**State of Colorado, Department of Natural Resources under Contract ENC#C154213 and National Science Foundation under Grant ATM-9420045**

# IMPACT OF SOIL MOISTURE INITIALIZATION ON A SIMULATED FLASH FLOOD

by Christopher Travis Ashby



William R. Cotton, P.I.

Colorado State University

# DEPARTMENT OF ATMOSPHERIC SCIENCE

PAPER NO. 702

# IMPACT OF SOIL MOISTURE INITIALIZATION ON A SIMULATED FLASH FLOOD

by

**Christopher Travis Ashby**

Department of Atmospheric Science

Colorado State University

Fort Collins, CO 80523

Research Supported by

**State of Colorado, Department of Natural Resources**

under Contract ENC#C154213.

**National Science Foundation**

under Grant ATM-9420045

Spring 2001

**ABSTRACT**

IMPACT OF SOIL MOISTURE INITIALIZATION ON A SIMULATED FLASH FLOOD

On the evening of 28 July 1997, an extreme rainfall event in Fort Collins, Colorado produced severe local flooding. Over 25 cm (10 in) of this fell over southwest Fort Collins during the 5.5 hour period beginning at 1730 MDT July 28 and ending at 2300 MDT. The Regional Atmospheric Modeling System (RAMS) Ver. 3b is used to simulate this event. The focus of this research is to better understand the simulated mechanisms for extreme precipitation generation given differing initial conditions. The simulations utilize four telescopically nested grids allowing for resolution of synoptic-, meso-, and convective scale motions in the respective domains. The initial atmospheric fields were supplied from the Rapid Update Cycle (RUC) operational forecast model analysis, sounding data and surface observations corresponding to 12Z 28 July 1997. Two simulations were performed, differing only in the method of soil moisture initialization. Simulation A was initialized with the soil moisture fields taken from the operational 40-km ETA forecast model analysis, while Simulation B was initialized using the Antecedent Precipitation Index (API) method of soil moisture estimation.

The synoptic scale forecasts show that Simulations A and B differ considerably in the boundary layer thermodynamic and wind predictions due to an overestimated evaporation fraction in regions of high soil moisture content in Simulation A. The primary difference in synoptic scale evolution between Sim. A and B is the intensity of the topographic circulation that results from a higher simulated low-level temperature in Sim. B. An accompanying increase and eastward shift in vertical mass transport relative to the Continental Divide, as well as increased Grid-2 precipitation volume are produced in Sim. B.

Precipitation evolution is similar between simulations prior to 1800Z followed by considerable differentiation in convective evolution after 1800Z. By 0500Z, 29 July, Simulation A produces a Grid-4 maximum accumulation of 26 cm (10.2 in.) 23-km to the southeast of Fort Collins. Simulation B generates two, Grid-4, maxima of 11 cm (4.33 in.) approximately120-km to the southeast of Fort Collins and accumulations of 8-9 cm approximately 30-km to the south and southeast of Fort Collins. Additionally, Simulation B produces a larger area of accumulated precipitation greater than 1-cm. The differences in accumulated precipitation occur despite comparable precipitation rates (~10-19 cm/hr) between simulations. Storm motion is identified as the primary contributing factor to the differences in accumulated precipitation. The time sequence of cell initiation locations in Simulation B is partially determined by the movement of the eastern edge of the storm-induced cold-pools. The theoretically predicted steady-state propagation speed for the cold-pool front is higher by a factor of 2.4 in Simulation B than in Simulation A during the quasi-stationary phase of the flood producing storm in Simulation A. This increase is due to the thermodynamic differences in the cold-pool environment rather than the cold-pools proper. During the quasi-stationary phase in Simulation A, the predicted steady-state cold-pool propagation speed is within 0.8 m/s of the upstream, lowest 200-m average wind-speed. These results suggest that the low-level thermodynamic forecast differences, which are controlled by the soil moisture initialization, are physically related to the accumulated precipitation differences through the cold-pool influence on storm propagation.

Christopher Travis Ashby
Department of Atmospheric Science
Colorado State University
Fort Collins, Colorado 80523
Spring 2001

## ACKNOWLEDGMENTS

I am grateful to many individuals who have contributed to my education over the past twenty-odd years. My sincere appreciation is extended to my advisor, Dr. William R. Cotton for granting me the opportunity to conduct this research and for his guidance, advice and patience throughout. In addition, my committee members, Dr. Thomas McKee and Dr. Jorge Ramirez, are recognized for their time dedicated and useful comments and discussions while reviewing this thesis. Much of the data used in the observational overview section of this thesis were generously provided by research associates and colleagues including Nolan Doesken, Jason Knievel, Ray McAnelly, Walt Petersen, Greg Thompson, and John Weaver. Drs. Robert Walko, Louis Grasso and all of the Cotton research group graduate students and research associates have been invaluable during this research, in terms of model assistance and scientific discussion — their contributions have been greatly appreciated. I am also indebted to the computer support staff within the Cotton research group for maintaining the functionality and utility of computer resources used in this research. I would like to record my gratitude to Brenda Thompson for her administrative assistance, and for providing constant reminders and words of encouragement to a very forgetful student. This research was supported by the State of Colorado, Department of Natural Resources, under Contract ENC#C154213, and the National Science Foundation, under Grant ATM-9420045.

One guiding principle of science was instilled in my mind by my guitar teacher Kelly Stuart to whom I am, to this day, extremely thankful: a problem understood is no longer a problem; an ignored or misunderstood problem will resurface when it is least welcome. Above all, I would like to thank my parents, Wayne and Cindy Ashby, for their love and dedication. The contributions made by these two great people cannot be so easily quantified or categorized and any attempt to do so here, would only trivialize their monumental importance to me. Finally, I would like to thank God, for giving me the mind and desire to pursue science.

# Table of Contents

# 1

# Introduction

Between the years of 1968 and 1997, an average of 140 deaths occurred annually due to floods and flash floods. Compared to lightning deaths (~76/yr), tornado deaths (~65/yr) and hurricane deaths (~24/yr), flooding and flash flooding are the most deadly of weather phenomena in the United States. (Woods, 1999)

Clearly, from both a scientific and humanitarian perspective, obtaining the ability to predict and warn the public of imminent flood disasters is a goal whose benefits would be extraordinary. However, floods and especially flash floods are still relatively unpredictable despite advances in forecasting techniques, observational methods and numerical weather prediction. One contributing factor to this problem is the relative rarity of the events that are truly catastrophic. For example, in Colorado, 180 deaths occurred due to floods/flash-floods between 1960 and 1997. However, 139 of these deaths occurred in a single night on July 31, 1976 in the Big Thompson flood. South Dakota records 249 deaths between 1960 and 1997 — 237 of which occurred, again, in just one night during the Rapid City flood of 1972 (Woods, 1999). The difference between floods which claim many lives and produce massive property damage versus those that produce no fatalities and little property loss is often determined by non-meteorological factors such as local drainage patterns and population density with respect to the drainage patterns (i.e. hydrological and social factors). However, even if one reduces the scope of the problem to that of the atmospheric component, that is, extreme precipitation, experience has shown that the predictability is still relatively low. This thesis only considers the atmospheric component of flooding and does not attempt to incorporate the science of hydrology or urban planning.

The purpose of this thesis is to determine the following:

1.) Given a realistic initial condition, supportive of extreme precipitation production, can a multi-scale numerical model produce a realistic extreme precipitation event?

2.) If the answer to Question (1) is affirmative, then to what extent does the location, timing, or even existence of the simulated extreme precipitation event depend on the specification of initial conditions?

3.) Given the sensitivity identified, do we currently have the required data and/or model accuracy to improve the location, timing, intensity and duration of precipitation in numerical forecasts for this type of event?

In brief, the initial condition chosen for this work is the 1200Z, 28 July 1997 analysis, which corresponds to the morning prior to the 1997 Fort Collins flash flood. The model used is RAMS version 3b (Pielke et. al., 1992). This event was chosen due to the higher quality atmospheric analyses available for initializing the simulations and the observational post-analyses which had been conducted independently of this thesis by other researchers (Doesken and McKee, 1998; Petersen et. al., 1999). Secondly, this event corresponds closely to the meteorological conditions surrounding the Big Thompson and Rapid City floods, which allows for a greater amount of background knowledge to be used in interpreting the results of the simulations (Maddox et. al., 1977; Maddox et. al., 1978).

The sensitivity investigated in this simulation is that of soil moisture initialization. Again, the hydrological aspects of antecedent soil moisture interacting with surface precipitation are not investigated, as the model used does not simulate the dynamics or evolution of surface runoff. Rather, the dynamics and thermodynamics of soil moisture interactions with the overlying atmosphere and the differences in the preconditioning of the storm environment are investigated. The choice of soil moisture as the varying parameter is motivated by numerous numerical studies in which variations in initial soil moisture significantly altered the simulated evolution of the convective environment (c.f. Chang and Wetzel, 1991; Bosilovich and Sun, 1999; Gallus and Segal, 2000; Beranardet et. al., 2000). Such a sensitivity, if found in the context of simulating extreme precipitation, may provide useful guidance for the use of a numerical atmospheric model in estimating extreme precipitation and/or Probable Maximum Precipitation (PMP) (Abbs and Ryan, 1997; National Research Council, 1994; Cotton et. al., 2000).

The remainder of this thesis contains a background chapter (Chapter 2) which presents prior relevant observational, numerical, and analytical research performed by persons other than the current author. Chapter 3 presents an observational overview of the Fort Collins flash flood and summarizes much of the work in Doesken and McKee (1998) and Petersen et. al. (1999). Chapter 4 describes the model configuration and description and an analysis of the two methods of soil moisture initialization used in this thesis. The synoptic-scale forecasts and differences among the simulations are discussed in Chapter 5 and the convective evolution along the Front Range is analyzed in Chapter 6. Finally, Chapter 7 contains a summary of conclusions drawn and suggestions for future research.

# 2

# Foundation

## 2.1 Flash Flood Meteorology

### 2.1.1 *Flash Flood Characteristics and Climatology*

Because of the potential property damage and threat to human life posed by flash flood events, efforts have been made to improve the ability of forecasters to provide advanced warning and more skillfully outline watch areas. Much of this effort has been directed toward better understanding the meteorological conditions that precondition the flash flood environment and recognizing typical synoptic and meso-$\alpha$ scale patterns that are conducive to flash flood producing storms.

Maddox et. al. (1979) examined 151 United States flash-flood events that occurred during the time period 1973-77. It was found that certain features were common to nearly all of these events. Firstly, nearly all events were produced by heavy rain that fell from *convective* storms. The ability of a convective updraft to rapidly process low-level, moisture-rich air, and produce precipitation-sized particles efficiently is essential. In addition, the convective nature of these events predisposes the warm season months to being the predominant period of occurrence of flash-flood events. In fact, it was found that 86% of U.S. flash flood events occurred during the warm season (April-September), and that 25% of these events occurred during July.

A second common feature was the relatively high value of the low-level dewpoint temperature in the affected areas, typically being in the 55°F to 75°F range. This is not surprising since low-level vapor mixing ratio and updraft velocity determine the rate at which an updraft supplies vapor to the storm system. In a similar climatology for Wyoming flash-floods, it was determined that high low-level moisture content, was instrumental in producing an unstable average sounding for flash-flood events (Rogash, 1988). Hence the effect of low-level moisture is multi-faceted, not only affecting the mixing ratio of updraft air, and hence the vapor supply for precipitation, but also contributing to the instability of the airmass on which the thunderstorm feeds. Additional effects, which may be quite significant, can manifest themselves by the lowering of the lifting condensation level (LCL) in high low-level vapor mixing ratio environments. These effects are discussed in more detail in following sections.

Thirdly, nearly all of the cases studied by Maddox et. al. (1979), exhibited high moisture content in a deep tropospheric layer, typically extending above 500 mb. One possible effect of high mid-level moisture content is the reduction in evaporation associated with entrainment. This not only decreases the ability of entrainment to dry the cloud mass but also reduces evaporational cooling and hence downdraft intensity within the convective column, which might otherwise interfere with or weaken the updraft of the storm or cause the storm to propagate away from the flood area. Finally, it was found that wind shear was typically weak to moderate throughout the cloud depth. A modeling study by Weisman and Klemp (1982) suggested that, for a given amount of buoyancy, low to moderate wind shear was conducive to secondary cell development and hence the formation and maintenance of a multi-cellular storm system. Secondary cell development along the rear flank of quasi-stationary, multi-cellular storms, can lead to extended periods of heavy precipitation over the same area, and hence represent one type of system capable of producing severe flash flooding. In addition Marwitz (1972) examined 14 high plains thunderstorms and found an inverse relationship between precipitation efficiency and vertical shear of the horizontal wind. In that study, it was believed that the effects of shear on both organization and detrainment contributed to the systematic variation in precipitation efficiency with shear.

While common features can be noted for almost the entire dataset examined by Maddox et. al, it was also found that the dataset could be divided, on the basis of synoptic and meso-$\alpha$ scale features, into distinct types of events. One of these categories was termed *Western events*. This particular category was not derived from meteorological considerations like the other three, but rather on geographical location, with events in this category lying primarily west of 104°W. The Big Thompson flash flood of 1976 and the Rapid City flood of 1972 were included in this category, as would be the Fort Collins Flash flood of 1997. This unrevealing choice of categorization stems from a number of problems. Firstly, flash floods that occur in the western United States typically occur over or near relatively complex terrain. The influence of terrain in initiating, maintaining and interacting with convective storms varies considerably with location and the situation. Secondly, the months with the highest frequency of flash-flood occurrence in the western U.S., are July and August, when much of the West is under the influence of the North American monsoon (Maddox et. al. 1979, Douglas et. al. 1993). During this time, surface patterns tend to be rather weak and upper level conditions benign, making it difficult to provide a simple, coherent classification of flash-flood events based on distinct meteorological conditions. Hence, the complex terrain and inconspicuous weather patterns of the western summer make classifying western events more difficult than for those in the eastern and central parts of the U.S., for which meteorological based classification schemes were given.

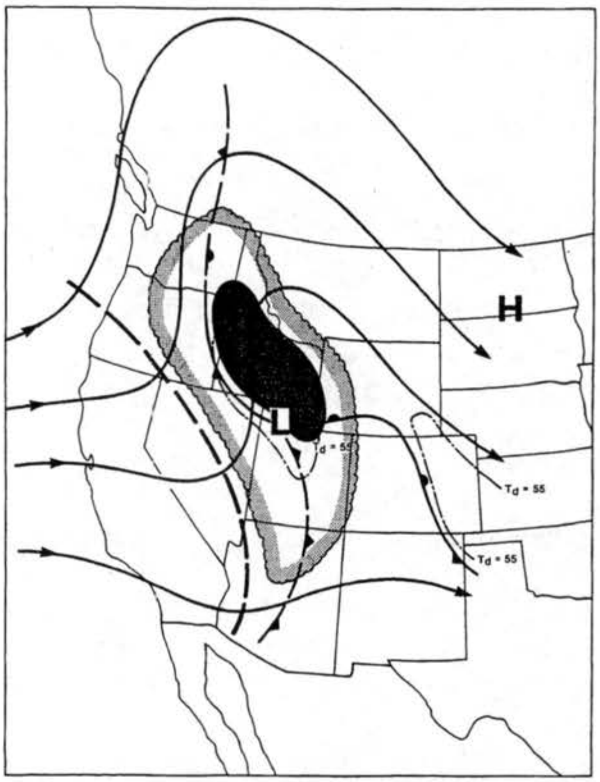


**Figure 2.1** Generalized 500 mb pattern for Type 1 western flash floods. 500 mb trough position depicted as heavy dashed line. Region at 500 mb with $T\text{-}T_d \leq 6°C$ is outlined. Time of analysis is just prior to onset of storm activity. Area of greatest flash flood potential is shaded. Taken from Maddox et. al. (1980).

A following study by Maddox et. al. (1980) was dedicated solely to the Western category of events, in recognition of the overly general treatment given to these events in the earlier work of 1979. In this later investigation, events were classified based on the 500 mb flow pattern. Using this methodology, Maddox outlined four primary 500 mb patterns associated with 61 documented flash flood events in the western United States. Of primary interest is the Type 1, 500 mb pattern seen in Figure 2.1, above. This pattern is characterized by a negatively tilted long-wave ridge overlying the flood prone area with an embedded short-wave trough ascending the western side of the ridge upstream of the threat region. The surface features in this figure are meant to be possible scenarios that may accompany the mid-level pattern and possibly help to focus convection. The short wave trough generally moves out of a stationary long wave trough to the west of the ridge or may rotate around a weak, stagnant, cut-off low located adjacent to the west coast.

Mean conditions at the flash-flood affected area, associated with the Type 1 pattern include an average surface temperature and dewpoint temperature of 78°F (26°C) and 55°F (13°C) respectively, and low dewpoint depressions from 700 to 300 mb (≤ 6°C). Wind speeds were generally less than 30 kt from the surface to 300 mb and winds were mainly southerly from 700-200 mb. Average precipitable water for these events was 0.94 in. (2.39 cm), 184% of the average monthly climatological value for the affected locations, and the average Lifted Index (LI) was -4. Hence, these events are characterized by abundant atmospheric moisture, especially in the low-levels, weak windspeed shear, and considerable instability, in addition to the general mid-level flow illustrated.

The Type 1 classification is especially relevant since the Fort Collins flood would, without question, fall under this category as an extreme example (see Section 3.2.1 for a thorough description of the FCL flood event). Additionally, the Rapid City and Big Thompson floods were Type 1 events. In fact, all of the western flash-floods documented in the Maddox et. al. (1980) paper that lie east of the Continental Divide and between 40°N and 44.5°N were Type 1 events (7 events total).

As illustrated in Figure 2.1 above, the primary threat area generally lies ahead of, or adjacent to, the approaching mid-level short-wave trough, as it approaches the ridge axis. The exact role, if any, of the embedded short-wave trough in these events has not been determined conclusively. Rogash (1988) noticed a similar short-wave feature at 300 mb in a study of the 22 July 1984 Wheatland, Wyoming flash-flood. Positive vorticity advection over the affected area at 300 mb was accompanied by near neutral vorticity advection at 500 mb. This placed the threat area in a dynamically favored region for positive, upper-level vertical motion via quasi-geostrophic differential vorticity advection, which in turn may have aided in destabilizing the upper troposphere. Additionally, Maddox et. al. (1977, Section 6) purport that the passage of the shortwave trough over the affected area is ultimately responsible for moving the storms away from the flood area. It should be emphasized however that this is an empirical conclusion, supported by the assumption that the shortwave has a significant impact on destabilizing the environment ahead of the shortwave. Hence, subtle synoptic and meso-$\alpha$ scale disturbances, in addition to topographic influences, may aid in the destabilization of the flash-flood environment.

One consequence of these studies is that they drew attention to the need for improved synoptic and meso-$\alpha$ scale analyses at local weather offices. Maddox et. al. (1980) demonstrated that National Weather Service (NWS) facsimile upper-air and surface charts were not sufficient for identifying many of the features found in their flash-flood climatology studies (e.g. embedded short-wave disturbances). However, even an analysis that reveals possibly pertinent meteorological features at the meso-$\alpha$ scale, still outlines a large threat area. In some cases, the threat area revealed by these analyses may be the same size as, or larger than, that of a forecast office watch area. Nonetheless, these results do highlight the relevant atmospheric conditions that warrant heightened awareness and caution within the flash flood warning program.

### 2.1.2 *Observational Case Studies*

Flash flood cases are notoriously difficult to observe due to their short duration, and localized nature. Due to the lack of predictability in time and space, special, planned observational efforts are nearly impossible. Advances in radar and satellite technology have added to the ability to analyze these events post facto, but the task of answering the specific question of why and how, is still largely conjectural. Two cases, not including the Fort Collins flash flood of 1997, have been given a considerable amount of attention observationally. These are the Big Thompson flood of July 1976 and the Rapid City flood of June 1972. Like the Fort Collins flood, these were Type I events that occurred in close proximity to a significant orographic barrier. Therefore, familiarity with the evolution of these events provides a background with relevance to the Fort Collins flood by analogue. Observations of the Fort Collins flood of 1997 is discussed in detail in Chapter 3.

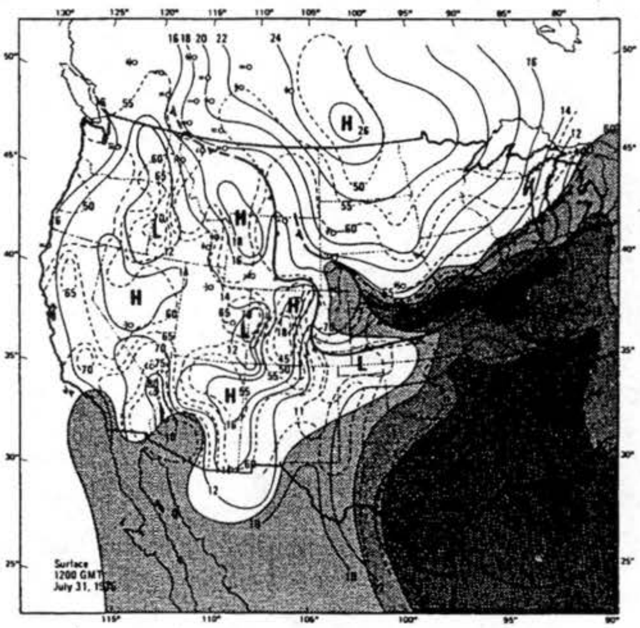


**Figure 2.2** Surface analysis for 1200Z 31 July 1976. Isobars are solid lines, contour interval 2 mb. Temperature are dashed lines at 5°F intervals, with high dewpoint (≥60°F shaded). Taken from Maddox et. al. (1978).

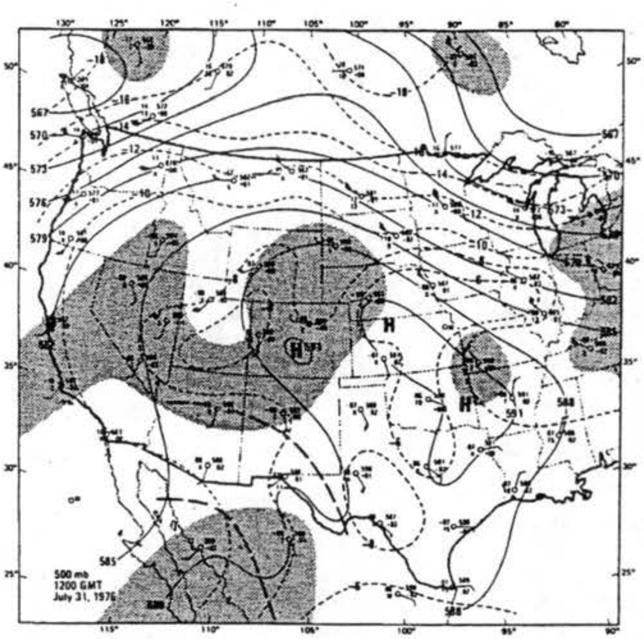


**Figure 2.3** 500 mb analysis for 1200Z 31 July 1976. Height contours (contour every 30m) are solid, short-wave troughs and isotherms at 2°C intervals are dashed. Regions where $T-T_d \leq 6$°C are shaded. Taken from Maddox et. al. (1978).

Caracena et. al. (1979) performed a detailed mesoscale analysis of the conditions prior to, during, and following the Big Thompson flood that occurred on 31 July 1976.

The maximum precipitation in the Big Thompson area exceeded 12", most of which fell between 0030Z and 0430Z (1830 and 2230 local time, respectively) (Maddox et al., 1978). This event occurred in association with a relatively strong surface high pressure system over the central plains that produced low-level easterly flow directed into the Front Range of the Rocky Mountains (Figure 2.2). The surface front on the southern and eastern peripheries of the high-pressure system laid in an east-west direction from Missouri through Kansas and into Colorado. Along the Front Range, the front acquired a north-south orientation and extended northward into Wyoming, roughly following the foothills of the Rocky Mountains. At 1800Z, or 6 hours prior to the onset of the flooding rain, the Loveland/Fort Collins temperature and dewpoint temperature were 75°F and 61°F respectively with mild southeasterly winds of 5-10 kt. The 1200Z 500 mb pattern is shown in Figure 2.3 above. Comparison with Figure 2.1 above, shows that the Big Thompson event was a prototypical example of the Type 1 event. The 500 mb wind above Denver was light westerly at 10 kt with a 2°C dewpoint depression. A shortwave trough at 500 mb over Arizona and New Mexico was moving slowly northward along the western side of the ridge.

One of the more important surface features was a secondary front, analyzed behind, or to the north, of the primary front. The latter had already passed through the Denver area twelve hours before the flooding rains began in the Big Thompson area. Behind the secondary front, partially located in southwest Nebraska, was an east-west oriented air mass, which exhibited a marked increase in both dewpoint temperature and easterly component of the wind. Dewpoint temperatures immediately behind this boundary were in the mid- to upper sixties (°F) and winds were easterly at 10-20 kt. The passage of this secondary front at Sterling, Colorado around 1900Z was adequately demonstrated in comparison of the 1340Z and 1935Z Sterling soundings. A lowering of the level of free convection (LFC) by 160 mb and an increase in precipitable water from 2.64 cm to 3.34 cm, from the 1340Z to the 1930Z Sterling, Colorado sounding, occurred after the passage of the front. An interpolated or estimated 0000Z sounding was constructed for Loveland, Colorado, which is approximately 20 km to the east of the Big Thompson drainage basin. This sounding had a Lifted Index of -6, but also exhibited a significant inversion at 730 mb. A surface parcel required 80 mb to reach the LFC. Greater instability and an increase in low-level moisture differentiated the post-secondary frontal airmass, which eventually fed the convective cells of the Big Thompson storm.

The passage of the secondary front at Table Mountain, in the Front Range foothills, was evidenced by wind profiler data taken from that location. These data exhibited a 15 m/s increase in the 300 m AGL, upslope flow, starting around 2330Z. Within 30 minutes of the trailing frontal passage at this location, a north-south line of thunderstorms developed along the Front Range foothills. This storm system became quasi-stationary over the Big Thompson drainage area between 0000Z and 0400Z resulting in severe flash flooding. Given that the post-frontal airmass exhibited a 730 mb inversion, it is likely that the orography, which the post-frontal surge ascended, was the primary, initial lifting mechanism for the Big Thompson storm complex.

Individual cell motion within the Big Thompson system was generally from southeast to northwest at approximately 8-12 m/s. Hence, the system was characterized by discrete propagation with new cells forming on the east and southeastern side of the multi-cellular system. The approximate rainout rate for the storm system, derived from a rain gauge calibrated Z-R relationship, was $9 \cdot 10^6$ kg/s, during it's three hour long, intense phase. A precipitation efficiency of 85% was calculated using approximate values of inflow mixing ratio, depth, and windspeed. (Caracena et al., 1979)

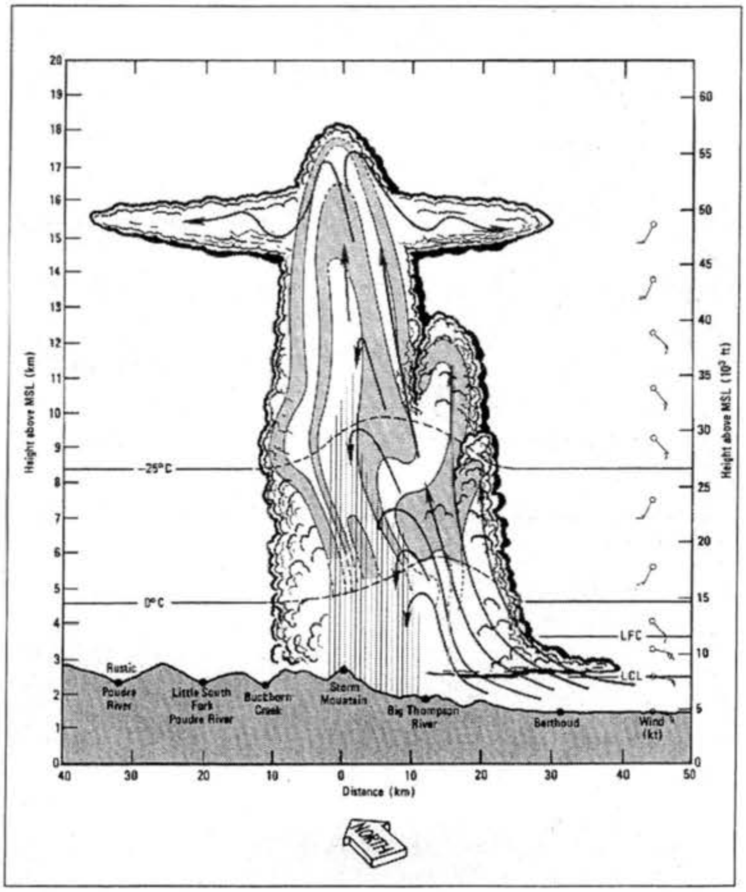


**Figure 2.4** Graphical depiction of physical model of Big Thompson storm. Taken from Maddox et. al. (1977).

A physical model for the storm was proposed, based on evidence supplied by radar reflectivity data, and the thermodynamic parameters of the inflow and environmental air (Figure 2.4 above). This model included the following characteristics. The combination of nearly ground altitude cloud-bases, and a 5.8 km MSL in-cloud freezing level, allowed for warm-rain processes to act in a relatively deep layer. Weak wind shear and moist mid- and upper-level air suppressed entrainment-induced evaporative losses. Low-cloud bases also minimized sub-cloud evaporation of falling precipitation. Each of these physical characteristics are proposed by the authors as factors which may have led to a high precipitation efficiency for the Big Thompson storm system.

Additionally, the authors argue that the moderate to strong easterly momentum of the low-level inflow air, and light winds aloft, a condition referred to as *reverse shear,* combined with the orographic anchoring of the average updraft position, resulting in a westward tilt of the storm updraft. Hence, rainwater could be efficiently unloaded from the updraft on the western side of the storm, opposite the inflow current, reducing the otherwise destructive effects, of water loading on the storm updraft. Additionally, radar reflectivity, did indicate a low echo centroid (LEC), with the highest reflectivity resting below 7 km MSL. This implies that much of the precipitation production and release from the convective plume was occurring in the lower levels of the cloud, reducing the effects of water loading in the upper portion. With reduced water loading in the upper portion of the cloud, it was suggested that greater updraft velocities could be achieved, possibly accounting for the high cloud tops (18 km MSL) observed. It was also proposed that efficient removal of liquid water at a lower altitude within the cloud would reduce the amount of supercooled water in the upper portions, thereby suppressing hail growth. The absence or reduction of hail in the Big Thompson storm would also minimize downdrafts created by melting of hail and graupel below the freezing level, resulting in little or no impetus for outflow-induced propagation away from the Big Thompson drainage. However, without more detailed, quantitative information for the Big

Thompson storm, or storms that develop under similar circumstances, the hypotheses formulated by these authors, remain largely untested. (Maddox et. al, 1977)

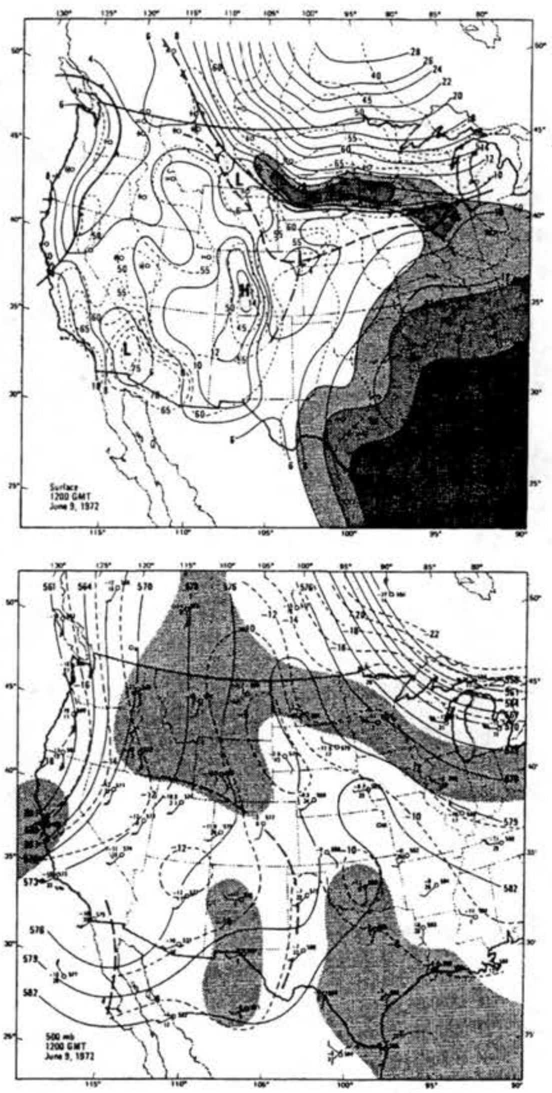

**Figure 2.5** Surface (top) and 500 mb (bottom) analyses for 1200Z 9 June 1972. Refer to caption of Figs. 2.2 and 2.3 for details.

A similar evolution occurred in the Rapid City flash flood of 9-10 June 1972. During the afternoon of June 9 and evening of June 10, as much as 15 inches of rain fell over the Black Hills of South Dakota, much of which fell over the Rapid Creek drainage.

At least 236 people were killed and damage totaled more than $100 million. (Maddox et. al., 1978)

Surface meteorological conditions at 1200Z were similar to those of the Big Thompson event. A strong polar high pressure system was moving southward through south-central Canada with a weak cold front lining the southern boundary of the system just to the south of Rapid City (Figure 2.5). Surface dewpoint temperatures behind the front were in the 60-65 °F range while those to the south of the front were still fairly moist in the range of 50-55 °F. At 500 mb, a large-amplitude, negatively tilted ridge was situated with the ridge axis located 200-300 km east of the Rapid City area (Figure 2.5). In addition, a weak short wave trough was embedded in the southerly flow along the western side of the ridge, with the trough axis extending from northern Colorado to the Texas panhandle.

The 1200Z Rapid City sounding showed a nearly saturated moist layer near the surface with a strong temperature inversion at 860 mb. Much drier air existed above the inversion, where the dewpoint depression was ~20°C. However, at Huron, South Dakota, 390 km to the east-northeast of Rapid City, dewpoint depressions of less than 3°C existed up to 750 mb. Easterly winds at the surface were approximately 25 kt at Huron with westerly winds of less than 10 kt above 750 mb. The atmosphere was considerably more unstable at Huron, with a lifted index of -7, compared to +6 at Rapid City. Precipitable water in the Huron sounding was quite high at 1.32 inches in the surface-500mb layer, which was nearly twice the Rapid City June means of 0.71 inches. Like the Big

Thompson event, the eventual flood area laid downstream of much more unstable and moist conditions. (Maddox et. al., 1978)

At 0000Z the surface winds across most of South Dakota were easterly and had increased to 20-30 kt, increasing the low-level moisture flux into the Black Hills area. At 500 mb the short-wave trough had progressed northward with the axis located at the intersection of the Wyoming, Nebraska, and South Dakota borders, just to the southwest of the Black Hills. This placed the Black Hills in an area of weak 500 mb vorticity advection. Southeasterly winds at 20 kt were present over Rapid City at 500 mb. The 10 June 0000Z Rapid City sounding exhibited considerable differences from the 9 June 1200Z sounding. Precipitable water in the surface-500mb layer had increased from 0.42 to 1.32 inches with a near tripling in the lowest 150 mb from 0.28 to 0.76 inches. Hence, rapid changes had occurred in the flood area during the previous 12 hours, priming the atmosphere for potentially catastrophic rainfall amounts from slow moving convective storms, which were realized between 2300Z June 9 and 0500Z June 10. (Maddox et. al., 1978)

Dennis et. al. (1973) estimated the total amount of water vapor supplied to the Black Hills storms using the maximum 15 g/kg vapor mixing ratio of the approximately 1 km deep layer of low-level air impinging on the Black Hills for the six hour duration of the event. This yielded roughly 500,000 acre-feet ($6.2 \cdot 10^{11}$ kg) of water vapor compared to 400,000 to 500,000 acre-feet ($5.0 \cdot 10^{11}$-$6.2 \cdot 10^{11}$ kg) of precipitation estimated from planimetered precipitation observations. Thus, the authors estimated the precipitation efficiency of the Black Hills storm system to be between 75% and 100%, which is comparable to the value of 85% estimated for the Big Thompson storm. Like the Big Thompson storm, not only were the convective cells supplied with moisture-rich inflow air, they were also remarkably efficient at converting the vapor supply to realized precipitation.

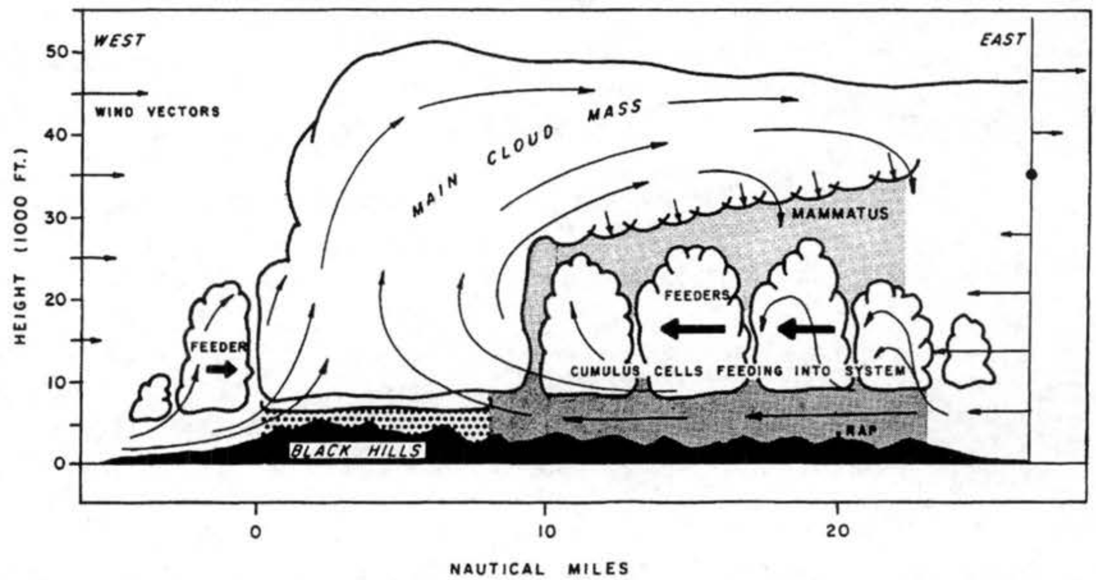


**Figure 2.6** Cloud morphology as inferred from radar and eyewitness observations. Lines with arrows represent main flow of air through the cloud system. Short double arrows represent the individual cell motion. Rapid City is denoted by "RAP". Taken from St. Amand et. al. (1972).

St. Amand et. al. (1972) proposed a physical model for the storm based on radar and eyewitness observations. This model included the recycling of upper level moisture by frozen and liquid precipitation falling from the anvil of active cells, into "feeder" cells that had initiated upstream in the low-level easterly flow (Figure 2.6 above). Therefore, the high precipitation efficiency was believed to be in part due to the reverse shear situation where upper level winds advected the upper level outflow over developing cells moving westward. This is in contrast to the Big Thompson storm model in which the storm titled downstream of the low-level flow and the lack of precipitation upstream of the main updraft was key to the maintenance of the system.

As in the Big Thompson case, downdrafts were nearly absent from the Rapid City storm complex. Dennis et. al. cite this as a probable mechanism for the stationary character of the system. They reasoned that the lack of downdrafts from the system allowed the easterly stream of moisture rich air to continually feed the convective cells. Had downdrafts developed to any significant extent, the associated surface outflow would have propagated eastward, down the slope of the Black Hills, forcing inflow air to rise farther to the east and causing the system to propagate away from the hills. These authors explained that the Black Hills actually experienced upslope fog during the afternoon, prior to and during the event, and hence cloud bases would have literally been on the ground. Therefore, sub-cloud evaporative cooling would have been nearly absent, reducing the impetus for downdraft formation.

### 2.1.3 *Numerical Simulations of Flash Floods*

From the observational studies presented thus far, it should be clear that mesoscale and synoptic scale dynamics play an important, even if not completely understood role in establishing the convective environment. However, materialization of flash flood producing rainfall relies on convective scale microphysical and dynamical processes for rapid precipitation formation and quasi-stationary movement. While observational studies have done quite well in providing an objective description of the synoptic and meso-scale processes which accompany particular flash flood events, detailed observations of convective scale processes are scarce and often must be inferred from indirect evidence using questionable assumptions and qualitative eyewitness descriptions. Within this void of uncertainty, numerical modeling of cloud systems has great potential to provide insight and direction toward understanding and quantifying those processes at and relevant to the convective scale and which ultimately lead to the phenomenon of flash flooding.

The past thirty years has seen significant advances in atmospheric model dynamics, microphysics, and land-surface process formulations, as well as a near exponential increase in computer speed and storage capacity. This has allowed for increasingly complex and, presumably more accurate, numerical representations of cloud systems and the accompanying dynamics. However, while convective- and mesoscale phenomena such as squall-line and supercell thunderstorms are well represented in the literature, relatively few simulations have addressed cumulonimbus systems that produce locally extreme precipitation amounts. The combination of sparse numerical treatment and rapid advances in model technology has resulted in a population of experiments with a widely varied set of implied assumptions and simplifications such as two-dimensionality of fluid motions, highly simplified ice- and liquid-phase microphysics, idealized terrain shapes, and initially homogenous distribution of land-surface characteristics. What follows is a brief examination of some of the more important results obtained in these investigations.

One approach to dealing with the constraints of memory and limits on computational speed is to not simulate the convective scale explicitly. The assumption in this approach is that the synoptic- and meso-scale forcing mechanisms (low-level convergence, orographic lifting, etc.) are sufficiently resolved in a relatively coarse mesh simulation (~40-120 km) so that the simulation will still produce an area of maximum precipitation in the realized flood area. This was the approach taken by Chang and Perkey (1995), in their study of the Big Thompson and Rapid City storms. Two sets of simulations were performed at 140 km and 35 km grid spacing for 24 and 12 hours respectively, bracketing the time of the actual flood events. At both resolutions, the model successfully produced a precipitation maximum within one grid point of the Big Thompson area. While the predicted precipitation amount was less than 20% of the observed maximum, the clear depiction of a local maximum over the Big Thompson drainage suggested that this approach was capable of reproducing the most important meso- and synoptic scale forcing mechanisms for the storm system. In contrast, the Rapid City simulations failed to produce a precipitation maximum near Rapid City. The authors attributed this to the inability of the model to properly simulate the propagation of the shortwave trough that was moving northward along the backside of the longwave ridge. This trough was believed to have aided in the development and maintenance of the storm system. Interestingly, this problem was traced back to a model temperature error of ~-2.5°C in the planetary boundary layer (PBL), in both simulations, over the arid highlands of the western U.S., where the PBL may often extend into the lower mid-troposphere. This resulted in an increased mid-level cyclonic circulation in the shortwave trough environment that hastened its progress over the southern Plains and retarded the movement of the trough over northern Colorado. The implication in this study was that, at least in the model solution, the short wave trough was a crucial forcing mechanism for the heavy precipitation at Rapid City while the surface frontal surge was sufficient for the Big Thompson case. However, without a successful simulation of the short-wave propagation, and an accompanying precipitation maximum near Rapid City, the role of the shortwave was not firmly established in this study. Inadequate representation of the Black Hills (~100 km square) by the 35 km grid is a possibility as well. In addition, no modeling study to date has demonstrated, unequivocally, the importance of the short-wave trough in the evolution of Type 1 events. This idea has limited support from the quasi-geostrophic theory of atmospheric motions as noted previously, but without detailed quantitative analysis, the evidence remains circumstantial yet relevant. Nonetheless, the proposed effect of PBL temperature on the shortwave propagation highlights a subtle, but potentially critical mode of surface influence on relevant synoptic scale features.

Kopp and Orville (1973) (KO) utilized a two-dimensional, time-dependent mountain cumulus model with 200 meter grid spacing to simulate the Rapid City storm. Using idealized terrain KO succeeded in producing a storm with updrafts in excess of 30 m/s and a maximum of 2.7 cm of precipitation during 33 minutes of simulation. This rainfall agrees reasonably well with the observed average rain rate of 5.1-7.5 cm/hr. Graupel and hail, a single hydrometeor category in their model, was found to reach a maximum in-cloud concentration of 8 g/kg, comparable to the maximum rain water concentration in the same simulation of 9 g/kg. Given that only 0.018 cm of hail/graupel fell to the ground in this simulation, melting of graupel and hail must have contributed substantial amounts of liquid water to the precipitation total. In addition, this simulation produced ~5 m/s downdrafts within the hail/graupel shafts but the role of these downdrafts in the simulated storm motion was not investigated.

A particularly disturbing problem in the KO simulations was the storm location to the west of the idealized terrain. The actual Rapid City storm concentrated the flood producing precipitation on the eastern slopes of the Black Hills. This model error could be a result of the fact that the terrain used in their simulations was completely unrealistic.

In particular, while the maximum terrain height in their simulations was nearly that of the Black Hills (5-6 kft MSL, 1.1 km AGL), the terrain rise occurred over a 600 m distance, producing a wildly exaggerated slope. Hence, their results have to be interpreted with extreme caution since the initial streamlines at the mountain were derived from potential flow around a cylinder with a radius equal to the height of the mountain.

Nair et al (1997) performed three-dimensional simulations of the Black Hills storm using the Regional Atmospheric Modeling System (RAMS) (Pielke et al, 1992). The simulations were initialized at 0000Z, around the time that the flooding rains began, and were integrated for six hours. The authors tested both homogenous initialization, in which the initial winds, pressure, temperature and humidity were derived solely from the 0000Z Rapid City sounding, and inhomogenous initialization, in which the initial fields were interpolated to the model grids from spatially varying gridded analyses. The homogenous simulation (HH1 in their paper) utilized a single grid with 1-km grid spacing covering most of the Black Hills region, while the inhomogenous simulation (IH1) utilized three, two-way interactive nested grids, the finest with 2-km grid spacing. The coarse grid covered most of South Dakota and parts of neighboring states, and hence was considerably more extensive than the single grid in the homogenous simulation. Topography was obtained from a 30" U.S. Navy terrain dataset. The maximum accumulated precipitation in IH1 was 220 mm, compared to the observed maximum of 380 mm, while HH1 produced 275 mm. However, the homogenous simulation concentrated the precipitation near the western grid boundary at the highest terrain, while the observed precipitation distribution was concentrated along the eastern slopes. IH1 reproduced the location of the maximum precipitation more realistically with four local maxima located along the eastern slopes of the Black Hills. Sensitivity simulations revealed that the erroneous precipitation distribution of the homogenous simulation was primarily due to the proximity of the outermost boundary, where radiative boundary conditions (Klemp and Wilhelmson, 1978) were imposed, to the Black Hills region. An additional homogenous simulation (HH3 in their paper) was performed which utilized the grid structure of IH1, to provide some measure of the importance of the horizontal variations in the initial conditions. This simulation produced a single maximum of 305 mm in contrast to the four local maxima produced in IH1. The maximum accumulated precipitation in the HH3 simulation was closer to the observed maximum, while the multiplicity of local maxima in the inhomogenous simulations was in better agreement, qualitatively, with the observed precipitation distribution. Because the inhomogenous simulation still produced flood-intensity storms, this simulation was considered more representative of the actual storm evolution. Storm structure also differed between HH1 and IH1. HH1 produced a storm with little vertical tilt, while the IH1 storm exhibited a pronounced westward tilt with height. Thus, the simulated storm structure in IH1 resembled the physical model proposed by Maddox et al for the Big Thompson storm but differed from the eastward tilted storm proposed by St. Amand et al for the Black Hills event. It should be emphasized, however, that the St. Amand storm model is based on radar and eyewitness observations, and therefore the simulated tilt of the Black Hills storm cannot be considered a refutation of this model unless the observations and/or their interpretation are flawed.

Miller (1978) conducted simulations of the 1975 Hampstead storm without an explicit ice-parameterization. The original simulations in that study grossly underestimated rainfall rates and the author in that study suspected the lack of ice-phase microphysics may not take into account the increased terminal velocity of hail. Hence, the terminal velocity of rainwater was doubled in an attempt to take into account the increased fall speed of hail. While this adjustment is difficult to justify rigorously, the result was a ten-fold increase in precipitation from the simulated storm. The direct implication is that higher terminal velocities lead to increased updraft vapor flux without a detrimental effect from water loading, or that higher terminal velocities allow for a greater precipitation efficiency through undetermined microphysical processes, or both. Miller notes that the increase in terminal velocity ultimately led to the production of a vigorous downdraft within the heavy rainfall area. Because of the veering wind profile, with height, the storms moved in a direction to the right of the low-level flow. This produced an asymmetric outflow region elongated perpendicular to the low-level inflow (Figure 2.7 below). This maximized the low-level convergence over a large area along the gust front that produced continual regeneration of cells at nearly the same location throughout the simulation. This result coupled with the Nair et. al. and KO results suggests, but is conclusive by no means, that the increased fall speeds of denser ice-particles that subsequently melt may be an important contributing mechanism to the rapid release of precipitation from a storm. However, as mentioned previously, the Maddox et. al. storm model for the Big Thompson event proposed that the absence of hail and graupel, and more specifically, the lack of melting of these species, contributed to the lack of downdrafts in the Big Thompson storm. Thus, while one model suggests, a nearly complete, or complete lack of downdrafts for quasi-stationary movement, the other relies heavily on individual cell movement and the existence of a prominent outflow for a quasi-stationary *system.*

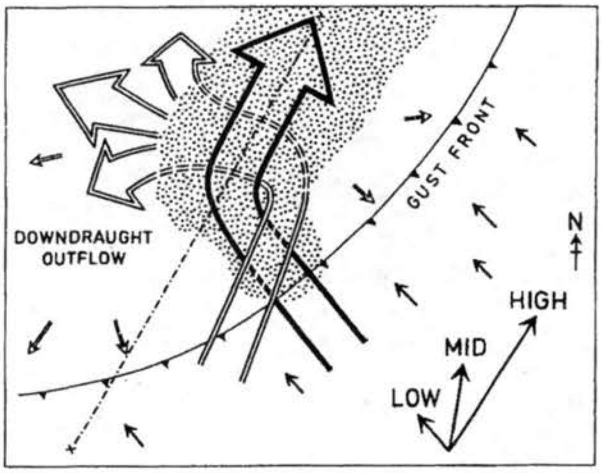


**Figure 2.7** Schematic of primary features of the storm model deduced from the simulation. Winds at various levels depicted in lower right corner. Taken from Miller (1978).

Yoshizaki and Ogura (1988) (YO), conducted two-dimensional simulations of the Big Thompson storm. These authors found that homogenous initialization of moisture below 3 km AGL resulted in convective initiation at the Continental Divide, the highest point of the idealized terrain. Maximum accumulated precipitation occurred 10 km to the west of the Continental Divide as cells matured downstream of the location of initiation. However when low-level moisture was initialized inhomogeneously, with enhanced vapor mixing ratio upstream of the elevated terrain, the initial convection formed 40 km east of the Continental Divide with maximum precipitation rates occuring 20-30 km to the east of the Continental Divide, in better agreement with observations. This suggests that the heterogeneous, post-frontal surge of enhanced moisture air described in Caracena et. al. (1979) may have been critical in locating the quasi-stationary storm system over the Big Thompson drainage basin. In that particular simulation, a multi-cellular storm was produced with new cells forming along the eastern, down-slope edge of the storm-produced cold-pool after the initial cell moved westward. This cold pool formed as rain fell through the cloud-free region to the west of the westward tilted updraft. One peculiar aspect of this simulation was the westward drift of the cells after initiation. The environmental winds present in the initial sounding had almost no east-west component between 3 and 7 km AGL. Analysis of the model produced winds showed an area of enhanced easterly wind at ~3km AGL to the east of the warm convective core, which advected the convective plume westward. This was attributed to a horizontal pressure gradient force directed toward the west on the upstream side of the convective plume at ~3 km AGL. This pressure gradient force was the result of a buoyancy gradient produced by the thermal contrast between the underlying cold pool and convective heating within the core of the updraft. The westward advection of the convective plume, away from the eastern leading edge of the cold-pool allowed for new cells to initiate in this location, leading to the simulated multi-cellular character of the storm. Therefore, in contrast to the Maddox et. al. conceptual model of the Big Thompson storm, the formation of a cold pool through evaporative processes was important in establishing the gross characteristics of the simulated storm. The results of several simulations in the YO study indicated that the location of the initial cell formation was the primary factor controlling the general location of maximum precipitation rate. Only when the initial convective cell formed 20-40 km upstream of the Continental Divide, was the precipitation maximized over the intermediate (2-3 km MSL) elevation areas east of the Continental Divide. The model used in the YO study did not include a surface flux parameterization and therefore the effects of varying surface characteristics, other than topography, were not explored.

In summary, previous attempts at modeling flash flood cases have demonstrated that various assumptions about dimensionality of flow, boundary conditions, terrain shape, and horizontal homogeneity on convective initiation and evolution can strongly influence the character of the solution. In the next section, we will examine the assumption of homogenous land characteristics such as vegetative type and coverage, soil moisture content and soil type. The reader should note that model formulations that do not include vegetation and soil parameterizations implicitly assume homogeneity in these parameters unless action is taken to artificially alter surface fluxes of moisture and energy.

## 2.2 Effects of Surface Characteristics on Mesoscale and Convective Circulations

Horizontal variations in sensible and latent heat fluxes at the earth's surface can result in significant horizontal variability in boundary layer thermodynamic structure and characteristics. These variations in boundary layer characteristics can induce thermally driven meso-scale and micro-scale circulations. Once established, these circulations may contribute, through advective processes, to the spatial variability of boundary layer properties and may have a measurable impact on vertically integrated convective parameters such as convective available potential energy (CAPE) and convective inhibition (CIN). Both observational and numerical studies have been conducted to better quantify these variations and their effects on mesoscale flows and convective motions. A subset of this work is presented here.

### 2.2.1 *Mechanisms for soil moisture influence*

In many numerical models the flux of sensible and latent heat, or water vapor, from the soil surface is determined by atmospheric surface layer fluxes of these quantities, which, in turn, require knowledge of the soil surface specific humidity and temperature. Soil-surface specific humidity is generally treated as a function of surface soil moisture and soil surface temperature. Hence the continuity of vapor and thermal energy exchange across the air-soil interface provides a constraint that tightly controls the soil temperature as well as the magnitude and partitioning of sensible and latent heat flux. (McCumber and Pielke 1981, Tremback and Kessler 1985, Mahrer and Pielke 1977)

Within the soil medium, transport of water substance is approximated by the Darcy-Buckingham equation: $q = -K\frac{\partial H}{\partial z}$, where K is the unsaturated hydraulic conductivity (or saturated hydraulic conductivity if the soil is saturated), H is the hydraulic head, a measure of the gravitational and soil water pressure head, or soil moisture potential, and z is the height above an arbitrary reference level. Thermal energy flux can be approximated by Fourier heat conduction with a known expression for the thermal diffusivity. Thermal diffusivity, soil moisture potential, and hydraulic conductivity are functions of volumetric soil moisture content, and soil type, as is the soil albedo. Hence the soil moisture content influences nearly all physical processes involving energy and mass transfer within the soil, in addition to that with the overlying atmosphere. (Maidment, 1993; Stull, 1988)

McCumber and Pielke (1981) conducted a series of one-dimensional numerical sensitivity tests to assess the relative contributions from variations in selected moisture dependent processes on energy flux magnitude and partitioning at the soil surface. The simulated soil depth was 1 meter with 14 soil levels, and did not contain a vegetation parameterization. These simulations indicated that the effect of albedo variation had relatively minor effects on maximum latent and sensible heat flux compared to the total change in sensible and latent heat flux due to soil moisture changes. For example, in comparing two simulations with sandy soil, initialized with identical soil moisture content, one with constant albedo and the other with moisture dependent albedo, the change in maximum fluxes of sensible and latent heat were < 50 $W/m^2$. However, they also compare two simulations for sandy soil with albedo held constant at 0.2, but initialized with 17% and 30% moisture saturation. A difference of 550 $W/m^2$ and -300 W/m^2 was produced between in the maximum latent and sensible heat fluxes, respectively, between the moist and dry initializations. While the effect of soil moisture on albedo is not negligible, the albedo effect alone on energy flux does not account for the large differences in energy flux seen in the second set of simulations (since albedo was held constant).

These simulations indicate that increased moisture content allows for a greater portion of the incoming solar radiation to be used for evaporation rather than for increasing the temperature of the soil. The larger soil moisture content increases the soil surface specific humidity, which in turn increases the calculated humidity gradient between the soil surface and the first atmospheric level. Hence, the surface flux of vapor increases, resulting in a negative impact on increases in soil thermal energy.

This same study also examined the influence of the vertical variation of initial temperature and moisture profiles for sandy soil. The variations introduced were designed to be representative of typical uncertainties in both temperature and moisture, typical for most model initializations. Peak variations in surface soil temperature, surface specific humidity and latent and sensible heat fluxes to the atmosphere were typically an order of magnitude larger for the soil moisture profile perturbations than for the temperature profile perturbations. The conclusion from this experiment was that, at least for daytime simulations, the surface soil temperature is strongly modified by solar forcing. Thus, the initial moisture profile is the more influential factor in determining the variations in sensible and latent heat flux to the atmosphere.

Finally, the authors examined the dependence of peak soil surface temperature and total moisture extraction on soil type and initial moisture content. The soil types used were peat, sandy, sandy-clay, sandy loam. With the exception of peat, it was shown that within the range of wilting point to 75% saturation, the initial soil moisture produced variations in soil temperature and energy fluxes that were again an order of magnitude greater than that due to soil type variation. These results indicate that the primary control on the evolution of latent and sensible heat flux from a bare soil boundary is the dependence of soil surface specific humidity and temperature on soil moisture. This implicates soil moisture as an extremely important variable for proper simulation of surface fluxes as well as for predicting boundary layer temperature and humidity. However, since this study was one-dimensional, horizontal variations in soil moisture could not be investigated. The one-dimensional approach did however provide a simple framework for understanding the basic sensitivities of the energy flux to soil moisture in an early soil-atmosphere model.

### 2.2.2 *Research on flux induced, mesoscale solenoidal circulations*

The term *non-classical mesoscale circulation* (NCMC) was coined by Segal and Arritt (1992) for thermally-driven circulations due to horizontal gradients in surface sensible heat flux, excepting the case of the land/sea breeze. The land/sea breeze and the NCMC form by the exact same mechanism, namely the creation of a pressure-density solenoid (PDS) by differential sensible heat flux between adjacent surfaces. Rigorously, a pressure density solenoid is a closed contour $C$ on which the integral $\oint_C \frac{dp}{\rho} \neq 0$, where p is the thermodynamic pressure and ρ is the mass density of the fluid. This is equivalent to the baroclinic source term $\frac{\nabla\rho \times \nabla p}{\rho^2}$ having a non-vanishing area integral on a surface bounded by the closed contour $C$. A PDS, by virtue of Kelvin's circulation theorem, will cause the circulation defined by $\oint_C \mathbf{U} \cdot \mathbf{dl}$ where **U** is the velocity vector, to increase in time when $C$ is a material contour. In short, a temperature gradient along a surface of constant pressure has the potential to initiate and maintain, against frictional vorticity losses, a circulation whose forcing is thermally direct. This situation is shown in Figure 2.8 below. This figure depicts a thermally-direct circulation shown along a closed contour, induced by a moist perturbation area (PA) with reduced sensible heat flux ($H_s$) surrounded by a drier surface with a larger sensible heat flux. The vertical solid lines are superimposed potential temperature plots, showing, qualitatively, the boundary layer thickness variation that results from the gradient in sensible heat flux and the resultant NCMC.

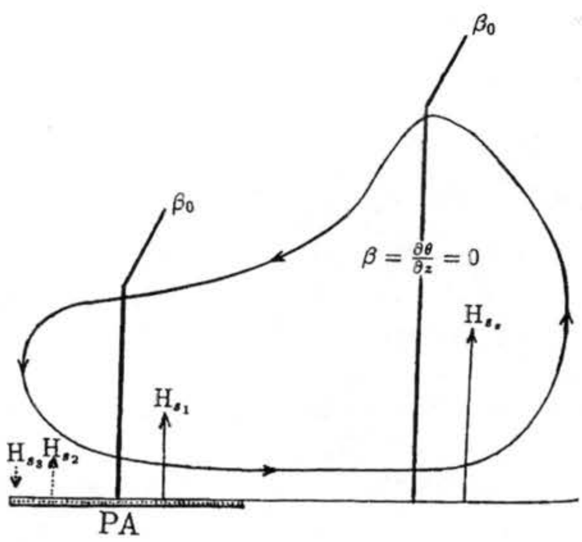


**Figure 2.8** Illustrative vertical cross section of NCMC. See text for details on notation. Taken from Segal and Arrit 1992.

The influence of soil moisture availability on NCMC formation and magnitude was studied numerically by Ookuchi et. al. (1984). This study showed that a meso-β scale (20-200 km) variations in soil moisture ranging from total saturation to zero moisture availability were capable of producing a thermally-direct circulation with a surface wind speed maximum of ~5 m/s and a temperature perturbation of approximately 18 K. As we shall see shortly, this type of circulation, under conditionally unstable conditions, can aid in triggering deep convection. However, these simulations had a weak background flow of 0.5 m/s perpendicular to the moisture gradient. Segal and Arritt (1992) provided a scaling argument indicating that increases in ambient wind speed required increases in the moisture perturbation length scale in order to counter the large scale flow. For background wind speeds greater than ~6 m/s, their scaling argument predicted that the NCMC formed would be too weak to counter the large scale flow. Therefore, the strength of the NCMC and associated temperature perturbation obtained in

Ookuchi et. al. (1984) would represent a largely undisturbed NCMC. With stronger background wind speeds, these intensities would be expected to decrease.

### 2.2.3 *Influence of surface energy flux on convective initiation and maintainance*

Yan and Anthes (1988) considered the effects of various soil moisture perturbation geometries on convective initiation and rainfall. They found that a configuration with a 144-km width of dry land, surrounded by uniformly moist land, generated the largest amount of rainfall in the geometries considered. This was attributed to a.) the increased convergence over dry land of two counter-propagating thermal fronts which move inward from the surrounding moist land and b.) the higher surface evaporation that occurs over the moist land than in the other geometries considered. Alternating bands of moist and dry land with length scales less than ~20 km produced NCMC's which were neither strong enough nor sufficiently deep to initiate convection. For these smaller wavelengths, vertical and horizontal advection, as well as horizontal mixing, hindered the development of the horizontal temperature gradient and the strength of the NCMC was not sufficient for the development of deep convection. While observational corroboration of these results is sparse, Brown and Arnold (1998) found that statistically significant spatial clustering of free convective cloud masses occurred over land-cover-type and soil-order boundaries in Illinois. In addition, they found that this effect was most pronounced on days with higher PBL dewpoint temperatures, and weak synoptic flow. This supports the argument that in the absence of significant synoptic forcing mechanisms, convective initiation in the unstable PBL may be strongly influenced by land surface heterogeneity.

Clark and Arritt (1995) used a one-dimensional atmospheric model with soil, vegetation and cumulus parameterization to examine the influence of soil moisture on convective rainfall. It should be noted that the one-dimensional formulation completely neglects the effects of horizontally varying soil moisture on PDS formation, which has already been shown to be important for convective initiation in the preceding experiments. The results of Clark and Arritt showed that fully vegetated and moist surfaces were most conducive to convective rainfall. As the work by McCumber and Pielke also suggested, the Clark and Arritt simulations demonstrated that albedo and thermal conductivity variations with soil moisture were far less important in influencing convective initiation than the effect of soil moisture on determining the partitioning between latent and sensible heat flux.

Chang and Wetzel (1991) used a mesoscale model with soil and vegetation evapotranspiration model to investigate the effects of vegetation and soil moisture variability on the evolution of the prestorm environment near Grand Island, Nebraska. In these simulations, soil moisture gradients were important for maintaining the thermal contrast across a stationary front over Grand Island. In addition, boundary layer height gradients produced horizontal gradients in frictional deceleration of the low-level flow that enhanced the horizontal convergence and vertical motion near the stationary front. The timing of the vertical motion production was linked to the collapse of the boundary layer over the vegetated, moist soil regions where the sensible heat flux reversed sign in the late afternoon. In addition, the authors noted that the ability of the vegetation to tap root-zone soil moisture was critical since soil surface evaporation alone was too weak to correctly predict the horizontal variability of the surface temperature. Therefore, the effects of soil moisture and vegetation can, in a numerical model, influence the timing and location of convective initiation.

Modification of boundary layer thermodynamic properties can become especially important when considering the problem of determining the location, relative to an orographic barrier, of quasi-steady state convection in an orographically lifted boundary layer flow. Grossman and Durran (1984) studied this problem observationally and analytically in the context of explaining the influence of the West Ghat Mountains in India on persistent offshore convection during the 1979 Summer Monsoon Experiment (SMONEX). The typical vertical wind profile for days with offshore convection exhibited low level, onshore westerlies at 10-14 m/s, and winds with an easterly component above 5 km. Analysis of observational data showed a 5-7 m/s deceleration of the boundary layer onshore flow over a 250 km path upstream of the coast. It was suggested that the West Ghats generate an upstream pressure gradient force that decelerates the boundary layer flow, forcing horizontal convergence and an accompanying vertical motion field. They concluded that the upstream blocking effect of the West Ghats might contribute significantly to boundary layer lifting and destabilization offshore. A solution that they derived from a non-linear, hydrostatic analytic model with vertically constant basic-state flow also bolstered their claim. Their solution indicated that increased vertical wind shear and upper-level subsidence would occur over the mountain range, suppressing the development of deep convection. However, Smith (1985) questioned their analysis claiming that convective latent heating, basic state wind shear and coriolis effects could not be neglected.

Ogura and Yoshizaki (1988) addressed these shortcomings using a two-dimensional cloud-resolving, moist, non-hydrostatic, compressible numerical model. Their simulations targeted the effects of ocean surface sensible and latent heat fluxes, cloud microphysical processes and vertical wind shear on the location of maximum precipitation relative to the topography. The authors found that inclusion of sensible and latent heat flux from the Arabian Sea, as well as a vertically sheared flow, was essential in locating the region of maximum precipitation well offshore in their simulations. Energy flux from the Arabian Sea decreased the amount of boundary layer lift required to initiate deep convection, allowing parcels to become positively buoyant further upstream of the mountain barrier. The presence of an opposing upper level flow, as opposed to vertically uniform flow, enhanced the low-level lifting upstream of the West Ghats. Additionally, the wind shear also influenced storm movement once the cells matured, causing them to reverse direction and slowly migrate westward with the upper level flow resulting in a precipitation maximum further offshore. As pointed out by these investigators, the location of maximum precipitation is likely to be dependent on other factors as well. Because their model did not incorporate ice processes, they could not examine the potential effects of ice processes in the westward sheared storm anvils on underlying precipitating cumuli. Nonetheless, the demonstrated sensitivity to surface latent and sensible heat flux greatly complicates the problem of deciphering the mechanisms for orographic influence on convective rainfall.

Tripoli and Cotton (1989) examined the influence of terrain induced PDS formation on the maintenance and initiation of a mesoscale convective system (MCS) which originated over South Park, Colorado. This study proposed a conceptual model for orogenic MCS formation in which the interaction between a meso-$\alpha$-scale thermally driven shallow slope flow and downward transport of westerly momentum produces an upbranch of enhanced vertical velocity where the simulated meso-$\beta$-scale convective system intensified explosively. Persistent convective heating within the MCS resulted in an effective deepening of the meso-$\alpha$-scale PDS to the tropopause, with an attendant growth of the meso-$\beta$-scale circulation into the meso-$\alpha$-scale. Additionally, their simulations showed that the meso-$\alpha$-scale slope flow acts to intensify the plains inversion, allowing the meso-$\alpha$-scale upbranch to be concentrated and dominated by the meso-$\beta$-scale updraft where the inversion is weakest or non-existent. Hence, PDS circulations, regardless of their origin, can have a pronounced, and deterministic influence on both the initiation and propagation of convective systems, and interactions among PDS circulations of varying origin can also be expected to influence the behavior of convective systems.

## 2.3 Summary

Previous work in observing and numerically simulating extreme precipitation has led to widely varying theories and conceptual/physical models to explain the peculiar characteristics of these events. Common to all of these ideas are mechanisms which attempt to explain a.) the sustained, heavy precipitation rates from the storm system, and b.) the quasi-stationary character of the convective system. In addition, each of the theories invokes microphysical properties of the storm as critical not only to the precipitation production but also to the storm movement. However, the models proposed differ significantly in areas such as the role of melting, evaporation, and downdraft function or existence. Of course, there is no reason, at this point, to believe that all flash flood producing storms are alike in their dynamics and microphysical characteristics or that a single physical model can adequately explain all events. Therefore, it is not correct to view the differing storm models as being conflicting or inconsistent. In fact, in the context of the original events for which conceptual models were proposed, it isn't even correct to propose that these models are scientific hypotheses since they cannot be completely disproved. This is true for the same reason the original authors could not prove them correct: the observational evidence required for each case is absent. Hence, it is fair to say that at this stage of scientific inquiry, that this area of science is one that is still in the era of discovering plausible truths but not absolute truths.

The pertinent question that must be answered before proceeding is that of whether or not numerical investigations even consider all of the primary factors that would differentiate one model of storm evolution from another. Section 2.2 discussed previous research on the influence of soil moisture on convective initiation and boundary layer evolution. It was suggested from that body of work that convective rainfall has the potential to be strongly influenced by heterogeneous surface characteristics. It is natural to ask whether surface characteristics such as soil moisture can fundamentally change the nature of a flash flood simulation. Firstly, this should be investigated in terms of severity and even the existence of a flash flood event in the model solution. Secondly, an investigation should address the possibility of producing ambiguous or sufficiently different results with respect to the conceptual model that would be used to characterize the model-produced storm system. These are the concerns that arise naturally from the overview presented and the objective of this thesis is to quantify the effects of soil moisture variation for atmospheric initial conditions which correspond to a potential flash flood producing environment. The initial conditions used in this thesis correspond to the 1997 Fort Collins flash flood.

# 3

# Fort Collins Flash Flood of 1997: An Overview

## 3.1 Introduction

On the evening of 28 July 1997, an extreme rainfall event in Fort Collins, Colorado produced severe local flooding resulting in five fatalities and over one hundred million dollars in property damage. Thirty-seven centimeters (14.5 inches) of precipitation were recorded in southwest Fort Collins between 1600 MDT 27 July and 2300 MDT 28 July. Over 25 cm (10 in) of this fell over southwest Fort Collins during the 5.5 hour period beginning at 1730 MDT July 28 and ending at 2300 MDT (Doesken and McKee, 1998). The precipitation recorded at the Colorado State University observation station set new 1-day, 2-day, 3-hour and 6-hour precipitation records.

During the Presidential Declaration Incident Period (July 28-August 12, 1997), thirteen counties, shown in Figure 3.1 below, were declared federal disaster areas (State of Colorado and FEMA, 1997). The Fort Collins flood was not the most intense flood experienced during this period. On the evening of July 29, a larger storm developed in Weld County and western Logan County (Figure 3.1), bringing 38.4 cm (15.1 inches) of rain to the Pawnee Creek drainage basin and covered a significantly larger area than that of the Fort Collins storm (Doesken and McKee, 1998). Hence, the period in which the Fort Collins flood occurred was characterized by heavy, flooding rainfall over numerous areas in the eastern half of Colorado. Human and hydrological factors however made the Fort Collins storm the most damaging in terms of human life and property and was the most completely documented storm, observationally, of those that occurred during the week of July 28.

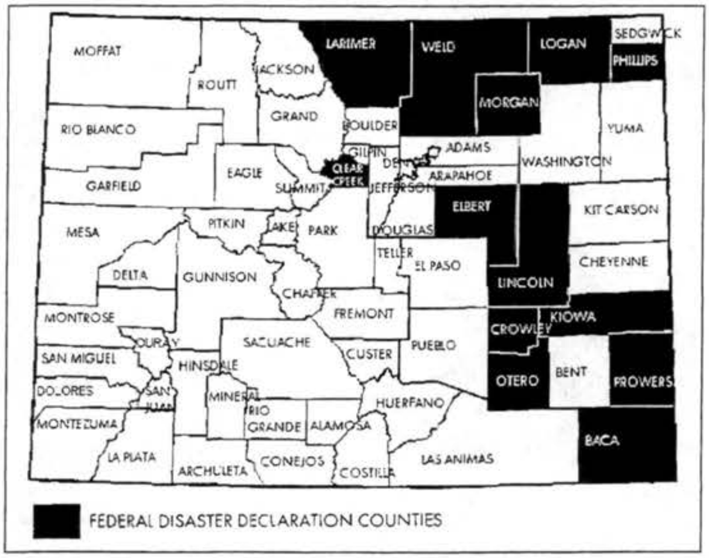


**Figure 3.1** Federal disaster declaration counties included in Presidential Declaration DR-1186-CO. From State of Colorado and FEMA (1997).

Additional observations of the Fort Collins flood and the meteorological environment are presented in Chapters 5 and 6 part of evaluating the simulations, and therefore this chapter serves only as a brief overview of the event. In the following sections, two time coordinates are used — Zulu (Z) and Mountain Daylight Time (MDT) — with Zulu exceeding MDT by 6 hours. Local sunrise on 28 July 1997 occurred at 0554 MDT (1154Z) and sunset occurred at 2019 MDT (0219Z) with twilight remaining until 2054 MDT (0254Z, July 29) (U.S.N.O. Astronomical Applications).

## 3.2 Meteorological Overview of the Fort Collins Flood

### 3.2.1 *Synoptic conditions*

The Fort Collins event occurred on the second consecutive day of rainfall in northeastern Colorado, after a surface high-pressure system moved southward from Canada producing moist, easterly, upslope flow into the Front Range foothills. Figures 3.2 and 3.3 show the surface and 500 mb NCEP analyses for 00Z, 29 July, at the beginning of the rains which ultimately led to the flooding. At the surface, a strong high-pressure system was centered in southern Manitoba, Canada producing easterly and northeasterly flow in the Central Plains and eastern Colorado. An elongated region of low-pressure extended from western Mexico, northward to Oregon. Temperatures in the northeastern quarter of Colorado ranged from the upper-sixties (°F) along the Front Range to mid-seventies in the High Plains of Colorado with dewpoint temperatures in the lower to mid-sixties (°F) throughout eastern Colorado. Like the Big Thompson and Rapid City floods, very moist air at the surface was being forced into a major orographic barrier on the southwestern periphery of surface high-pressure. However, while the Big Thompson event was observationally linked to the passage of a secondary front along the Front Range (Maddox et. al., 1978), no similar mesoscale or synoptic-scale feature has been identified observationally in the vicinity of Fort Collins prior to the flood event (Petersen et. al, 1999). By 00Z, 29 July, the only identifiable surface front was located in New Mexico, roughly 500 km south of Fort Collins.

At 500 mb, the center of the monsoon ridge was located over the Oklahoma-Texas border area. Three low-pressure centers, one located just off the coast of California, another off the southwest coast of Canada and another over Quebec, Canada resulted in a

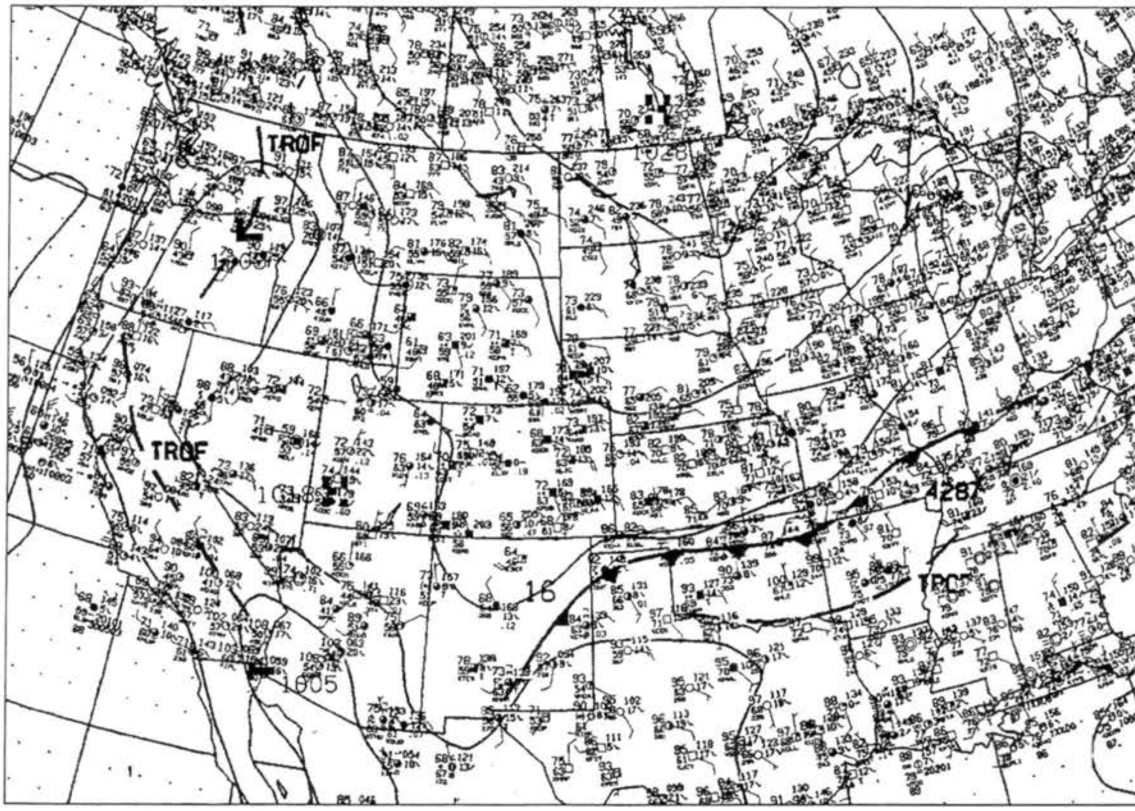


**Figure 3.2** NCEP surface analysis for 00Z, 29 July 1997. Solid lines are reduced mean-sea-level pressure isobars at 4 mb intervals.

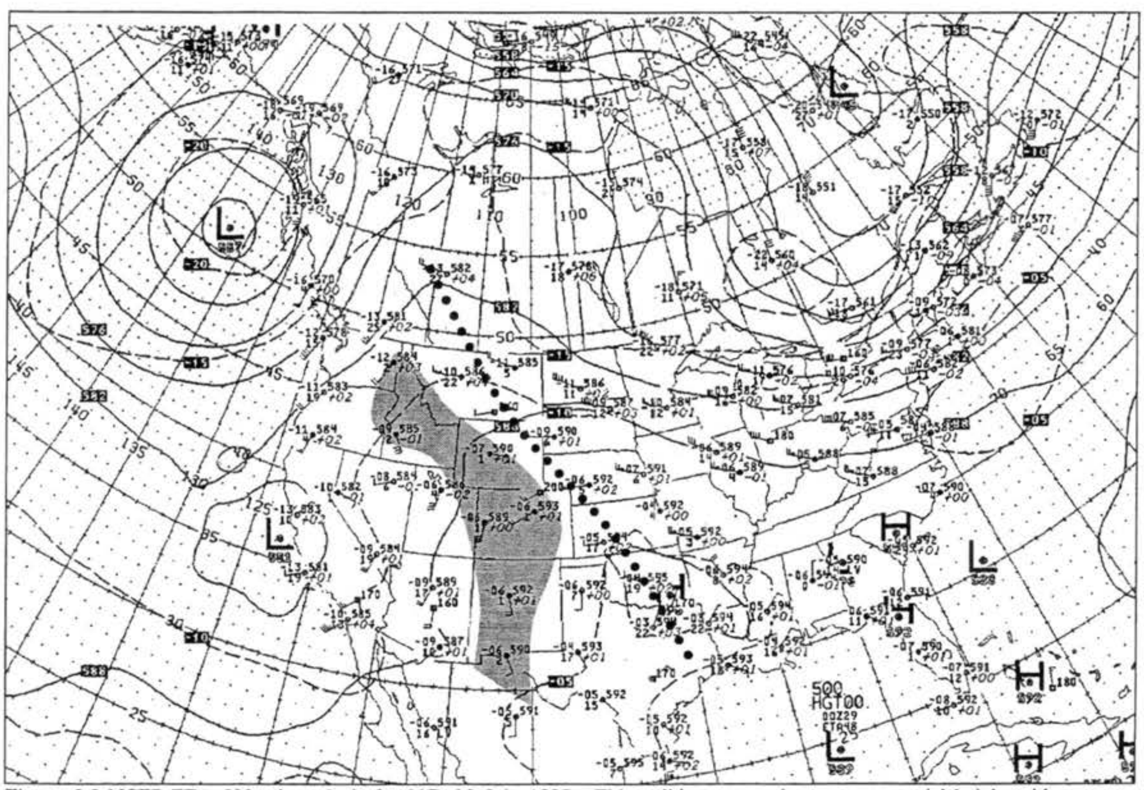


**Figure 3.3** NCEP ETA 500 mb analysis for 00Z, 29 July 1997. Thin solid contours denote geopotential height with a contour interval of 6 dm. Thin dashed contours denote temperature with a contour interval of 5°C. Thick dotted annotation line shows location of ridge axis. Shaded annotation denotes approximate area of dewpoint depression ≤ 2°C.

negatively-tilted ridge axis extending from Texas to Montana. Southerly flow with windspeed varying between 15 and 30 kts was present over Arizona, New Mexico, western Colorado and Utah, along the western edge of the monsoon high. Denver was located just west of the ridge axis and measured a 15-kt southwesterly wind at this level. The midlevel air overlying the Rocky Mountains in New Mexico, Colorado and Wyoming was very moist with little temperature variation and 1°C dewpoint depressions at all rawinsonde sites in these states. In addition, the 00Z, 500 mb analysis suggests the existence of a shortwave in northeastern Utah. This is supported by a similar and more pronounced feature in the Nested Grid Model (NGM) 700 mb, 00Z analysis, which shows a shortwave in the same location, extending into northeastern Colorado (See Figure 5.4).

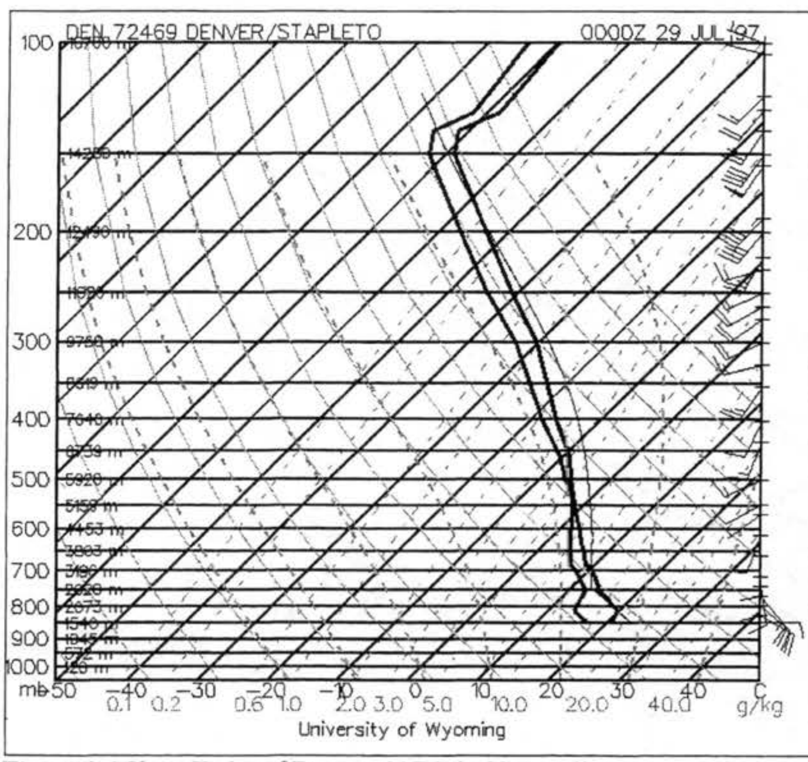

**Figure 3.4** Skew-T plot of Denver, 00Z July 29 sounding.

The 00Z 29 July Denver sounding is shown above in Figure 3.4. This sounding shows near saturation throughout most of the troposphere. A nearly isothermal layer existed between the surface and 810 mb. A conditionally unstable lapse rate existed between the top of the stable layer at 810 mb to 500 mb and from 460 mb to 400 mb. The LCL and LFC in this sounding are 745 mb and 690 mb, respectively, yielding 24 J/kg of convective inhibition (CINH). The equilibrium level was at 180 mb resulting in 703 J/kg of CAPE. Hence the troposphere was moderately unstable with a relatively low LCL and very little work would be required to release this instability.

The vertical wind profile in the Denver sounding veers with height with southeasterly winds between 10 and 20 kts (5-10 m/s) in the lowest 500 m. Winds between 725 and 400 mb were at or below 15 kts (7.6 m/s) and predominantly southwesterly. Above 400 mb, windspeed generally increased with height attaining values between 20 and 50 kts (10.2-25.5 m/s) with little directional shear. The wind profile and CAPE yield a bulk-Richardson number (BRN) of 15.8. A modeling study by Weisman and Klemp (1982) indicated that a BRN of 15 is marginal, and on the low end, for the development of rotational characteristics in thunderstorms. However, simulations in the latter reference failed to produce either secondary (multi-cell) or split-storms for CAPE values less than 1000 J/kg. Therefore, this modeled relationship between BRN and storm structure can be applied loosely, at best, in the context of the Denver sounding.

Comparison of Figure 3.3 with Figure 2.1 shows that the Fort Collins flood is a Type I event (see Section 2.1.1). The Lifted Index (LI) for the 00Z, 29 July Denver sounding is -2.5 compared to an average of -4 for the Type I event. Precipitable water in the Denver sounding was 3.81 cm, which is 60% higher than the Type I average of 2.39

cm (Maddox et. al., 1980). The late-July median precipitable water at Denver is approximately 1.8 cm with precipitable water exceeding 2.9 cm only 5% of the time (McKee and Doesken, 1997). Hence, conditional instability was not astonishingly high, but rather tropospheric moisture content and weak mid-level winds were the most outstanding features of the Denver sounding.

### 3.2.2 *Precipitation overview*

Figure 3.5 below shows the time series of accumulated precipitation at Christman Field, located in northwest Fort Collins, for the time period between 0000 MDT and 2400 MDT on 28 July. Intermittent precipitation had occurred in western Fort Collins during the night, leading to an accumulation of 5.0-6.5 cm (2.0-2.5 inches) of rainfall by 0700 MDT. A final morning rainfall occurred between 0815 MDT and 1000 MDT in which just over 3.8 cm (1.5 inches) of rain fell at Christman Field. By noon, the rains in Larimer County had ended and the town of Laporte, located just to the northwest of Fort Collins received 15-20 cm (6-8 inches) of precipitation. The eastern half of Fort Collins, however, received only 1.2-1.9 cm (0.5-0.75 in). (Doesken and McKee, 1998)

At approximately 1800 MDT (00Z, 29 July) precipitation commenced in western Fort Collins after a 7.5-hour hiatus. The first phase of precipitation was associated with two small convective systems that passed over Fort Collins and moved to the north-northeast of the city. Between 1900 and 1930 MDT a second phase of heavy rainfall occurred followed by a brief decrease in rain intensity until 2000 MDT. At 2000 MDT a third area of heavy rainfall approached Fort Collins from the southwest. This convective system became quasi-stationary over southwest Fort Collins until approximately 2230

MDT. During this last phase of precipitation, approximately 12.75 cm (5.0 inches) of precipitation fell at Christman field. (Petersen et. al., 1999)

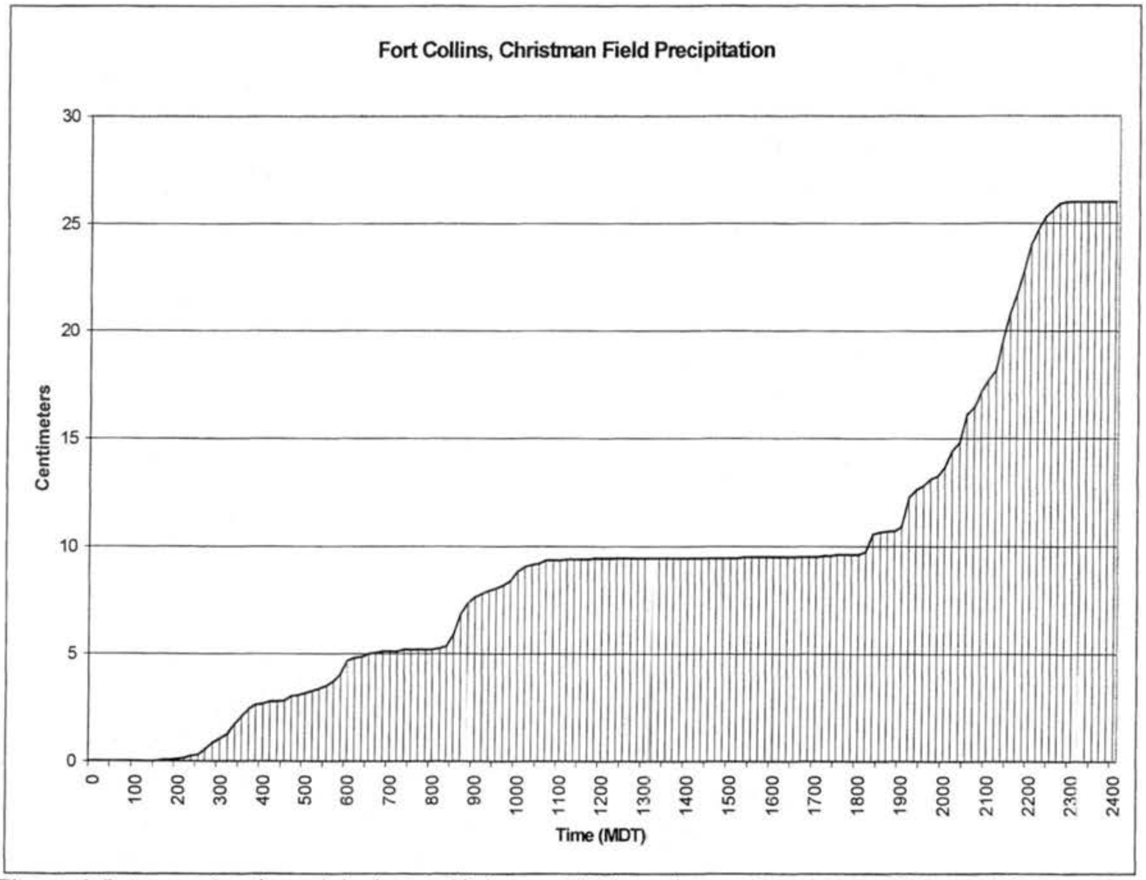


**Figure 3.5** Accumulated precipitation at Christman Field starting at 0000 MDT, 28 July 1997. Raw data courtesy of Colorado Climate Center.

Christman field, located on the northwest side of Fort Collins, did not experience the heaviest rains that evening. Rather, the intersection of Drake Rd. and Overland Trail in southwest Fort Collins was located at the center of maximum accumulated precipitation. Figure 3.6 below shows the accumulated rainfall analysis for Fort Collins and surrounding area for the time period between 1730 MDT and 2300 MDT, 28 July. This analysis reveals a 25-28 cm (10-11 inch) maximum located in southwest Fort Collins at the upstream end of Spring Creek. This creek was the primary water source for a detention basin in central Fort Collins, which was breached shortly after the rainfall ended in southwest Fort Collins, resulting in five fatalities. The east-west isohyet gradient on the west side of the precipitation maximum in Figure 3.6, is approximately 4.88 cm/km (1.92 in/km). This demonstrates the highly localized nature of this flood with the area immediately to the east of the hogbacks, along the western edge of Fort Collins, receiving the largest amounts of precipitation. It has been speculated that the steep topography gradient at the base of the foothills may have played an important role in maximizing low-level convergence and localizing the precipitation along the western side of Fort Collins. (Petersen et. al., 1999; Doesken and McKee, 1998)

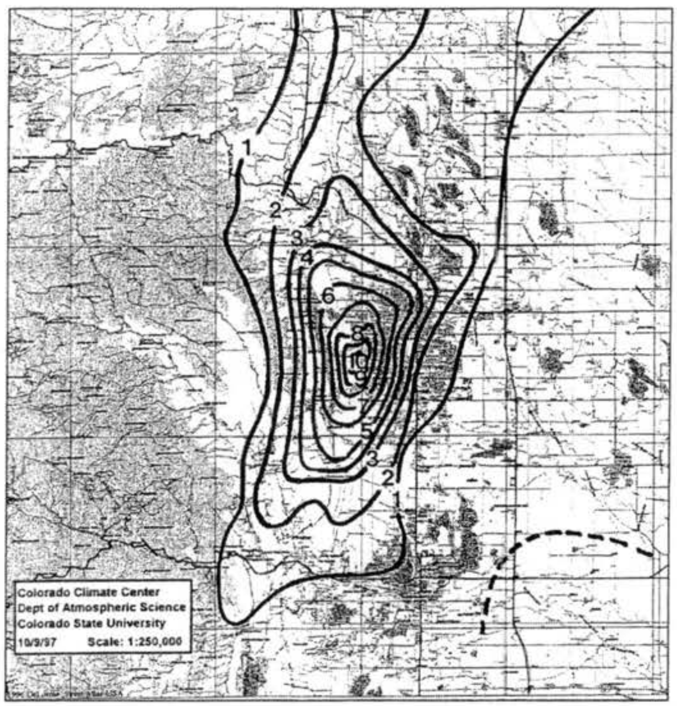


**Figure 3.6** Accumulate rainfall analysis for the time period 1730-2300 MDT, 28 July 1997. Thick contours are isohyets contoured at 1 inch (2.54 cm) intervals. From Doesken and McKee (1998).

### 3.2.3 *Storm Characteristics*

As in most flash flood cases, the flood producing precipitation in the Fort Collins event resulted from the combination of very high precipitation rates, likely exceeding 12-15 cm/hr (5-6 in/hr), and a quasi-stationary system characteristic (Doesken and McKee, 1998). Pedersen et. al. (1999) provide a detailed radar analysis of the Fort Collins storm and the following paragraphs summarize some of their findings.

The system that affected the Fort Collins area reached maximum precipitation intensity and remained quasi-stationary throughout the last 1.5 hours of the event, ending at 2230 MDT. However, the individual cells within the system propagated to the north-northeast at approximately 6-8 m/s (13-18 mph), with new cell generation occurring on the southern and southeastern periphery of the system. Between 2000 MDT and 2200 MDT, convective systems to the southeast of Fort Collins were propagating primarily northeastward between 5 and 10 m/s (11-22 mph), while the Fort Collins system remained nearly stationary. (Pedersen et. al., 1999)

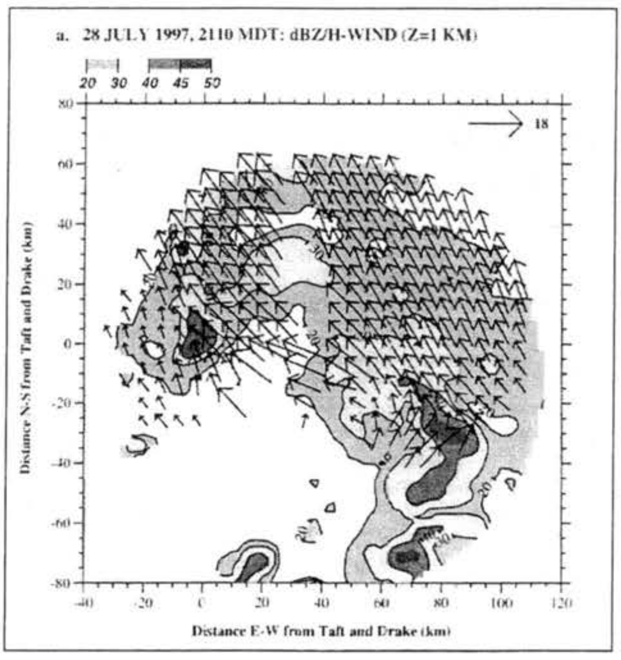


**Figure 3.7** Radar reflectivity and 1-km AGL winds at 2110 MDT. Vector scale is in m/s. From Petersen et.al. (1999).

One factor that may have had an influence on the intensification and stationary nature of the Fort Collins storm was the development of a bow echo west of Denver after

1800 MDT. This system propagated northeastward at approximately 8 m/s (18 mph) between 1900 and 2100 MDT. At 2100 MDT the bow-echo was located approximately 90 km to the southeast of Fort Collins. The 1-km (AGL) flow around the northern edge of this bow echo, shown in Figure 3.7 above, contained a band, or jet, of enhanced easterly-component wind, terminating at the Fort Collins convection. At 300 m AGL and approximately 6 km to the east of the 50-dBZ reflectivity maximum, the southeasterly jet achieved a maximum radial velocity between 16 and 20 m/s (36-45 mph) (Figure 10 in Petersen et. al., 1999). Petersen et. al. (1999) propose that this low-level, meso-scale jet, may have been a significant forcing mechanism for storm intensification between 2000 and 2200 MDT, by enhancing low-level convergence over Fort Collins.

Pedersen et. al. (1999) analyzed multi-parameter data obtained that night from the dual-polarization CSU-CHILL radar, located approximately 40 km to the southeast of Fort Collins. Information about hydrometeor size, shape and thermodynamic phase was partially provided by specific differential reflectivity ($Z_{dr}$), linear depolarization ratio (LDR), and specific differential phase ($K_{dp}$). Using a "blended" relationship between rainfall rate, total reflectivity, $Z_{dr}$, and $K_{dp}$, the surface rain-mass flux was estimated for a stationary circle with 10-km radius, centered at Drake Rd. and Taft Hill Rd. near the accumulated precipitation maximum. The estimate showed three primary peaks of 13, 19 and $21.5 \cdot 10^5$ kg/s, in chronological order. These peaks were separated by approximately 1-1.5 hour intervals. The peak CHILL radar-estimated precipitation rate was 110 mm/hr (4.3 in/hr), using the blended relationship as noted above, and core diameters with reflectivity between 48 and 51 dBZ were typically 1-2 km during the last hour of precipitation. It should be noted however that the CHILL-radar estimate of storm total precipitation using the blended relationship underestimated the gauge maximum by approximately 20%.

Petersen et. al. (1999) inferred storm microphysical structure for the time period 2100 through 2130 MDT using the multi-parameter radar data. The highest reflectivity throughout the storm was typically located at or just above the environmental 0°C level, which was located approximately 3.4 km AGL (4.9 km MSL). However, mean reflectivity values of greater than 35 dBZ were generally located below or near the height of the -10°C level (7.0 km MSL). Hence, like the Big Thompson storm, the Fort Collins convection also exhibited a low-echo-centroid, indicative of efficient production and removal of precipitation from the updraft in the lower portion of the cloud. It was inferred that 2-3 mm raindrops were present in the 2-3 km AGL layer, on the eastern edge of the reflectivity core, while millimeter-sized raindrops were lofted to temperatures colder than 0°C within the updraft, followed by freezing. The radar-estimated ice-mass fraction increased from 0.1 to 0.5 in the 1-km interval centered around 3.5 km AGL. Petersen et. al. (1999) proposed that raindrops lofted above the 0°C level likely froze and underwent substantial accretional growth before descending on the northwest side of the updraft. It should be noted that no hail or frozen precipitation was reported for the Fort Collins storm (Petersen et. al., 1999). Hence, the complete melting of high- and intermediate-density ice-particles, such as hail and graupel, before reaching the ground, may have contributed to a significant portion of the rainfall observed at ground level. The Cheyenne NEXRAD radar, operated by the National Weather Service, recorded reflectivity values greater than 10 dBZ up to heights of 12-14 km AGL or 13.5-15.5 km MSL during the periods of peak precipitation. In addition, the radar echo-top was located

5-10 km northeast of the low-level reflectivity core, indicating a northeastward storm tilt. (Petersen et. al., 1999).

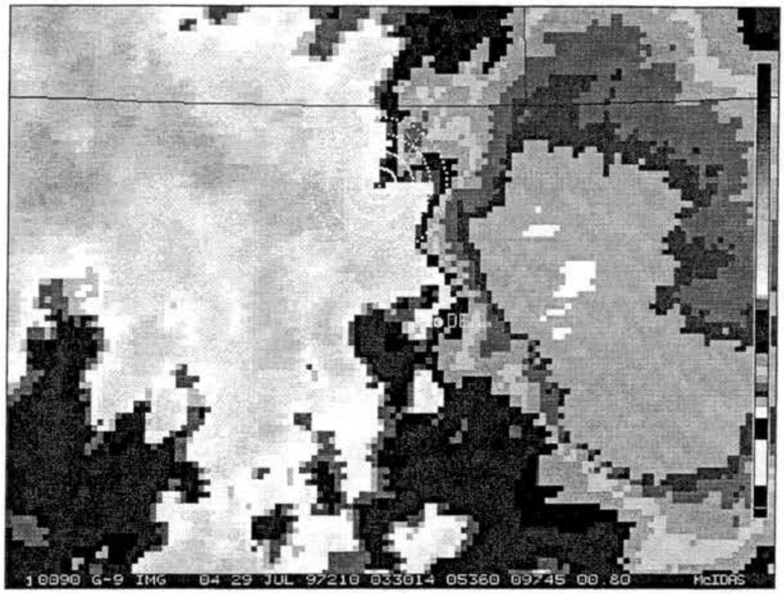


**Figure 3.8** GOES-9, oblique-stereographic projection, infrared image at 2130 MDT, July 28 (0330Z, July 29). Fort Collins is located at the center of the concentric circles. Radii are at 10-km intervals. Denver is shown by the light colored dot immediately to the west of "DEN". "X" denotes a 207K brightness temperature at 30 km radius (before correction).

Comparing this echo-top measurement to the 00Z July 29 Denver sounding indicates that the Fort Collins storm did achieve cloud top heights approaching that of the tropopause which was located at 14.2 km MSL. The 2130 MDT, GOES-9, channel 4 (infrared) image is shown in Figure 3.8. The coldest cloud top brightness temperature, marked with an X, was 207K (-66.15°C) located, in this depiction, approximately 30 km to the northeast of Fort Collins. However, due to the equatorial orbit of this satellite, coupled with its westward displacement from the longitude of Fort Collins, a parallax correction is required. This correction was computed by the author using McIDAS-X software and amounts to $-9.9487 \cdot 10^{-3}$ degrees of latitude and $-1.1562 \cdot 10^{-2}$ degrees of longitude per kilometer of height above MSL. At the latitude of Fort Collins, this correction is 1.47 km, along an azimuth of 221.43°, per kilometer of height. Using the Denver sounding as an *estimate* of the height of the 207K cloud-top temperature, a height of 13.8 km MSL was estimated. This yields a correction of 20.3 km toward the southwest (221.43°). Hence the true location of the minimum cloud top temperature is approximately 10 km to the northeast of Fort Collins, in general agreement with the Cheyenne NEXRAD echo-top measurement both horizontally and vertically. No estimates of updraft velocities were provided in the published observational studies of the Fort Collins storm.

## 3.3 Summary

Between July 27 and August 12, 1997, 13 counties in eastern Colorado were declared federal disaster areas due to severe flooding caused by convective precipitation. One of the most severe floods occurred in Fort Collins on the night of July 28, 1997. The Fort Collins storm produced over 10 inches (25-26 cm) of rain in a 5.5 period ending at 2230 MDT. This storm was characterized by quasi-stationary movement during the last 1.5 hours of the event. Interactions with proximate convection and topography were identified as possible influences on both the intensity and motion of the system. Radar inferences about microphysical properties of the storm indicated that the complete melting of frozen droplets, hail, and graupel, before reaching the ground might have been responsible for a significant portion of precipitation recorded at ground gauges. Storm top estimates provided by radar, and analysis of infrared satellite imagery indicates that the Fort Collins storm reached heights between 13 and 15 km MSL, 5-10 km northeast of Fort Collins, during the most intense phase of the storm.

# 4

# Model Configuration

## 4.1 Model Overview

The atmospheric model used in this research is RAMS Version 3b (Pielke et al., 1992). This research tool has been employed for simulating a wide-range of phenomena in both research and operational environments. Applications include investigations of tornadogenesis (Grasso and Cotton, 1995), MCS evolution (McAnelly et al., 1997), pollutant dispersion (Grossi et. al., 1998), land surface-atmosphere interactions (Vidale et al., 1997), and real-time operational forecasting at the Forecast Systems Laboratory (FSL) (Snook et al., 1995). The versatility of RAMS stems from its numerous options regarding surface, moist-microphysics, turbulence, radiation, and surface-process parameterizations, in addition to its interactive grid-nesting capability (Clark and Farley, 1984) and initialization options. Features relevant to the simulations described in this work are described below. Details concerning the use of model options on specific grids and at particular times are discussed in section 4.2.2.

**4.1.1** ***Governing equations and numerics***

The simulations utilize the non-hydrostatic governing equations for momentum and mass continuity. Leapfrog time-differences are used for velocity components and pressure, while forward time-differencing is used for all other quantities. In addition, resolvable acoustic disturbances are simulated on a short time-step using a standard time-splitting technique (Tripoli and Cotton, 1982). Advection is implemented in flux-conservative form using either second-order centered or second-order upstream spatial differences depending on the time-differences used as described above. The stencil used for the model variables is the Arakawa C grid (Mesinger and Arakawa, 1976).

The model grid utilizes an oblique-stereographic projection in the horizontal and a terrain following vertical coordinate, $\sigma_z$: $\sigma_z = H \cdot \frac{(h - h_s)}{(H - h_s)}$, where h is geometric height, $h_s$ the lower boundary geometric height and H is the upper boundary geometric height, each referenced to sea level (Gal-Chen and Somerville, 1975). Nested grids are implemented using the two-way interactive nesting technique of Clark and Farley (1984), and Clark and Hall (1991).

Klemp and Wilhelmson (1978) boundary conditions are applied for the normal velocity components at the lateral boundaries of the model domain. This minimizes reflection of gravity wave-like disturbances (phase speed ~ 20-40 m/s) at the lateral domain boundaries. Other variables are assumed to have a vanishing gradient at inflow boundaries and a constant gradient at outflow boundaries. At the top boundary, a rigid wall condition is assumed (vertical velocity is assumed to be zero).

**4.1.2 *Parameterizations***

Parameterizations for moist-convection, radiative transfer, turbulent diffusion, surface-layer processes, and soil and vegetation interactions are also included and utilized. Turbulent diffusion is parameterized using K-closure theory, the diffusion coefficients for scalars and momentum calculated from the basic Smagorinsky (1963) scheme with hydrostatic stability modifications for the vertical diffusion coefficients (Hill, 1974; Lilly,1962). Surface layer fluxes of heat, moisture and momentum, each of which are determined both by atmospheric and vegetation/soil layer variables are computed using the scheme of Louis (1979). The soil model is based on that of Tremback and Kessler (1985). The soil class in the current simulations is spatially invariant and corresponds to the sandy-clay-loam USDA textural class (USDA, 1951). A vegetation model, based on the work of Avissar and Mahrer (1988), is used to calculate vegetation layer variables. The vegetation parameters are based on the vegetation classification used in the Biosphere-Atmosphere Transfer Scheme (BATS) (Dickinson et. al., 1986). Radiative transfer parameterization is accomplished with a long- and short-wave radiation scheme developed by Chen and Cotton (1983). In addition to molecular scattering, ozone, and water-vapor influences, this scheme also parameterizes the effects of water condensate on the radiative budget.

Convective parameterization is performed by a modified-Kuo scheme (Kuo, 1974; Tremback, 1990). Microphysics calculations are performed using the bulk one-moment scheme described in detail in Walko et al. (1995). This scheme allows for water in the form of vapor, cloud droplets, rain, pristine ice, snow, aggregates, graupel, and hail; each category is assumed to be distributed according to a generalized gamma distribution.

## 4.2 Simulation Specifications

This section describes the organization of the simulation in terms of grid configuration, initialization method and user-specified parameters. Aside from the differences in the initial soil-moisture distribution described in Section 4.2.2, the following specifications apply to all simulations.

### 4.2.1 *Grid configuration*

The simulations utilize four telescopically nested grids, which allows for resolution of synoptic-, meso-, and convective scale motions in the respective domains. The geometry and time-step information for each grid is shown in Table 4.1 below. The grids are depicted in Figures 4.1 and 4.3 below.

| Grid | $\Delta x = \Delta y$ (km) | $\Delta t$ (sec) | Center (lat, lon) | No. of Gridpoints X | No. of Gridpoints Y |
|---|---|---|---|---|---|
| 1 | 80.00 | 90.00 | (40.01°N, 105.09°W) | 33 | 28 |
| 2 | 20.00 | 45.00 | (40.01°N, 105.09°W) | 54 | 38 |
| 3 | 5.00 | 15.00 | (40.01°N, 105.09°W) | 70 | 70 |
| 4 | 1.67 | 5.00 | (40.20°N, 104.09°W) | 89 | 110 |

**Table 4.1** Grid specifications.

Each grid has 37, $\sigma_z$ levels, with a spacing of 100 m at the ground, expanding geometrically with an expansion ratio of 1.12. The upper limit on the vertical grid spacing was set at 800 meters, which occurs at 7.5 km, resulting in a model top of 19.5 km. The topography for each grid was interpolated from the United States Geological Survey (USGS), 30-second dataset ($\cong$ 900m). It is worth emphasizing that the topography was interpolated from this dataset to each grid in the simulation and hence is at the native grid resolution on each respective grid. The topography on grids 2 and 4 are shown in Figures 4.2 and 4.4 respectively. The soil model grids have horizontal grid structures identical to the respective atmospheric model grids described above. Each soil-model grid contains 11 vertical levels that extend to a maximum depth of 0.5 meters.

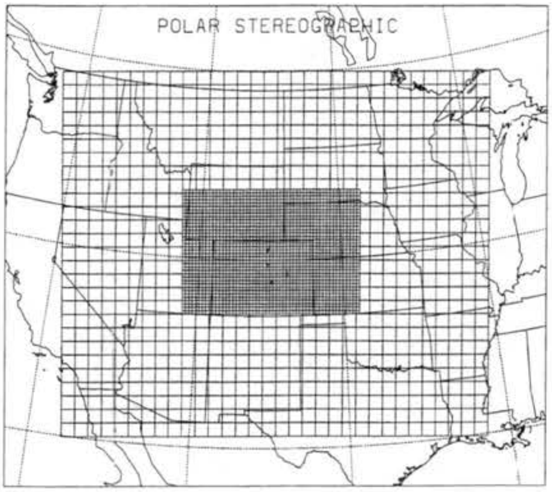


**Figure 4.1** Locations of grids 1 and 2.

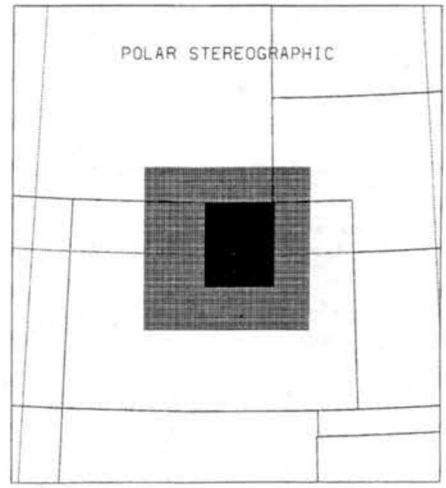


**Figure 4.3** Locations of grids 3 and 4.

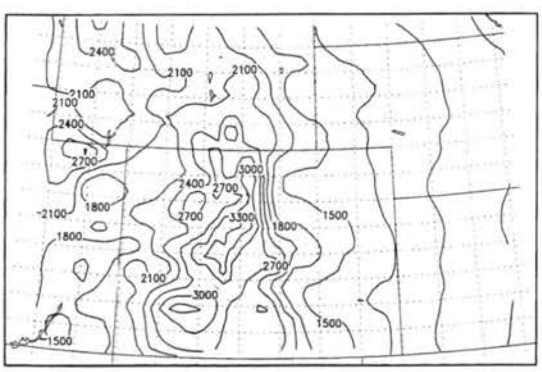


**Figure 4.2** Grid 2 elevation. Contour interval is 300 meters.

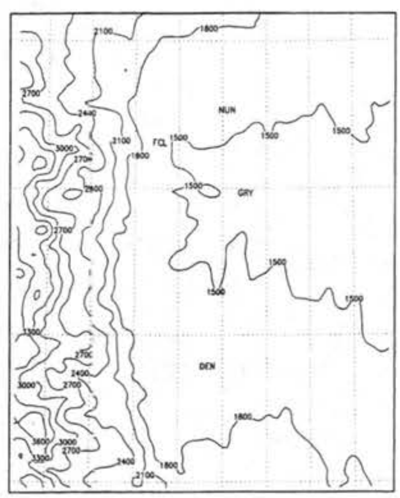


**Figure 4.4** Grid 4 elevation. Contour interval is 300 meters.

### 4.2.2 *Initialization and integration method*

The initial atmospheric fields were supplied from three sources. The first of these was the 1200Z, 28 July, Rapid Update Cycle (RUC) operational forecast model analysis. The other two datasets consisted of NCAR archived surface and rawinsonde observations for the same time. All three of these sources supply temperature, pressure, humidity, wind direction, and wind speed, to be interpolated onto the model grids. These datasets were analyzed onto grids 1 and 2 using the objective analysis package included in RAMS (Tremback, 1990), with some modifications to accommodate the grid structure of the RUC analysis. The surface and rawinsonde data augment the RUC analysis with measurements near the surface, and supply initialization data at points between the uppermost level of the RUC analysis, which lied around 14.0 km, and the domain top (~19.5 km).

Two simulations were performed, differing only in the method of initializing soil moisture. Simulation A was initialized with the soil moisture fields taken from the operational 48-km ETA forecast model analysis. The ETA soil moisture analysis consisted of two volumetric soil-moisture content fields, for the regions corresponding to 0-10 cm and 10-100 cm soil layers. These were assigned to the RAMS soil model levels according to the depth range in which each RAMS soil level existed. Simulation B was initialized using the Antecedent Precipitation Index (API) method of deriving soil moisture (Saxton and Lenz, 1967), based on precipitation observations in the NCDC TD3240 United States Control Cooperative Precipitation Dataset. The API method and the ETA soil-moisture dataset are described in detail in Section 4.3.

The model is integrated from 1200Z, 28 July to 0500Z, 29 July. Throughout the entire simulation, Davies nudging (Davies, 1983) is used on the lateral boundary of grid one, and the upper 4.5 km of all grids. This technique introduces an additional tendency term to the temperature, pressure, humidity, and wind variables to force these variables toward user-specified values with a user-specified relaxation time. The user-specified data values, in this case, correspond to 00Z 29 July and 12Z 29 July and were generated using the same method as that used to generate the initial conditions. The upper-domain nudging is introduced, as an analogue to Rayleigh friction, which eliminates unwanted gravity wave reflection from the top boundary.

Each simulation consisted of three stages of integration. The first of these was the time allocated for model spin-up from 1200Z 28 July until 1500Z 28 July. During this period, considerable undulations occurred in the geopotential height fields at all levels, associated with the model adjustment. By 1500Z these fields reached a more quiescent state. Until 1500Z, microphysics parameterization was simplified on all three grids to allow cloud-water as the only form of water condensate throughout the spin-up phase. This was done to avoid inadvertent modifications to the initial soil-moisture distribution due to spurious precipitation associated with model adjustment dynamics. At 1500Z, the second stage of integration began in which the full microphysics parameterization was activated on all three grids and the modified Kuo cumulus parameterization was activated on grid 1. As stated in section 4.1.2, all condensed water is distributed according to a generalized gamma size distribution (Walko et. al., 1995). The width parameter, $\nu$, was set to 2.0. A mean diameter of 1.0 mm was specified for rain, graupel, snow and aggregates and 3.0 mm for hail. Cloud droplet concentration was set to 300 $cm^{-3}$. These microphysical parameters were not altered between the simulations.

The second stage of integration continued until 1800Z. At 1800Z, grid four was activated, taking its prognostic fields by interpolation from Grid 3. This corresponds to a time before deep, moist-convection initiated on Grid 3, at the location where Grid 4 was to be located. Integration resumed with full, moist microphysics active on all grids. This third and final stage of the integration continued until 0500Z July 29, at which time the simulations were terminated. This corresponded to a time after the precipitation associated with the Fort Collins flood had ended in reality, and there was no indication of further heavy precipitation occurring in either simulation after this point. During this final stage, each time-step (90 sec) required approximately one half hour of CPU time on an IBM RISC System/6000 7248, and required 144 MB of RAM. Thirty-minute (model time) analysis output during phase 1 and 2 of integration, 15-minute output during phase 3, and hourly history file output required 2.4 GB of media storage, per simulation.

## 4.3 Soil Moisture Initialization

### 4.3.1 *ETA-derived soil moisture*

The initial soil-moisture distribution for Simulation A is taken from the 12Z 28 July 1997 analysis of the operational ETA model. The information presented in this section holds only for the date relevant to this thesis — 28 July 1997 — as the ETA components are constantly undergoing changes and improvements. At this time, the horizontal resolution of the operational "early"-ETA was 48 km in the horizontal with 38 vertical levels in the atmosphere. The 12Z ETA analysis is the end-result of a twelve-hour data assimilation cycle performed with the ETA Data Assimilation System (EDAS) (Rogers et. al., 1996). This data assimilation system is identical, in terms of model physics to the ETA operational model, but is interrupted four times, at three-hour intervals, to update the model atmospheric and microphysical fields using observational data. The final twelfth-hour update then becomes the initial condition, or analysis, for the operational run. During the data assimilation cycle, soil moisture is allowed to evolve freely via the EDAS (ETA) soil-model, simulated precipitation and surface parameterizations. No soil-moisture updates, other than those simulated by the model physics take place during the three-hourly atmospheric field updates. A description of the soil model and surface parameterizations can be found in Pan and Mahrt (1987), Janjic (1996), and Chen et. al. (1996).

The initial fields used for the first three-hour integration of EDAS are taken from the Global Data Assimilation System (GDAS), which produces 6-hourly global analyses of atmospheric and soil variables (Kanamitsu, 1989). Information about the soil and surface schemes used in the NMC global spectral model can be found in Betts et. al. (1996) and Hong and Pan (1996). The July 1997 NMC global spectral model was operated at T126 spectral resolution. This is roughly equivalent to 105-km horizontal resolution. As of July 1997, the soil moisture forecasts of GDAS were freely evolving forecasts carried from one assimilation cycle to the next with no modifications. However, upon ingestion into EDAS, the volumetric soil moisture was limited to be below a critical value due to problems noted with the ETA predicted low-level temperature field and the positive precipitation bias known to exist in GDAS at that time (Black et. al., 1997; Betts et. al., 1997).

In short, GDAS produces 6-hourly soil-moisture analyses from a continuously evolving forecast that becomes the initial condition for EDAS at 00Z 28 July. The soil-moisture field continues to evolve under EDAS according to the ETA model physics to produce the operational ETA analysis at 12Z July 28. Both the ETA (and hence EDAS) and the global spectral model (and therefore GDAS) utilize two soil layers of 0-10 cm below ground and 10-200 cm below ground. The soil moisture values from these two levels were interpolated onto the RAMS soil model grid as described previously. The 12Z, or initial, top-level soil moisture fields for Grids 1 and 3 are shown in Figure 4.5.

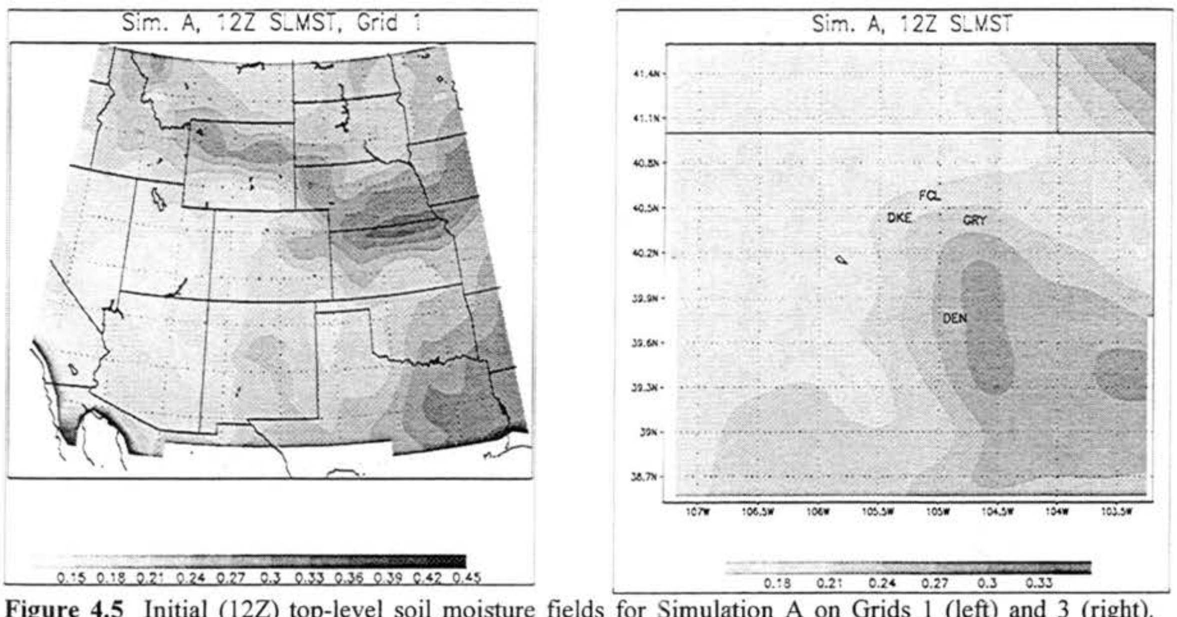


**Figure 4.5** Initial (12Z) top-level soil moisture fields for Simulation A on Grids 1 (left) and 3 (right). Volumetric soil moisture content shaded at 0.03 ($m^3$/ $m^3$). Shading scale is identical between plots.

### 4.3.2 *API soil moisture estimation*

The Antecedent Precipitation Index (API) is a measure of the depth of water contained within a given depth of soil (Saxton and Lenz, 1967). Physical processes such as precipitation and subsequent infiltration act to increase the API while evapotranspiration and percolation contribute to the decay of API. Hydrologists have developed a simple exponential model for the evolution of API: $API_i = (API_{i-1} + P_{i-1})K_{i-1}$, where the subscript $i$ labels each day, $P_i$ is the precipiation which falls and infiltrates the soil on the ith day, and $K_i < 1.0$ is the retention coefficient for the ith day. For the case of constant $K$, the API algorithm may be considered to produce a weighted sum of the antecedent precipitation events with a weighting factor $K^t$, where $t$ is the number of days between a precipitation event and the day for which the API is desired. Clearly, one's choice of initial API becomes less important as the number of days used in the calculation increases. Saxton and Lenz (1967) demonstrated that for a 90 day calculation with $K$=0.90, the choice of initial API had a negligible effect on the API at day 90.

In this study, an API value is derived for each precipitation measuring station in the NCDC TD3240 U.S. Control Cooperative Precipitation dataset with a complete daily precipitation record for the 88 days preceding 28 July 1997. The precipitation record starts at 0000 hours MST 1 May 1997 and ends at 0000 hours MST 28 July 1997. The retention coefficient used differs from the simple exponential model in that it was not constant, but rather a sinusoidal function with a one-year period exhibiting a maximum of 1.0 on 15 January and a minimum of 0.92 on 15 July. This particular functional form is based on the derived K-values in Saxton and Lenz (1967) as well as those found in Choudhury and Blanchard (1983). As noted in the latter reference, considerable error can occur with this algorithm if snow-cover is present due to the dependence of snowmelt on factors not considered in the API formulation. Therefore, this algorithm provides a questionable soil moisture estimate during the winter months in snow-covered areas or at high elevations where snow-cover can exist throughout much of the year. Additionally, Saxton and Lenz (1967) note that variations in local drainage patterns and vegetation type and coverage can also have a significant impact on the optimal retention coefficient. No correction schemes were devised for these deficiencies and hence the retention coefficient used in this study was applied uniformly in space.

During the execution of the API algorithm, the API value is not allowed to exceed the saturation value for sandy-clay-loam. For a 12-inch (30.5 cm) deep layer of soil, this corresponds to an API of 0.128 m.. Once the API value for each station is determined, it is converted to volumetric soil-moisture content and these values are analyzed onto the RAMS soil-model grids 1, 2 and 3 using the Barnes (1973) objective analysis scheme. While the depletion coefficient used is designed for determining the average 0-12 inch (0-30.5 cm) depth soil moisture (Saxton and Lenz, 1967), the API-derived values are applied uniformly throughout the soil-model depth (50.0 cm).

Thus, the complete API method used in the model initialization consists of two primary steps: 1.) Determining the API at specific stations and subsequent conversion to volumetric soil moisture content, and 2.) objectively analyzing the estimated station soil-moisture content onto the model grids. Some of the deficiencies associated with the first step have already been mentioned. However, even if one assumes that the first step provides perfectly diagnosed soil moisture content at station location, there remains the problem of extrapolating/interpolating these values onto the model grid.

The Barnes objective analysis determines grid point, or destination values, by performing a weighted average of all station, or source estimates. The weighting function used is a two-dimensional Gaussian centered at the destination point: $\eta_{ij(k)} = \frac{1}{\pi\sigma^2} e^{-\left(\frac{r_{ij(k)}}{\sigma}\right)^2}$, where $i, j$ denotes the $i$ and $j$ index of the destination grid point, $k$

denotes the $k_{th}$ source or station and r is the distance between the source and destination grid point. $\sigma$ is a user-specified parameter that represents the square root of the areally averaged value of $r^2$ and therefore specifies the width of the Gaussian and it's smoothing properties.

Thus the analyzed value at the i, jth grid point becomes:

$$API_{ij(k)} = \frac{\sum_k \eta_{ij(k)} API_k}{\sum_k \eta_{ij(k)}}. \tag{4.1}$$

In his 1973 paper, Barnes considered the continuous version of this objective analysis in which a continuous and integrable function $f(x, y)$, is smoothed to produce,

$$g(x, y) = \int_0^{2\pi} \int_0^{\infty} f(x + r\cos\theta, y + r\sin\theta)\eta(r, \sigma) r \, dr \, d\theta, \tag{4.2}$$

where $r$ and $\theta$ are polar coordinates, and $\eta$ is again the two-dimensional Gaussian with r now defined on the entire plane.

Barnes showed that if f is a simple sinusoidal function,

$f(x + r\cos\theta, y + r\sin\theta) = A\sin[a(x + r\cos\theta)]$,

then $g(x, y) = D(a, \sigma) A\sin[a(x + r\cos\theta)]$.

Hence, the phase of a pure sinusoidal function is unaffected by the Gaussian smoothing, while the amplitude is decreased by a factor, called the response:

$$D(a,\sigma)=e^{-\frac{a^2\sigma^2}{4}}=e^{-\left(\frac{\pi\sigma}{\lambda}\right)^2}\text{, where }\lambda=\frac{2\pi}{a}.$$

Thus, the continuous version of this scheme is essentially a smoothing operation that leaves the amplitude of wavelengths much larger than $\sigma$ nearly unaltered and strongly decays wavelengths much smaller than $\sigma$. One should recognize that the Barnes scheme is inherently a smoothing operation and the estimate that the discrete equation (Eq. 4.1) provides should be considered an estimate of the smoothed field given by Eq. 4.2. Typically $\sigma$ is specified by choosing a relatively high response $D$, say 0.9, and the wavelength $\lambda$ to which this response applies. This determines $\sigma$ and hence the response $D$, at all other wavelengths.

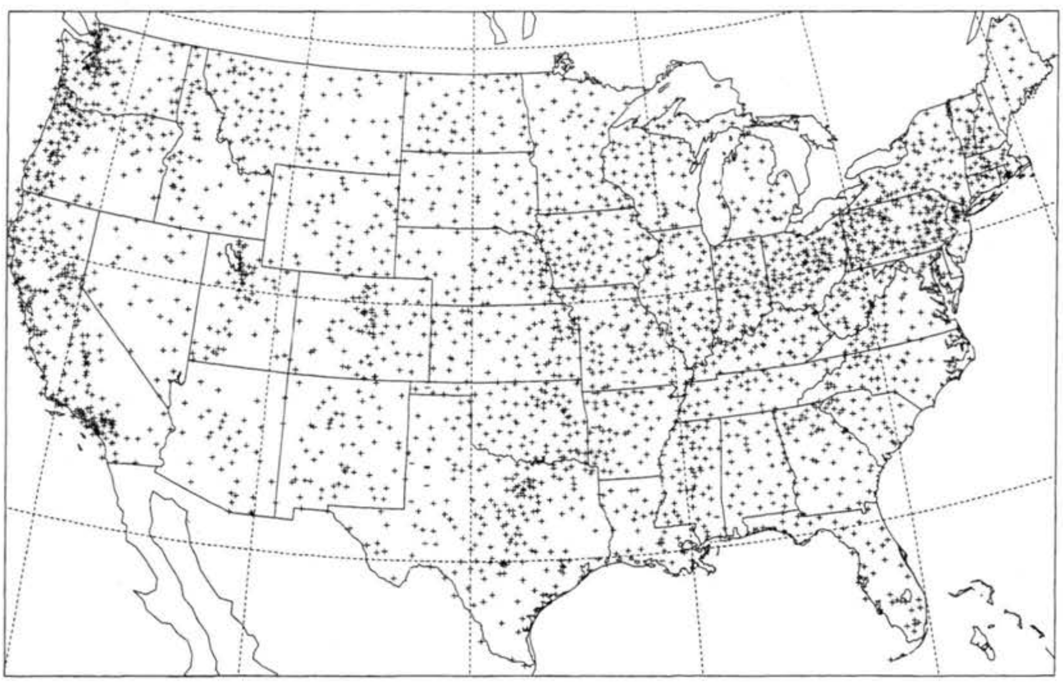

**Figure 4.6** Stations used in the API estimate of soil moisture. Each station is denoted by a '+'.

One's choice of wavelength should consider factors such as mean station or sample spacing as well as the characteristic length scale of variations in the underlying field being sampled. Figure 4.6 above shows the United States precipitation stations used in the API calculation. Within Colorado, which contains 73 stations in the NCDC dataset, the average distance between neighboring stations is 48.50 km with a standard deviation of 29.44 km. If at least four stations are required to properly sample one complete wavelength, a minimum wavelength range determined from the average and standard deviation above, is 95-390 km. Figure 4.7 shows the API derived soil moisture on grid 3 using the API method described, at 95 and 390 km. The difference between these two fields demonstrates the need for a more precise criterion in determining the proper wavelength to be used in the objective analysis.

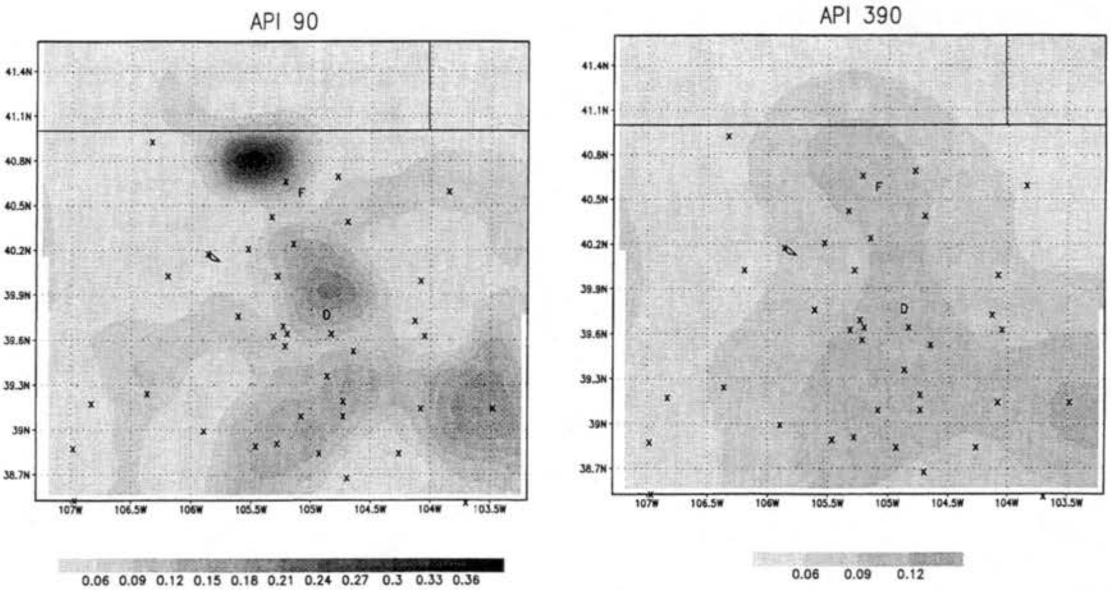


**Figure 4.7** API estimated volumetric soil-moisture content from gauge data on Grid 3 at 90 km (left) and 390 km (right) wavelength. Shading interval is 0.03 $m^3/m^3$.

For this purpose, a gridded, 5-km, 24-hour radar-estimated precipitation dataset, covering Grid 3, was used to construct a hypothetical, high spatial-structure API-derived soil-moisture estimate. The time encompassed in this dataset was 00Z 1 May 1997 through 00Z 28 July 1997. Comparison of radar derived precipitation with co-located gauge measurements indicated a tendency for radar derived precipitation estimates to exceed gauge measurements by a factor of ~1.5-3.0. In fact, using radar derived precipitation estimates in the API algorithm resulted in unrealistically large areas of full soil saturation over all of eastern Colorado and most of the central plains. Because of this complication, radar-based API estimates were not used for model initialization but rather, the gauge values were used as described above. However, for obtaining a hypothetical, high spatial-structure soil moisture field, the radar estimated precipitation was halved. The first plot in Figure 4.8, CTL 0, shows the resulting radar-derived, API estimated, volumetric soil moisture field on grid 3. Area-averaged versions of this field were created using the Barnes analysis scheme in which every grid point of CTL 0 is treated as a station measurement of soil moisture content. Each of these fields will be called CTL $\lambda$, where $\lambda$ is the wavelength retained with response of 0.9. These are also shown in Figure 4.8 along with CTL 0. The CTL $\lambda$ fields represents the closest approximation to Eq. 4.2, given $\lambda$, and are therefore constitute a control set of area-averaged soil moisture fields obtained from CTL 0.

CTL 0 was then sampled at the grid-points closest to each of the locations of the 73 Colorado precipitation gauges used in the NCDC archive that lied within grid 3. These 73 samples were then used to produce objective analyses at the same wavelengths as those in the CTL set. These fields will be called SMP $\lambda$, where $\lambda$ is again the wavelength retained with a response of 0.9. These are shown in Figure 4.9. The objective is to determine to what extent the objective analysis of a sampling of CTL 0, reproduces either CTL 0 or a smoothed version of CTL 0, namely the CTL $\lambda$.

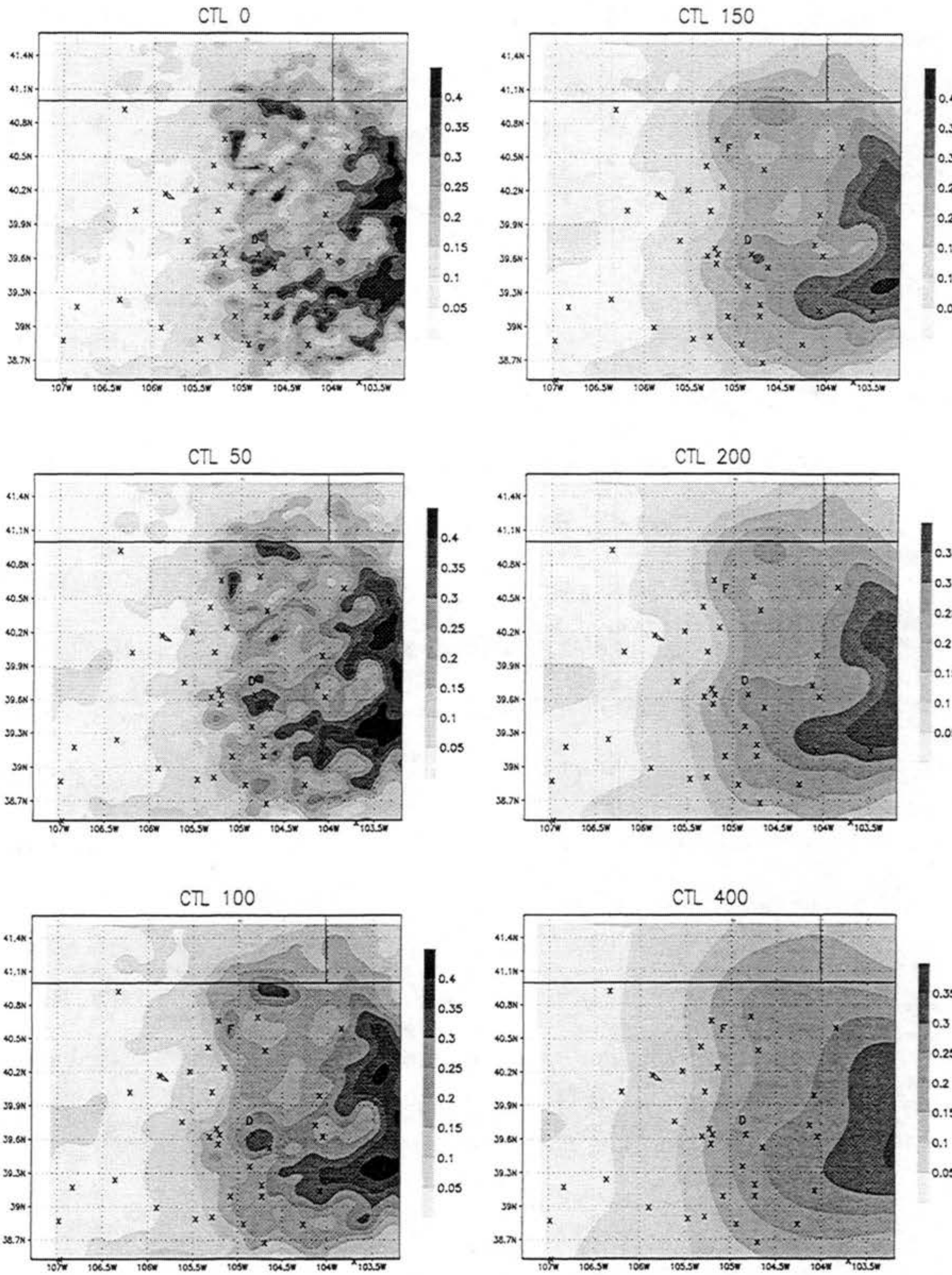


**Figure 4.8** Objective analysis of full 5km gridded, radar-derived API estimated volumetric soil moisture content. Shading interval is 0.03 $m^3/m^3$. The wavelength retained at a response of 0.9 labels each plot. CTL 0 is the unaltered estimate on the 5km grid. Sampling stations used in deriving Figure 4.9 are denoted by an "x". Denver and Fort Collins are denoted by an "F" and "D" respectively. Shade scaling is identical between plots.

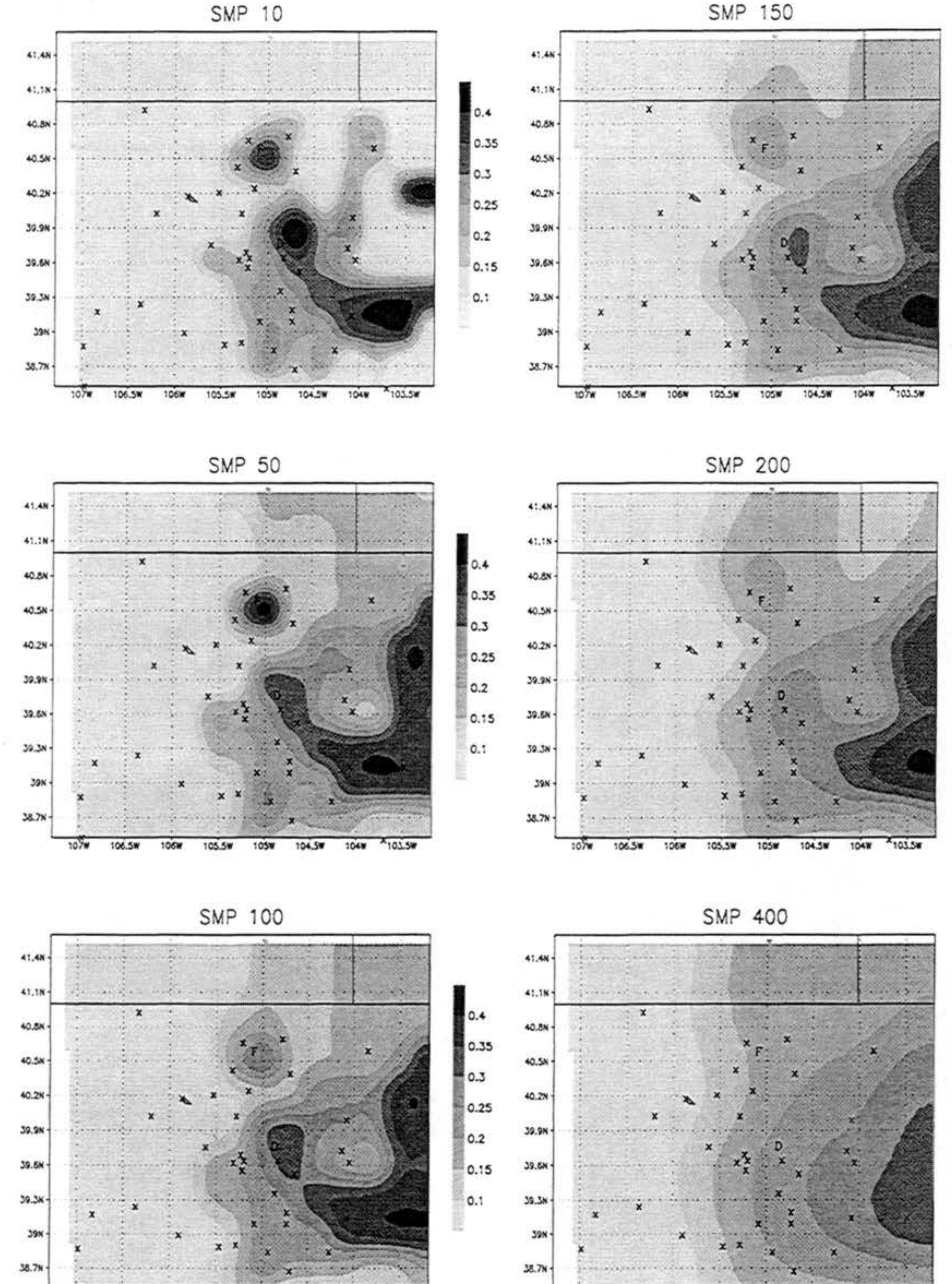


**Figure 4.9** Objective analysis of volumetric soil moisture content from sampled, radar derived API estimate. The wavelength retained with a response of 0.9 labels each plot. Contour interval is 0.03 $m^3/m^3$. Sampling locations are denoted by an "x". Fort Collins (CSU campus) and Denver (Denver International Airport) are denoted by "F" and "D" respectively. Shade scaling is identical between plots.

| SMP→ / CTL↓ | 10 | 20 | 50 | 75 | 100 | 125 | 150 | 175 | 200 | 250 | 300 | 400 | 500 |
|---|---|---|---|---|---|---|---|---|---|---|---|---|---|
| **0** | .5972 | .8077 | .8251 | .8389 | .8470 | .8530 | .8557 | .8556 | .8541 | .8519 | .8490 | .8392 | .8255 |
| **10** | .5972 | .8077 | .8251 | .8389 | .8470 | .8530 | .8557 | .8556 | .8541 | .8519 | .8490 | .8392 | .8255 |
| **20** | .5976 | .8083 | .8257 | .8396 | .8477 | .8537 | .8564 | .8563 | .8548 | .8526 | .8497 | .8398 | .8262 |
| **50** | .6222 | .8420 | .8619 | .8765 | .8850 | .8914 | .8943 | .8942 | .8928 | .8907 | .8878 | .8778 | .8637 |
| **75** | .6315 | .8558 | .8775 | .8925 | .9013 | .9079 | .9110 | .9110 | .9098 | .9079 | .9052 | .8954 | .8813 |
| **100** | .6366 | .8644 | .8878 | .9032 | .9123 | .9192 | .9225 | .9227 | .9216 | .9201 | .9177 | .9084 | .8943 |
| **125** | .6387 | .8695 | .8946 | .9104 | .9198 | .9269 | .9304 | .9308 | .9300 | .9290 | .9271 | .9183 | .9045 |
| **150** | .6387 | .8721 | .8991 | .9152 | .9248 | .9322 | .9359 | .9367 | .9362 | .9357 | .9343 | .9263 | .9129 |
| **175** | .6372 | .8730 | .9019 | .9182 | .9281 | .9357 | .9398 | .9408 | .9406 | .9409 | .9401 | .9330 | .9200 |
| **200** | .6347 | .8927 | .9036 | .9201 | .9302 | .9380 | .9424 | .9438 | .9440 | .9449 | .9449 | .9388 | .9264 |
| **250** | .6275 | .8694 | .9047 | .9212 | .9319 | .9401 | .9450 | .9471 | .9481 | .9507 | .9524 | .9488 | .9377 |
| **300** | .6182 | .8639 | .9037 | .9202 | .9312 | .9398 | .9452 | .9480 | .9498 | .9543 | .9578 | .9570 | .9476 |
| **400** | .5972 | .8492 | .8983 | .9145 | .9260 | .9351 | .9413 | .9452 | .9485 | .9567 | .9640 | .9692 | .9635 |
| **500** | .5768 | .8322 | .8904 | .9063 | .9182 | .9276 | .9342 | .9390 | .9435 | .9548 | .9655 | .9764 | .9746 |

**Table 4.2** Linear correlation coefficients. Light shading denotes boxes corresponding to equal wavelength. Dark shading denotes SMP wavelength of maximum correlation with each CTL wavelength. A circle shows the general region where the coevolution of CTL wavelength and SMP wavelength of maximum correlation ceases.

A linear correlation analysis was done between these fields, yielding correlation coefficients for each pair of CTL and SMP fields. These results are shown in Table 4.2 above. Firstly, it is apparent that as the wavelengths of both the SMP and CTL fields are increased, the correlation coefficients increase, with the largest coefficients occurring near the lower right corner of the table. This behavior should be expected since both the SMP and CTL fields reduce to nearly the same field, that is the domain average, as the wavelength increases to infinity. In addition, one can clearly discern a dominant one-domain-width wavelength, zonal distribution of soil moisture in CTL 0 that the sampling network adequately samples. What is of interest in determining the proper wavelength for the objective analysis is the set of SMP wavelengths that correlate best with each individual CTL wavelength. These boxes are shaded with dark gray. These boxes indicate that within the range 175-500 km, the SMP wavelength of maximum correlation evolves nearly in tandem with the CTL wavelength. This behavior is exactly what one should expect if the SMP field is producing an approximate smoothing of the true underlying field at a wavelength consistent with that specified. This can be more clearly understood if one considers what a true or "perfect" Barnes objective analysis would produce. As noted earlier, the discrete version of the Barnes scheme, which is also the one used in practice, is only an estimate of the continuous version, the latter being a smoothing operation with smoothing properties specified by the wavelength and response. If this discrete estimate does not provide an acceptable estimate, due to discretization error and undersampling with respect to the averaging operation, then there is the danger of the resulting field being *neither* an accurate representation of the true field, *nor* that of any area-average. Hence, a perfect Barnes objective analysis would always provide a smoothed version of the underlying field on length scales that are in accordance with the user-specified parameters (wavelength and response). This is precisely what is represented by the CTL field. Therefore, if one considers then how a perfect objective analysis correlates with the CTL fields, it should be clear that the results would be similar to auto-correlating the CTL set. This would produce wavelengths of maximum correlation along the diagonal of the table.

The qualitative observation is that when an objective analysis is providing an area-average of the underlying field, the wavelength of maximum correlation should change nearly in unison with the true area-averaged field when the method of averaging is comparable. What is clear from the behavior of the SMP wavelength of maximum correlation is that this trend exists at wavelengths longer than 175 km but begins to decay at approximately 150-175 km wavelength. This indicates that at the short wavelength end of this range, the objective analysis becomes increasingly ineffective at providing an area-average consistent with the user specified parameters and is inadequate at even shorter wavelengths.

One ramification of this behavior can be seen in comparing the evolution, with increasing wavelength, of the soil moisture perturbation located near Fort Collins. CTL 0 shows a high magnitude soil moisture perturbation with east-west dimensions of ~10 km and north south dimensions of ~30 km. As the wavelength in Figure 4.8 increases, this perturbation remains nearly constant in spatial extent while the magnitude of the perturbation decays. Examination of the SMP 100 field in Figure 4.9 shows that this perturbation has been sampled and somewhat decayed but is depicted as a ~100-km diameter perturbation. At smaller SMP wavelengths, this problem becomes even more apparent. In essence, the small-scale variability in CTL 0 has been under-sampled and projected onto a length scale imposed, in part, by the mean station separation distance. At longer wavelengths the length-scales and magnitudes of moisture perturbations are in better agreement with CTL fields smoothed at the same wavelength and the Barnes scheme is providing an estimate in accordance with its design.

The error in assessing the length-scale of high amplitude perturbations should not be taken lightly. As noted in Section 2.2.3, numerical results have suggested that stronger NCMC's with subsequent initiation of deep convection, may occur for 100-km soil-moisture perturbations compared to ~20-km perturbations. Hence the projection of under-sampled extrema onto the 100-km length scale — that which is imposed by the station separation distance — is not desirable, and yet is certain to occur when the station samples are sampling a field with finer structure than that of the station network and the Barnes wavelength is insufficiently large. The objective is not to eliminate 100-km scale soil-moisture perturbations from the analysis, but rather to diminish the probability of aliasing much smaller scale, large amplitude perturbations, which are abundant in CTL 0, to this scale. Despite the fact that the CTL 0 soil-moisture field is hypothetical, it seems plausible that the spatial complexity in this field is typical of soil moisture perturbations produced by convective precipitation during the summer months in Colorado. Using the results of this sampling experiment as guidance, a wavelength of 200 km was chosen for the objective analysis of *gauge* data using the method described earlier in this section. The soil moisture analysis used for initializing Simulation B is shown in Figure 4.10 below. As can be seen from this figure, there are still 100-km length-scale perturbations, one of which is centered to the northwest of Fort Collins. Again, the objective was not to eliminate perturbations of this scale, but to retain a magnitude that more likely represents the areal average at this length scale. Comparison with Figure 4.7 shows that a 90-km wavelength applied to this same station data yields a soil moisture perturbation of similar length scale to that in Figure 4.10 but with a much higher magnitude. This magnitude on this length scale is hardly justified by the one station (FCL 9 NW) which edge-sampled the analyzed perturbation.

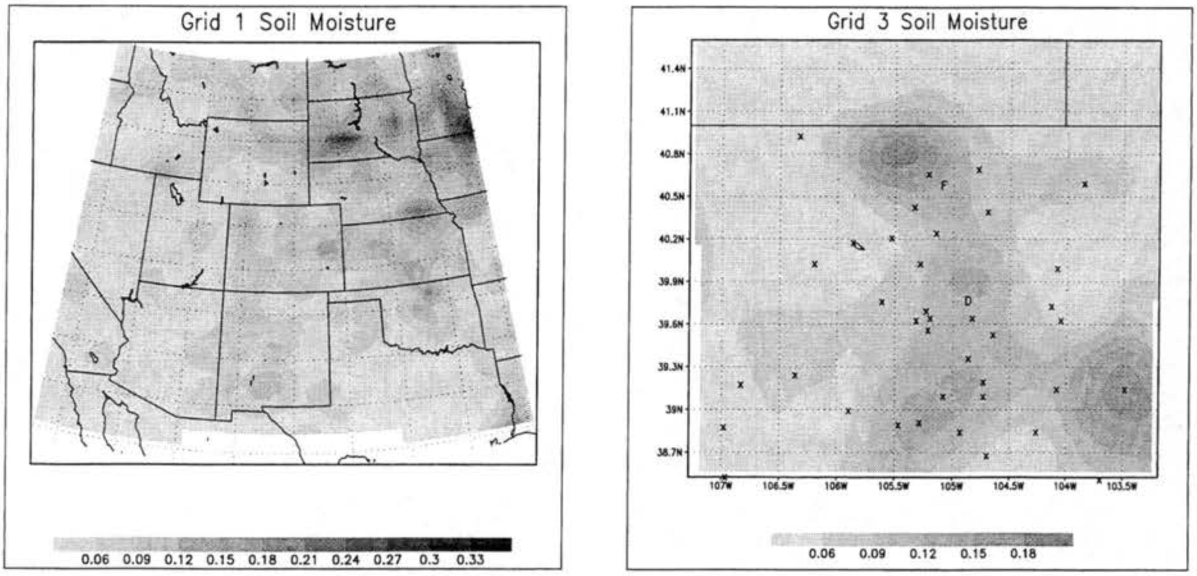


**Figure 4.10** Initial volumetric soil-moisture distribution on grid 1 (left) and grid 3 (right) for simulation B, shown with gauge locations. Contour interval is 0.03 $m^3/m^3$.

Comparison of Figures 4.10 and 4.5 shows that the ETA-derived soil moisture values are significantly higher than that of the API method. On Grid 3, the average volumetric soil moisture content in the top-level of soil is 0.23 $m^3/m^3$ (54% saturation) in Simulation A, compared to 0.075 $m^3/m^3$ (18% saturation) in Simulation B. Consequently, many of the differences in simulation evolution examined in later chapters will largely be a result of the large discrepancy in overall initial soil moisture magnitude as opposed to spatial distribution.

# 5

# Synoptic-scale Forecasts

## 5.1 Introduction

In this chapter, the Grid 1 forecast fields are presented. Examination of these fields serves two purposes: to familiarize the reader with the state of the simulated synoptic pattern at a standard synoptic observation time and to identify differences between the forecast and observations, as well as those between simulations. The primary focus will be on the 00Z July 29 (12-hour) forecasts. Additional details of the synoptic-scale evolution are also found in Chapter 5 where the synoptic fields at non-standard observation times are deemed relevant to the nested grid results. Because much of the model output in this chapter is compared with standard National Weather Service analyses, the choice of units in this chapter will be those used in the analyses: knots for windspeed, Celsius for upper-air temperature and dewpoint temperature, and Fahrenheit for surface temperature and dewpoint. MKS units will be used exclusively in later chapters.

## 5.2 Simulation A

### 5.2.1 *Free-atmosphere*

Figures 5.1 and 5.2 below show the NCEP 500 mb analysis along with the 00Z July 29 forecast produced in Simulation A. The NCEP analysis shows both station rawinsonde measurements as well as the contoured height and temperature analysis of the 48-km ETA operational model. As in the NCEP analysis, Simulation A positions the center of the monsoon ridge over the Oklahoma-Texas border area. The forecast geopotential heights over Texas, southern New Mexico and southern Arizona are 2-3 dm higher than observed. This is likely due, in part, to the input data-files used for boundary nudging, as a 1-2 dm excess is also present in the nudging files over these same areas. However, the simulated 500 mb heights in this area exhibit an additional 1-2 dm increase above those of the nudging data. Further north, over Utah, Wyoming and Colorado, the forecast heights are generally within 1 dm of the observations.

Throughout the majority of the domain, the forecast winds are in good agreement with those of the analysis. The most notable exception is at Rawlins, Wyoming where the analysis shows a 15-kt easterly wind while the forecast maintains a westerly component in this area. Over Colorado, the forecast winds closely approximate those of the rawinsonde observations. The 588-dm contour in both the 48-km ETA analysis and in the Simulation A forecast indicate a shortwave disturbance extending from southwestern Wyoming, southeastward to the Continental Divide. This same feature can be seen with a much larger amplitude in the 700-mb, Simulation A forecast (Figure 5.3). Over Colorado, the forecast 500 mb dewpoint depressions are 1-5°C greater than the rawinsonde values, indicating slightly drier conditions than observed. However, the

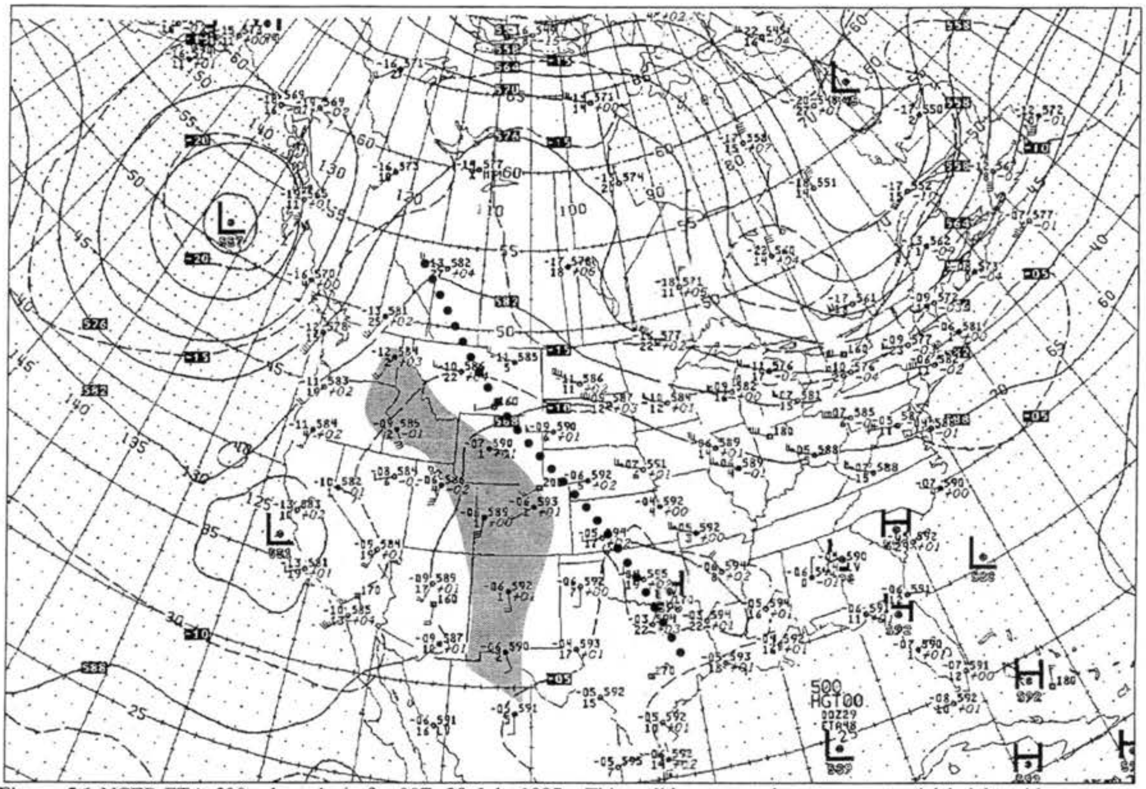

**Figure 5.1** NCEP ETA 500 mb analysis for 00Z, 29 July 1997. Thin solid contours denote geopotential height with a contour interval of 6 dm. Thin dashed contours denote temperature with a contour interval of 5°C. Thick dotted annotation line shows location of ridge axis. Shaded annotation denotes approximate area of dewpoint depression ≤ 2°C. (Identical to Figure 3.3).

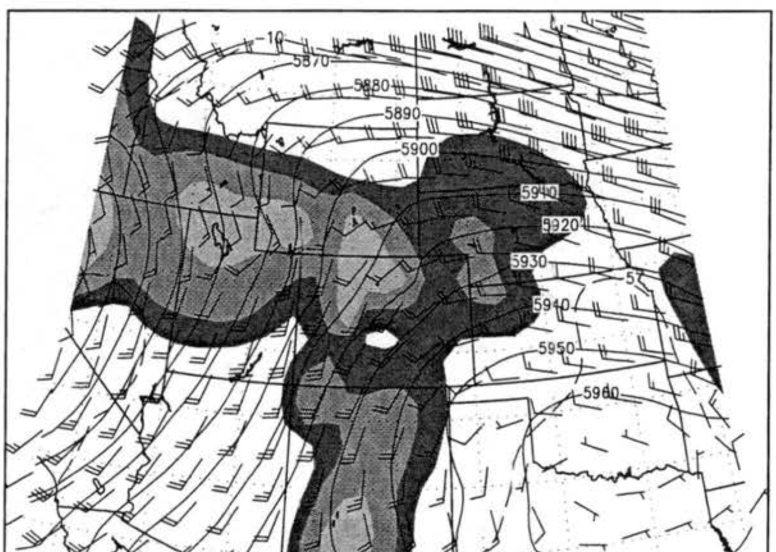


**Figure 5.2** 12-hr, 00Z July 29, Simulation A 500 mb forecast. Solid contours: geopotential height, 1-dm interval. Dashed contours: temperature, 5°C interval. Wind barbs: half-barb=5 kt, full-barb=10 kt, pennant=50 kt. Shading denotes dewpoint depression (d.d.): Light=(d.d.≤2°C), Medium=(2°C≤d.d.≤4°C), Dark=(4°C≤d.d.≤6°C).

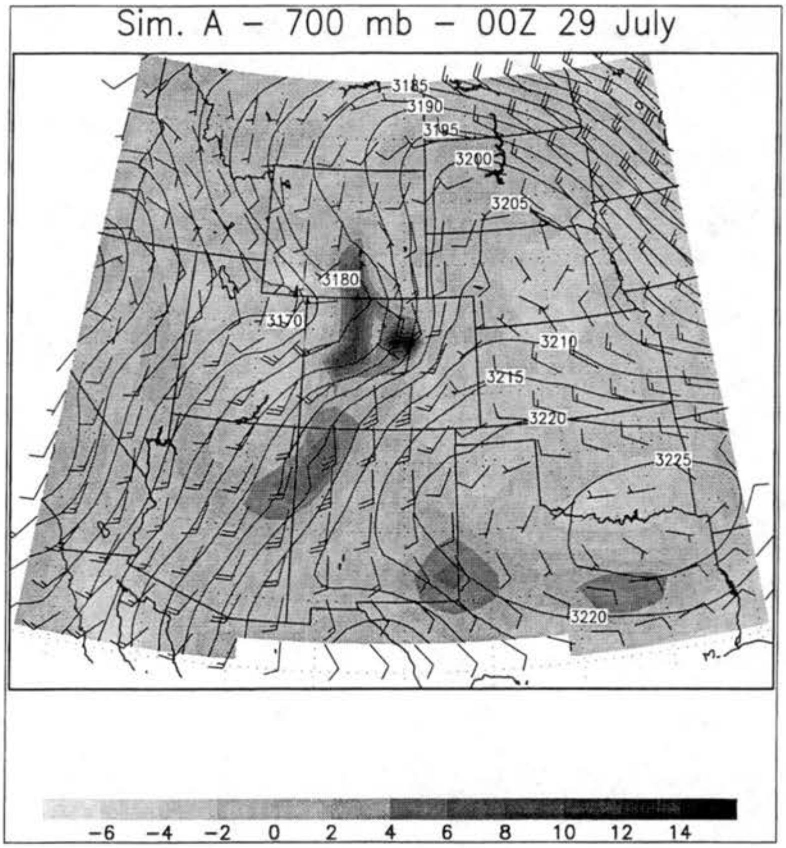


**Figure 5.3** 12-hr, 00Z Simulation A, 700 mb forecast. Solid contours: geopotential height, 5 meter interval. Barb convention same as figure 5.2. Vertical velocity shaded at 2 cm/sec interval.

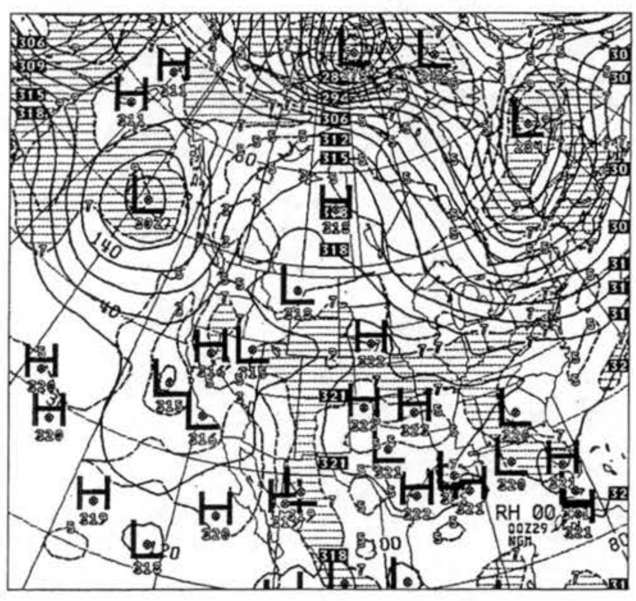


**Figure 5.4** 00Z July 29, 700 mb NGM analysis. Geopotential height (solid contour, 3 dm interval). Relative humidity (dashed contour, 20% interval starting at 10%). Shading denotes areas with relative humidity greater than 70%.

general pattern of dewpoint depressions match those in Figure 5.1 quite well, with the smallest dewpoint depressions occurring in a north-south band from New Mexico to northern Colorado, and in advance of the shortwave in Wyoming and Idaho. The temperature forecast at 500 mb also agrees well with the 48-km ETA analysis and rawinsonde observations.

At 700 mb (Figure 5.3), Simulation A depicts two high pressure centers. One is located almost directly beneath the 500 mb high over the Texas-Oklahoma border while a secondary center appears over central Nebraska. This is in accordance with the NGM 00Z 29 July analysis (Figure 5.4 above). In addition, the NGM analysis depicts a northward translating shortwave trough, the axis of which is centered on the Colorado-Wyoming border, extending into eastern Colorado. This is also present in the 12 hour (00Z), forecast of simulation A with the shortwave axis oriented in a northwest-southeast direction just south of the Colorado-Wyoming border. The cyclonic curvature across the short-wave axis results in a weak easterly (upslope) component in northern Colorado along the Front Range and southern Wyoming, while southerly and south-southwesterly winds are found to the south of the shortwave axis. Meso-$\alpha$- and meso-$\beta$-scale areas of positive vertical motion exist within the shortwave with maxima of 10-14 cm/s. Much of this vertical motion is associated with convective motions on grids 2 and 3.

### 5.2.2 *Surface forecast*

Figures 5.5 and 5.6 show the surface analysis and the 12-hour (00Z) Simulation A forecast temperature, dewpoint, winds and reduced mean-sea-level pressure. In contrast to the free-atmosphere forecasts, considerable error is present in the Grid 1 surface temperature and dewpoint forecast. East of the Continental Divide, the forecast

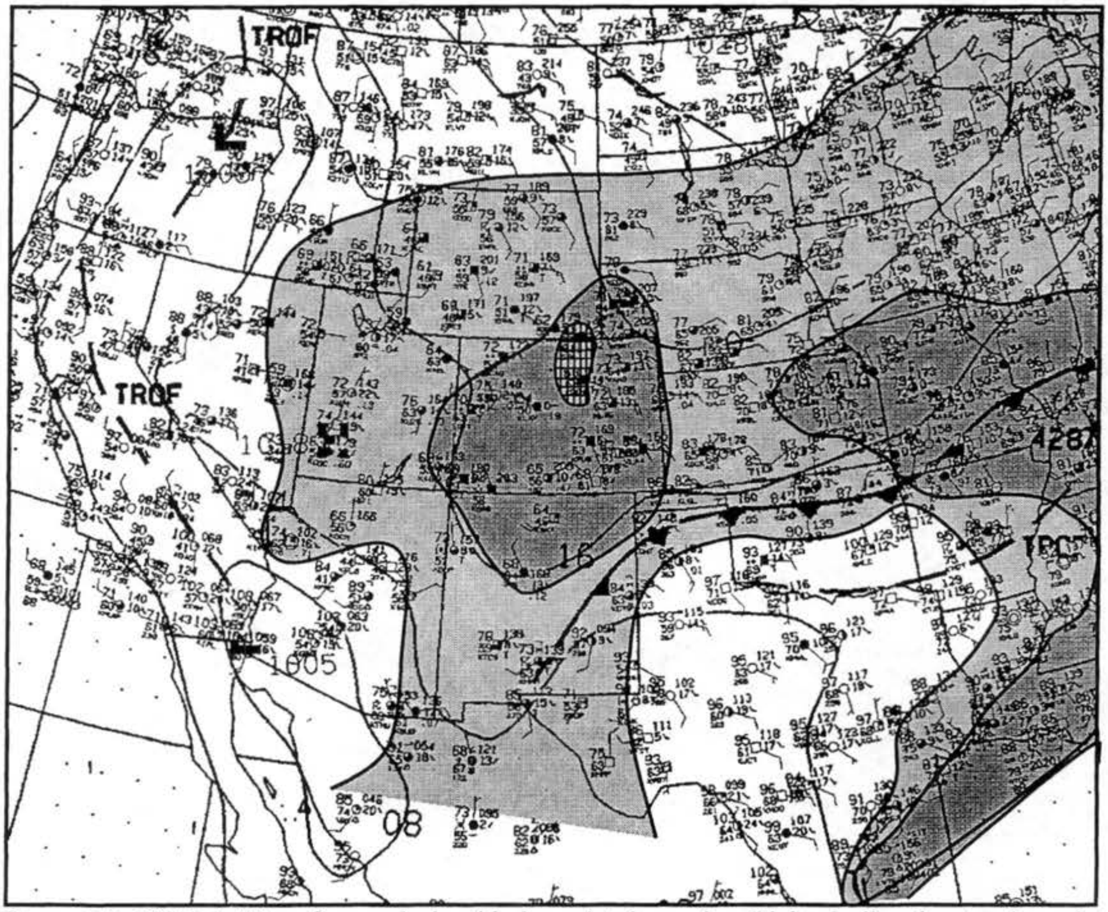


**Figure 5.5** 00Z July 29 surface analysis with dewpoint depression. Light shading denotes dewpoint depression < 20°F, medium shading < 10°F and crosshatch pattern < 5°F.

temperature is generally too cold with a typical error between -5°F and -15 °F. The forecast temperature errors are most significant in the central and southern plains. Forecast dewpoint temperatures are systematically higher than observations with errors between +5°F and +15°F. The bias toward cooler temperatures and more moist conditions results in significant forecast error in surface dewpoint depression. Comparison of Figures 5.5 and 5.7 shows that the dewpoint depression forecast deviates from observations by -5°F to -30°F over the southern and central plains. While the analysis shows dewpoint depressions less than or equal to 5°F occurring only along the Front Range, the simulation 00Z forecast shows an area of dewpoint depressions less than 5°F which covers approximately half of the domain.

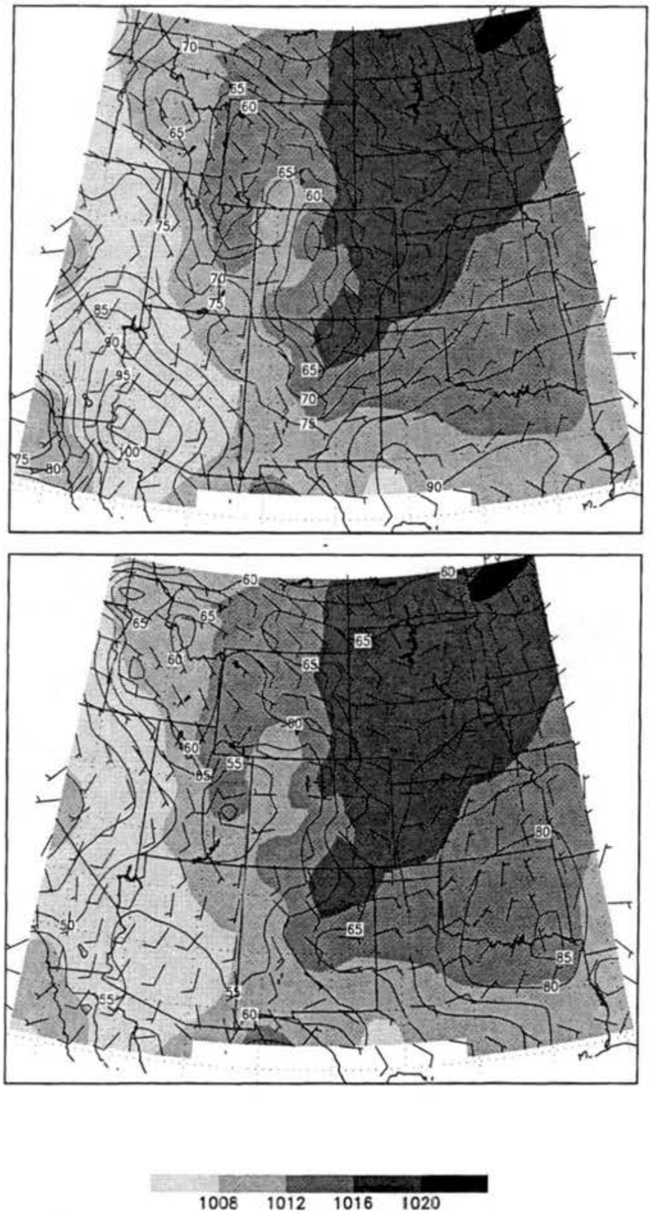


**Figure 5.6** 12-hr 00Z, Simulation A surface forecast. Top panel depicts reduced mean-sea-level pressure shaded at 4 mb intervals. Solid contours denote temperature at 5°F intervals. Wind barb convention is the same as in Figure 5.2. Lower panel is the same as top panel, except solid contours denote dewpoint at 5°F intervals.

The fact that this error occurs in the boundary layer while the free-atmosphere forecasts remain very reasonable, strongly suggests that the cause lies in the sensible and latent fluxes produced by the surface parameterization at the lower boundary. A typical

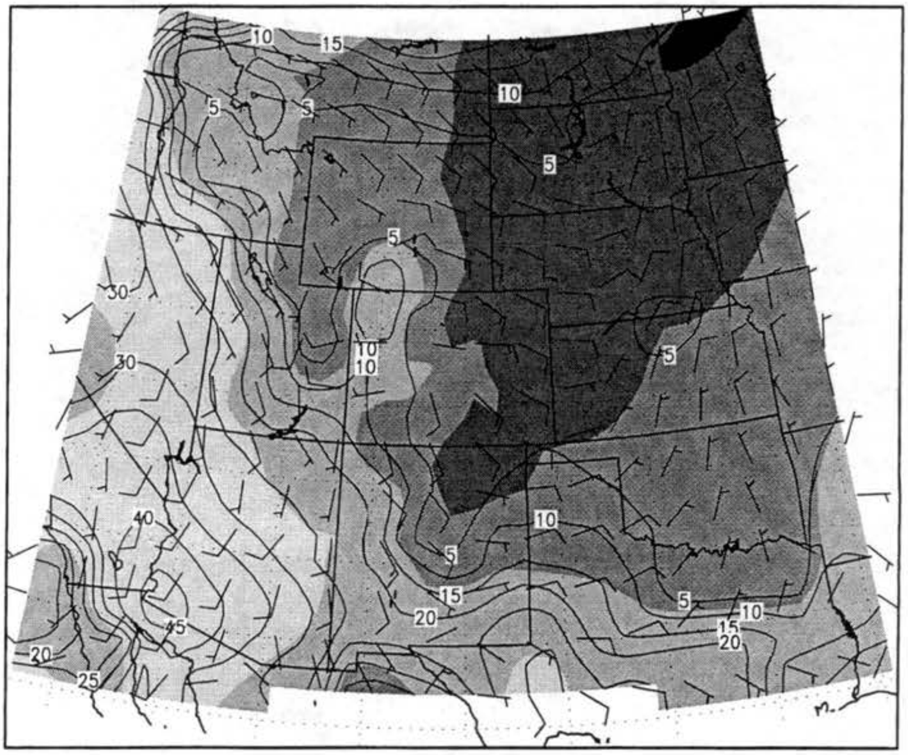


**Figure 5.7** Same as figure 5.6, except solid contours denote dewpoint depression at 5°F intervals.

example of the situation in the southern and central plains is given in Figure 5.8. The top panel in this figure shows the observed temperature evolution between 12Z July 28 and 00Z July 29 at KTUL (Tulsa International Airport). The lower panel shows the simulated temperature and dewpoint evolution at the grid point closest to KTUL. Observations indicate that the surface temperature climbed 18°F between 12Z and 22Z while the dewpoint temperature remained between 72°F and 75°F. The simulated surface evolution, however shows a nearly steady temperature throughout the entire period while the dewpoint increases over 10°F between 12Z and 20Z, bringing the lower atmosphere to near saturation. Incident radiant energy at the surface (Figure 5.9) shows that nearly clear sky conditions existed between 13Z and 18Z and between 21Z and 00Z. The lowest incident radiation flux was roughly 920 W/m$^2$ at 20Z. Hence, lack of incident radiation is

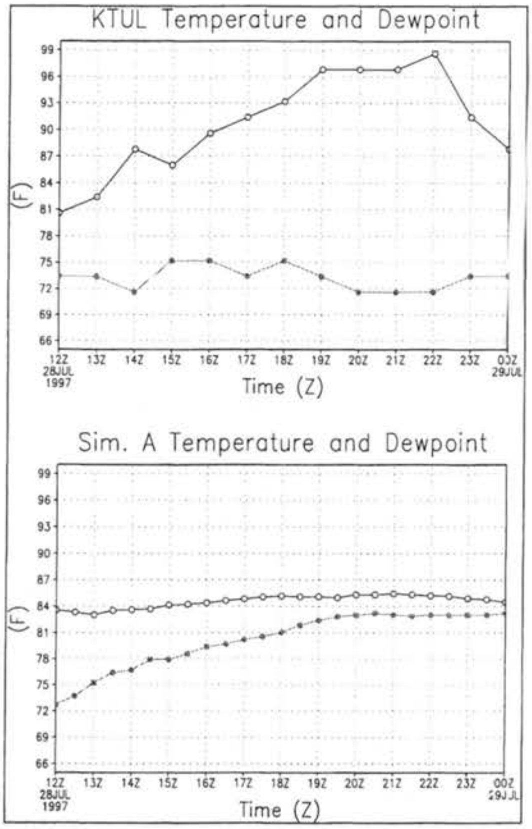


**Figure 5.8** Top panel: observed temperature (open circles) and dewpoint (solid circles) at Tulsa, Oklahoma (KTUL) for the time period 12Z-23Z 28 July. Bottom panel: simulated temperature at and dewpoint for closest Grid-1 gridpoint.

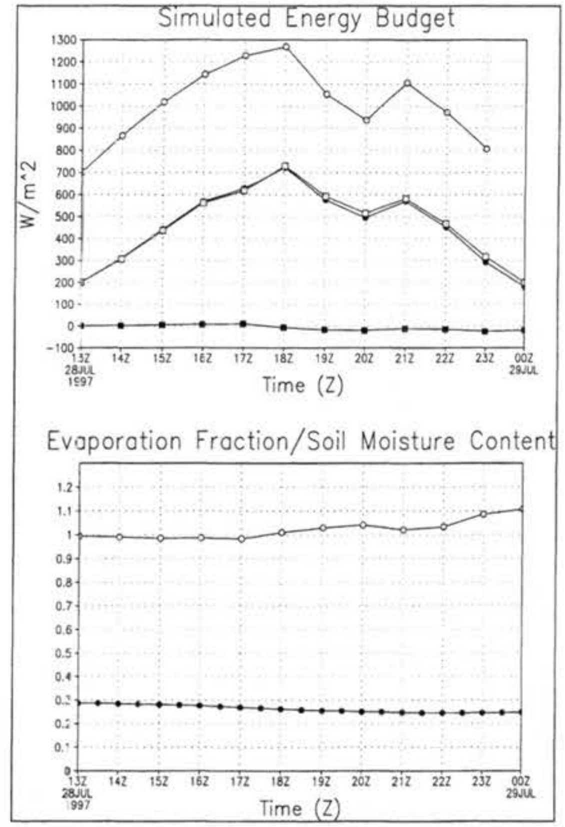


**Figure 5.9** Top panel: Simulated energy budget for Tulsa gridpoint. Incident radiation (open circles), available energy flux (solid circles), latent heat flux (open squares), sensible heat flux (solid squares). Bottom panel: Evaporation fraction (open circles), volumetric soil moisture (closed circles).

not a possible explanation for the nearly steady simulated surface temperature. Rather, Figure 5.9 shows that the problem lies in the partitioning of the available energy flux between sensible and latent heat (vapor) flux. Available energy (AE) is simply the sum of latent and sensible heat flux. The evaporation fraction (EF), is defined as:

$EF = LH/(SH+LH) = LH/AE$, where LH is the latent heat flux and SH is the sensible heat flux.

The lower panel in Figure 5.9 shows that the evaporation fraction remains above 0.98 throughout the entire period 12Z-00Z. Beyond 18Z, the latent heat flux exceeds the available energy, resulting in a negative sensible heat flux. This occurs when surface evaporation rate becomes large enough to cool the soil and vegetation to a temperature below that of the overlying atmosphere and sensible heat is transferred to the surface from the overlying atmosphere. In this situation, all of the incoming radiation is used for vaporizing liquid water from the soil and vegetation with little or no sensible heating of the lower atmosphere.

Betts and Ball (1995) examined the surface diurnal energy budget over the First International Land Surface Climatology Project (ISCLP) Field Experiment Site (FIFE) near Manhattan, Kansas during 1987. Betts and Ball categorized the observation days between May 26 and September 30 by the top 10-cm-layer soil moisture content. Figure 5.10 below shows their calculated average evaporation fraction as a function of time of day and volumetric soil-moisture content category. In order to establish a crude correspondence between their data and the simulation, it should be noted that sandy-clay-loam, the soil type used in all simulations appearing in this thesis, is characterized by a saturation volumetric moisture content of 42% (0.42 $m^3/m^3$). The soil-moisture value given to each curve in Figure 5.10 is the average soil moisture content associated with each category. The last category, 0.256 $m^3/m^3$, corresponds to 61% saturation for sandy-clay-loam, and the category definition was volumetric soil moisture content greater than 0.23 $m^3/m^3$ or 55% saturation for sandy-clay-loam. The curves in this figure indicate that evaporation fraction is typically below 0.8 during the daytime, even for the most moist soil conditions considered. In addition, Betts and Ball note that above volumetric moisture concentrations of 0.22 $m^3/m^3$, the evaporation fraction becomes less sensitive to soil moisture content. While vegetation parameters and soil properties in that field study are not exactly those imposed in the model surface parameterization, the simulated evaporation fraction is dubious.

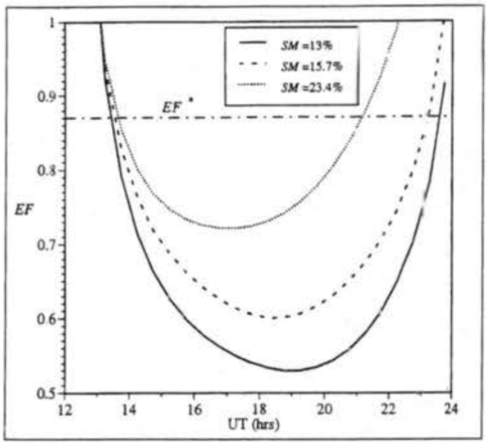


**Figure 5.10** Average evaporation fraction for three soil moisture categories. Percentages corresponding to each curve are the average volumetric soil moisture content for each category. Curves are derived from data collected in FIFE during the summer of 1987. Figure from Betts and Ball (1995).

For comparison, temperature and dewpoint observations and forecasts are shown in Figures 5.11 and 5.12 for KFLG (Pulliam Airport, Flagstaff, Arizona). Here the forecast dewpoint depression is in much better agreement with observations than in the KTUL case. Both the observations and simulation exhibit a daytime increase in temperature and a daytime decrease in dewpoint temperature, although the decrease in dewpoint is somewhat underestimated in the simulation. An examination of the surface energy budget shows that the evaporation fraction is significantly smaller than at KTUL, with values ranging from 0.4 to 0.65 during the morning and afternoon, and the sensible heat flux becomes as large as 350 W/m$^2$ at 20Z. The incident radiation at Flagstaff is seen to be comparable to that at Tulsa. The most significant difference between these two simulated sites is the top soil-layer volumetric moisture content. While Tulsa soil moisture content varies from 0.30 m$^3$/m$^3$ (71% saturation) to 0.25 m$^3$/m$^3$ (59%

saturation), Flagstaff is considerably drier with top soil-layer moisture varying from 0.18 $m^3/m^3$ (43% saturation) to 0.10 $m^3/m^3$ (24% saturation). The examples provided from Flagstaff and Tulsa are typical of the dewpoint-depression/evaporation-fraction relationship throughout the Grid 1 domain, with exceptions to be noted shortly.

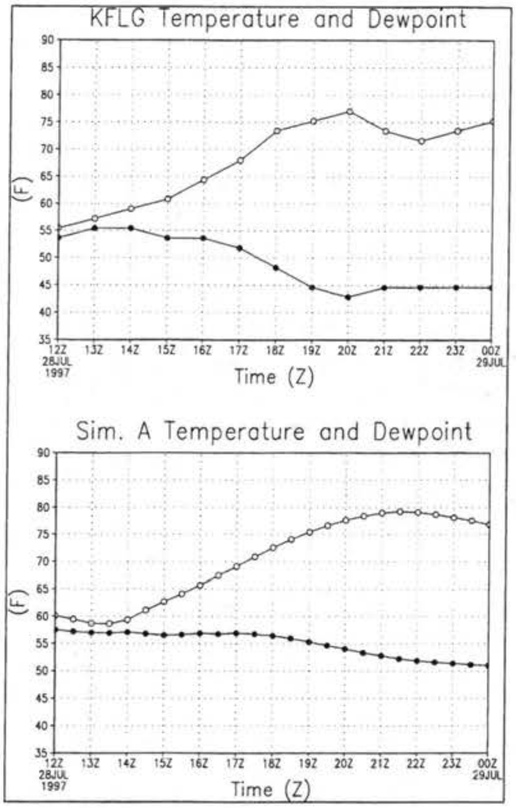


**Figure 5.11** Same as Figure 5.8, except for Flagstaff, Arizona (KFLG).

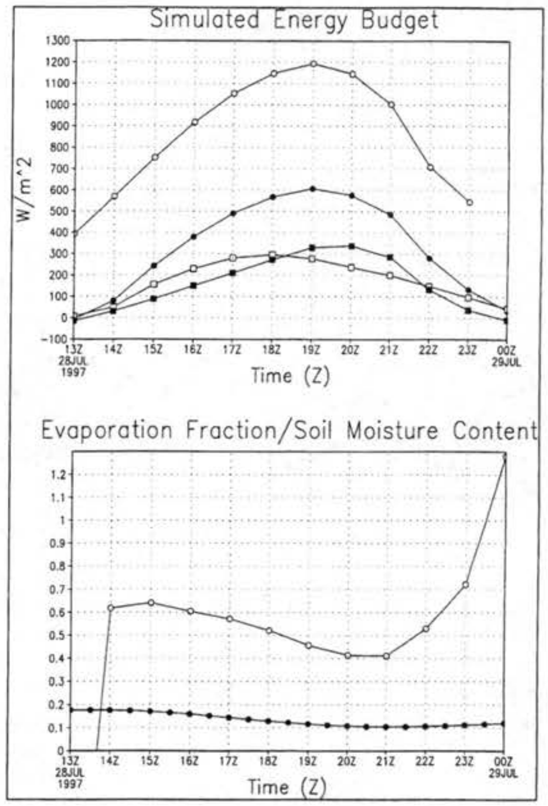


**Figure 5.12** Same as Figure 5.9 but for Flagstaff gridpoint.

These examples suggest that the dewpoint depression forecast error is likely due to an overestimate of evaporation fraction in regions of high ($\gtrsim$50% saturation) soil moisture content. This conclusion is finalized by the masks shown in Figure 5.13. The black area in the first mask consists of those grid points that satisfy the following conditions: a.) the grid point is not within 320 km of the Grid 1 boundary, and b.) the forecasted 00Z dewpoint depression is less than 5°F. The first condition is imposed because this mask is going to be compared to model simulated surface fluxes. Near the

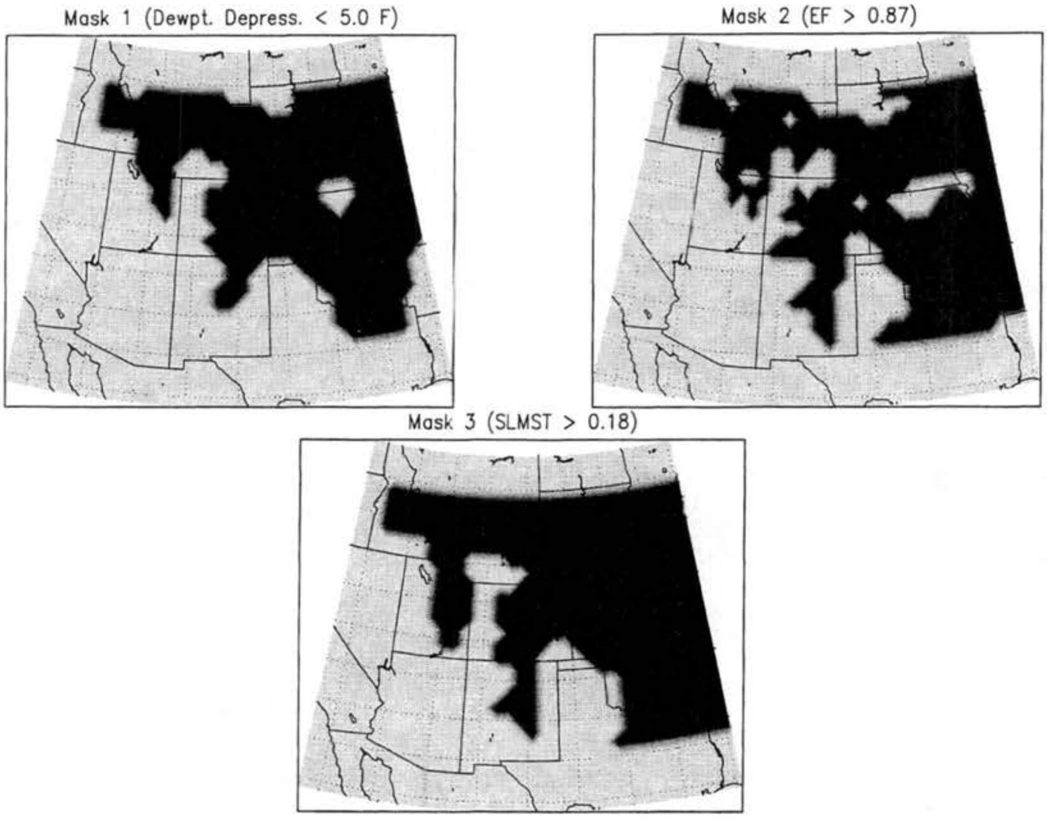


**Figure 5.13** Masked fields corresponding to 00Z dewpoint depression < 5°F (top left), 18Z-23Z average evaporation fraction (EF) > 0.87 (top right), and 18Z-23Z average top-level volumetric soil moisture content > 0.18.

grid boundary, the temperature and dewpoint evolve in a more or less independent fashion from the surface forcing, due to the Newtonian nudging tendencies, and hence these grid points are excluded from consideration. The second mask denotes grid points that satisfy "a" above, and the condition that the average 18Z-23Z evaporation-fraction is greater than 0.87. The seemingly arbitrary cutoff of 0.87 is, in fact, not arbitrary. Betts and Ball (1995) presented mixed-layer model equations for the local time rate of change of saturation pressure, or lifting condensation level (LCL) at the surface. Using approximate values applicable to the FIFE data for inversion-base Bowen ratio and the entrainment closure parameter they estimated an evaporation-fraction of 0.87 as the critical value for maintaining the saturation pressure against daytime, boundary layer dry air entrainment and temperature increase. To a first approximation, a constant saturation pressure implies a nearly constant dewpoint depression for surface parcels. The 12Z July 28 analysis (not shown) indicates that dewpoint depressions over the Great Plains were generally between 5°F and 10°F at the time of model initialization. Hence, the 00Z forecasted depressions of less than 5°F equate to maintenance or reduction in the initial, or 12Z, dewpoint depressions.

Despite the fact that the assumed parameters for the FIFE site are not guaranteed to hold over the entire simulation domain, the critical evaporation-fraction of 0.87 was used as a guide. This guide is served quite well as the similarity between Masks 1 and 2 is unmistakable. The agreement is not perfect but the similarity clearly identifies evaporation fraction as the primary contributor to the small dewpoint depressions. The Bowen ratio (defined as SH/LH) that is implied by an evaporation fraction of 0.87, is 0.15. Betts and Ball note that, "Over the FIFE grassland, Bowen ratios are *never* this low unless forced by strong dry advection, so that $p^*$ generally falls (LCL rises)." There is no evidence of strong, dry advection in the simulation, the observations over the Tulsa grid-point, or over the area of forecasted dewpoint depression less than 5°F.

The third mask denotes the grid points where "a" above is satisfied and the average 18Z-23Z, top-level volumetric soil moisture is above 0.18 $m^3/m^3$ (43% saturation). This value was chosen based on an inspection of the average soil moisture field between 18Z and 23Z. This mask corresponds well with most of Mask 2 with the exceptions lying on the central portion of the Nebraska/Kansas border and northwestern

South Dakota. Hence, the majority of the region corresponding to dewpoint depressions less than 5°F, is explained by the evaporation fraction as seen in Mask 2, which in turn is largely controlled by the top-level soil moisture as seen in Mask 3.

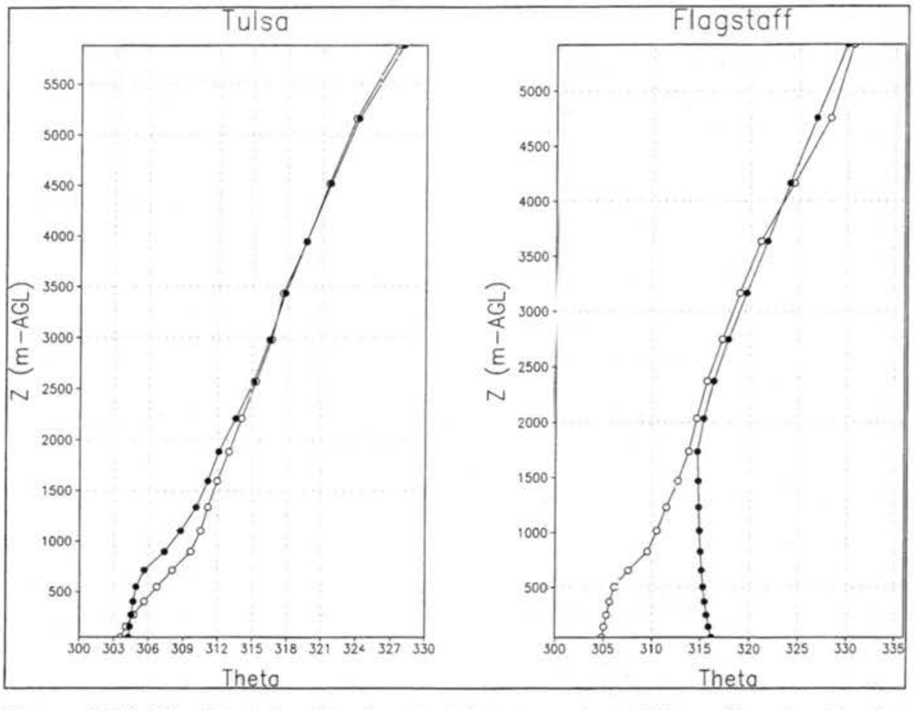


**Figure 5.14** Simulated low-level potential temperature (K) profile at gridpoints closest to Tulsa (left) and Flagstaff (right). Open circles correspond to 12Z July 28; solid circles correspond to 22Z July 29. Height on vertical axis is expressed in meters above ground level.

Excessively small sensible heat fluxes will tend to restrict the growth of the convective boundary layer. The top and lower panels in Figure 5.14 show the 12Z and 21Z potential temperature profiles at the Grid-1 grid points closest to Tulsa and Flagstaff respectively. At 21Z, the Flagstaff grid point has an unstable boundary layer extending to 1.7 km AGL. In contrast, the simulated Tulsa boundary layer is stable and shallow despite enduring eight hours of clear sky conditions. There is a daytime reduction in stability above 200 m AGL between 12Z and 21Z at Tulsa that is, in large part, due to cooling between 200 m AGL and 2.7 km AGL. The reduction in boundary layer growth may also contribute to the dewpoint depression error by diminishing dry-air entrainment into the boundary layer. Additionally with boundary layer growth restricted, vapor flux from the surface is confined to a smaller volume leading to a stronger rise in surface dewpoint temperature for a given vapor flux at the surface. These two effects likely exacerbate the forecast dewpoint depression error. Given that the top-level soil moisture cutoff value (0.18 $m^3/m^3$) is smaller than two of the soil moisture categories considered in Betts and Ball (1995), and yet the simulations produce evaporation fractions that far exceed those in the 1995 study, it is impossible to claim that the soil moisture initialization in Simulation A is the source of error. Regardless of the soil moisture content, the simulated evaporation fraction appears to be excessive, and the surface parameterization must therefore be questioned.

It is important to remember that a forecast dewpoint depression less than 5°F does not imply error in the dewpoint depression forecast unless observations show that conditions deviated significantly from this prediction. In eastern Colorado, the observed dewpoint depressions were less than 10°F and were less than 5°F along the Front Range. The forecast error in these locations is much less than in the central and southern plains. The 00Z surface analysis (Figure 5.5) shows that many of the stations within the analyzed 10°F dewpoint-depression contour experienced broken clouds to overcast conditions. Cloud coverage is, of course, another potential mechanism of reducing sensible heat flux and hence boundary layer growth and rising surface temperature, through a reduction in incident radiation.

### 5.2.3 *Summary*

In this section, the 12-hr upper-air and surface forecasts were presented. By far, the greatest errors in the synoptic fields were associated with the boundary layer temperature and moisture fields, with Simulation A exhibiting a strong bias towards cooler and more moist conditions over much of the domain. This bias is attributed to the surface parameterization, which generally produces an excessively large evaporation fraction where the average 18Z-23Z top-level soil moisture content exceeds ~43% saturation. The dewpoint depression error in eastern Colorado is less than 5°F, and this may be due to the presence of cloud cover in reality. The free atmosphere forecasts are in much better agreement with observations. Simulation A produces somewhat drier conditions at 500 mb than were observed while the general pattern of mid-level moisture correlates well with the observed pattern. Additional fields from this simulation are presented in the next section for comparison with Simulation B.

## 5.3 Simulation B

The previous section ended with a discussion of the surface fields in Simulation A. In this section, we will begin with those of Simulation B.

### 5.3.1 *Surface forecast*

Figure 5.15 below shows the simulated 00Z July 29, surface temperature, dewpoint temperature and wind, in Simulation B. The simulated temperatures over most of the domain are in much better agreement with observed temperature and dewpoint than in simulation A. Over the southern plains, temperatures are generally within 5°F of observations. Temperatures are approximately 5°F-8°F too warm over the central plains

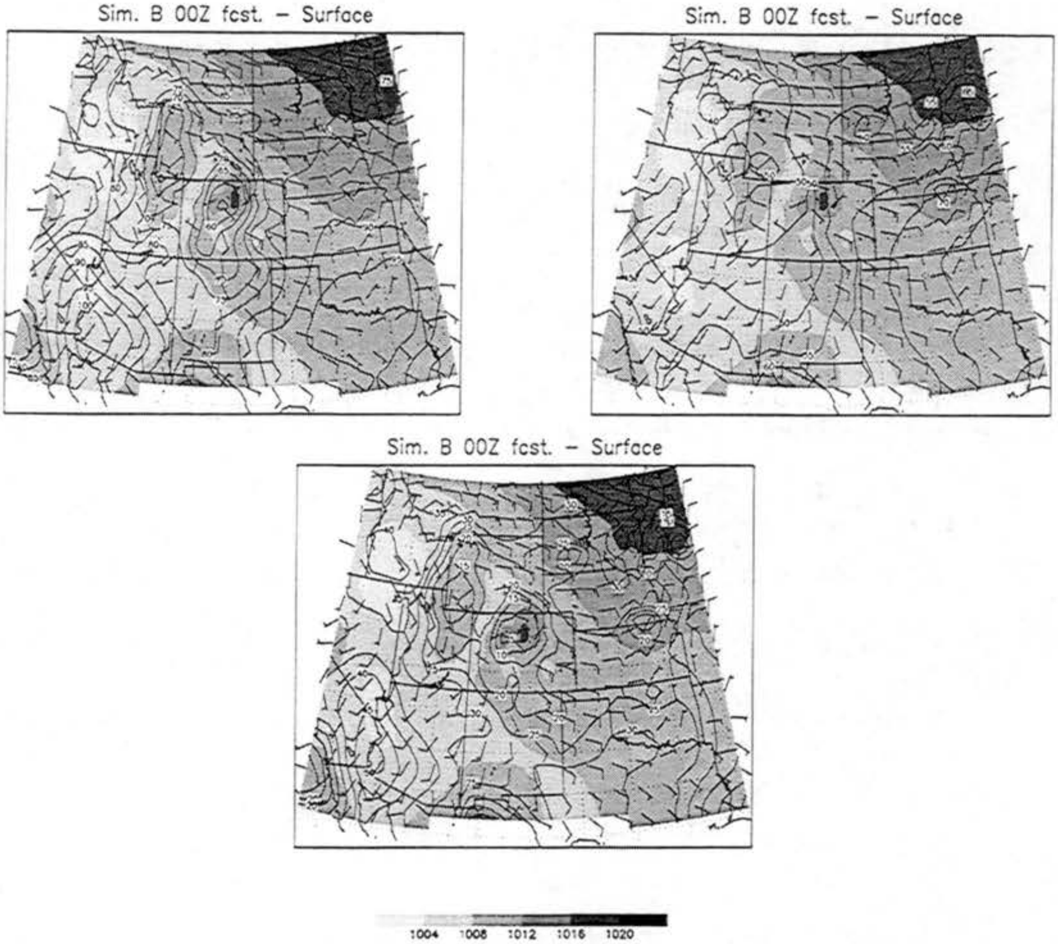


**Figure 5.15** Simulation B 00Z forecast surface fields. Reduced mean sea-level pressure shaded at 4 mb intervals. Top left: Temperature contoured at 5°F intervals. Top Right: Dewpoint temperature contoured at 5°F intervals. Bottom: Dewpoint depression contoured at 5°F intervals. Barb convention is the same as figure 5.2.

and ~5°F too warm in eastern Colorado. The north-south band of less than 65°F temperatures in northeastern Utah and western Wyoming is partly a result of elevation, which is between 2100 and 2400 m in this region, and is also partly due to cloud coverage and precipitation associated with the northward translating shortwave in eastern Utah. Dewpoint temperatures are generally lower in Simulation B than in Simulation A. In eastern Colorado the surface dewpoint is drier than the observation analysis by approximately 5°F-8°F. Over the southern, central and northern plains, dewpoint temperatures are typically within 5°F of observations. Utah and Nevada are also drier than observed with errors between 5°F-8°F, while Idaho experiences more severe errors of (-10°F)-(-15°F).

The forecast dewpoint depression is shown in the lower panel of Figure 5.15. Comparison with Figure 5.5 shows that the dewpoint depressions are generally 10°F larger than observed, and this is true specifically in eastern Colorado. While the overall Grid 1 dewpoint depression forecast is in better agreement with observations than in Simulation A, eastern Colorado dewpoint depressions are actually predicted more accurately in Simulation A than in Simulation B. As discussed at the end of Section 5.2.2, the increased accuracy of surface dewpoint depression forecast in Simulation A may be due to existence of cloud cover over eastern Colorado in reality. This of course raises the possibility that Simulation A, in eastern Colorado accomplishes, through soil moisture, what may have been accomplished through cloud coverage by nature. Due to the inexact representation of topography on Grid 1, and the associated effects on Grid 1 temperature in the vicinity of the Rocky Mountains, this issue will be deferred until Chapter 6 where results from Grids 3 and 4 are presented.

At this point, it is clear that the simulated, low-level thermodynamic fields are strongly influenced by soil moisture initialization. We can now examine the effects of this variation on the synoptic low-level wind field. For this purpose, the surface temperature and winds were averaged using 30 minute output, between 18Z and 00Z for Simulations A and B, and subtracted (Figure 5.16). This yields the mean temperature and wind difference for the afternoon hours after Grid 4 was inserted. The first and most important aspect of this figure is that the average surface temperatures are *everywhere* greater, on Grid 1, in Simulation B than in Simulation A. The minimum temperature differential is 2°F and the maximum is 13°F. The resulting wind field is, with very few exceptions, an upslope wind difference field with respect to the topography and is most pronounced where the temperature difference is maximized. The magnitude of this vector-difference approaches 10 kt in western Kansas, Nebraska and much of New Mexico. West of the Continental Divide in Colorado, the increase in upslope flow component is not as pronounced, with a maximum differential magnitude of 5 kt.

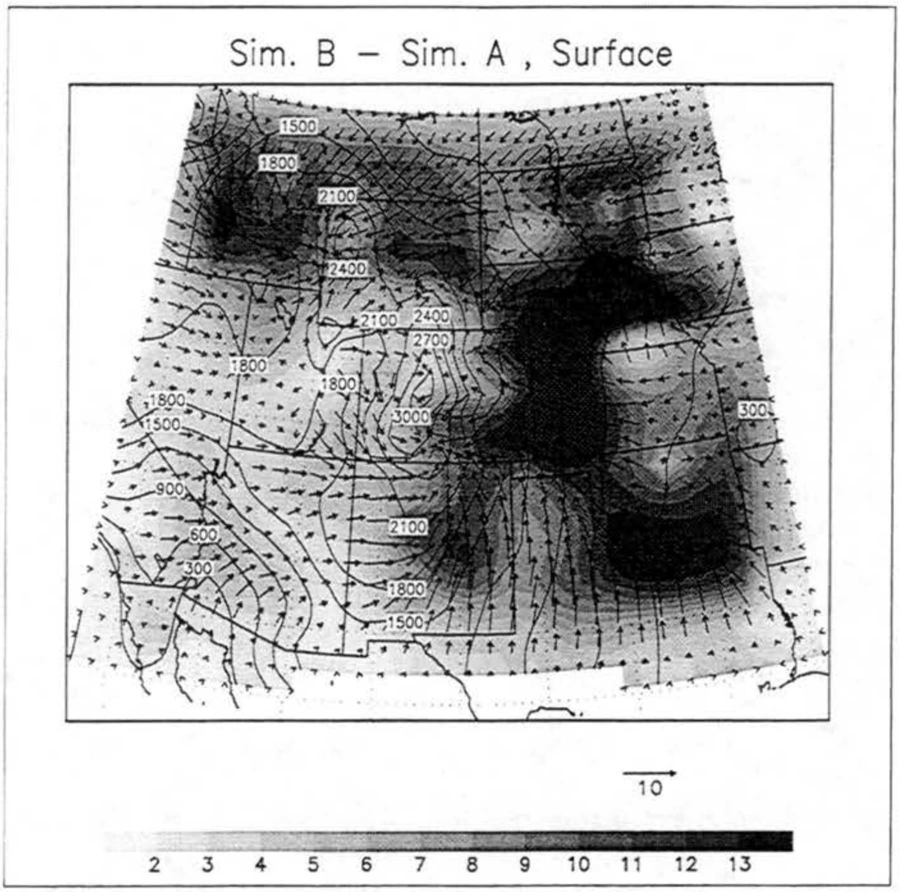


**Figure 5.16** Difference between Sim. B and Sim. A (B-A) temperature and wind field, 18Z - 00Z average. Temperature difference shaded at 1°F interval. Wind vector scale is 10 kt. Topography is contoured at 300m intervals.

The Colorado Rocky Mountains, on Grid 1 are oriented in a more or less north-south configuration with the steepest gradients oriented eastward and westward. Hence, the large-scale upslope flow can be examined through zonal-vertical cross-sections. Figure 5.17 shows cross-sections of the zonal wind velocity and vertical velocity from 100°W to 110°W. These fields are averaged latitudinally between 37°N and 41°N, which correspond to the southern and northern border of Colorado, respectively, and are averaged temporally between 18Z and 00Z using 30 minute output data.

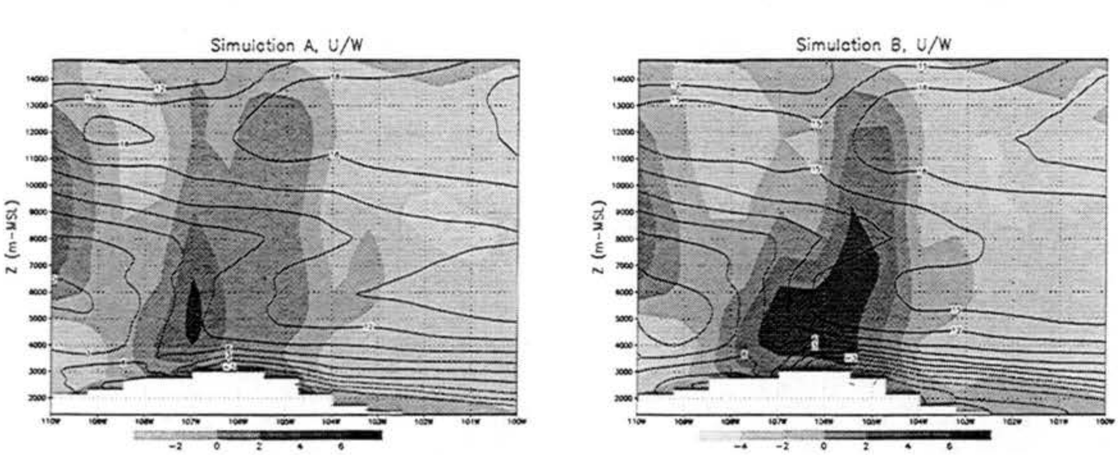


**Figure 5.17** Averaged longitude-height cross sections from Sim. A (left) and Sim. B (right). Zonal velocity (U) contoured at 3-kt intervals. Vertical velocity shaded at 2-cm/s intervals with identical shading scale between plots.

These plots show the gross cross-barrier flow differences between Simulation A and B and the distribution of large-scale vertical motion with respect to the Continental Divide during the afternoon hours. This figure shows, not suprisingly, that the mean easterly upslope flow is approximately 3 kt stronger in simulation B than in A and extends approximately 300 m above that in Simulation A. To the west of the Continental Divide, the westerly upslope flow is marginally increased. The mean vertical motion over the Continental Divide is approximately twice that in Simulation A, and the centroid of the mean low-level vertical motion is shifted slightly eastward toward the increased easterly low-level flow. The 12Z July 28 - 05Z July 29 simulated, Grid 1 accumulated precipitation is shown in Figure 5.18 below.

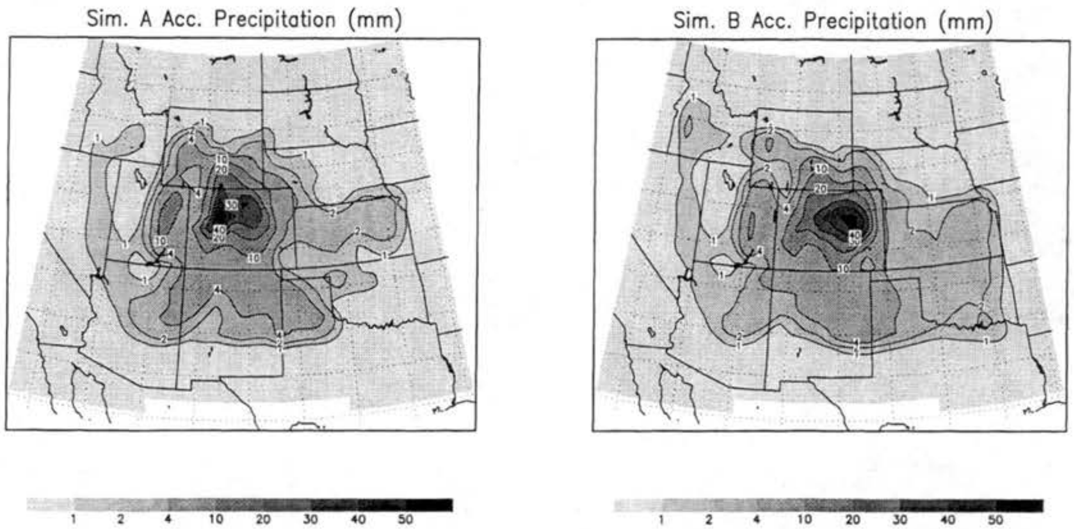


**Figure 5.18** 12Z July 28 - 05Z July 29, simulated, Grid 1, accumulated precipitation in Simulation A (left) and Simulation B (right).

This figure exhibits a similar dichotomy in distribution about the Continental Divide with Simulation A achieving the greatest amounts to the west of the Continental Divide and Simulation B to the east. Again, it should be noted that the cross sections and precipitation forecast are synoptic-scale fields that represent the mean behavior of the atmosphere and yield little information about local extremes in time or space. In addition, the vertical velocity profile implicitly contains the mean vertical motion associated with deep moist convection and should be considered a product of the unresolved convective motions when presented on the synoptic scale. The primary conclusion to be drawn from this output is that Simulation B simulates a stronger, deeper, average upslope, low-level flow primarily east of the Continental Divide, an accompanying increase in large-scale vertical mass transport over and east of the highest terrain, and an eastward shift of the large-scale precipitation maximum to the east of the Continental Divide.

### 5.3.2 *Free-atmosphere*

The left panel in Figure 5.19 below, shows the Simulation B, 00Z, 500 mb forecast. One of the primary differences between this forecast and that of Simulation A is the decreased dewpoint depression, indicative of more moist conditions. The right panel shows the 18Z July 28 - 00Z July 29 averaged difference field at 500 mb.

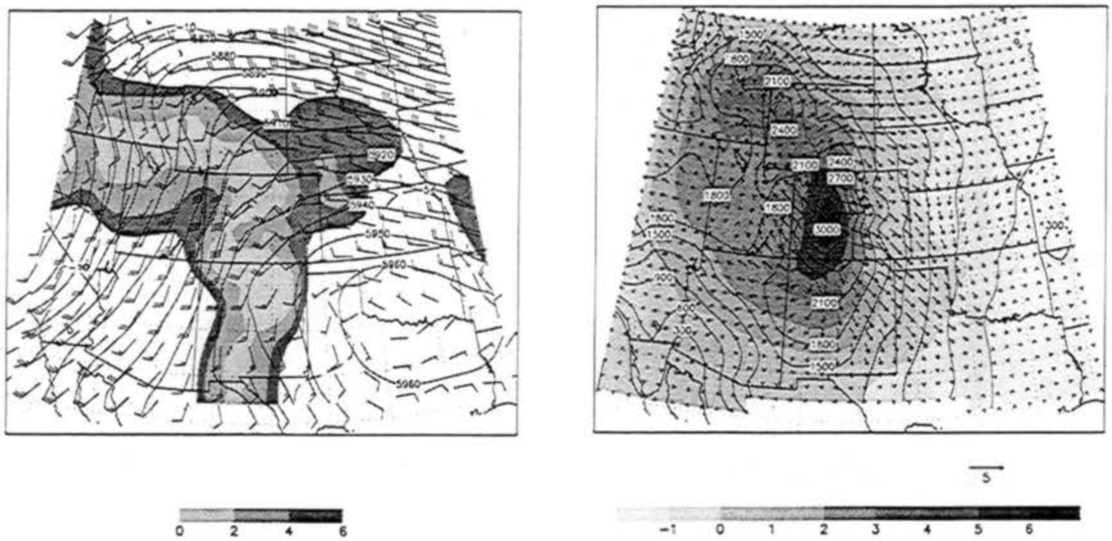


**Figure 5.19** Left: Simulation B, 00Z, 500 mb forecast. Dewpoint depression shaded at 2°C intevals. Heights contoured at 10 m intervals. Barb convention is the same as figure 5.2. Right: 500 height and wind difference field, averaged between 18Z and 00Z. Height is shaded at 1 m intervals. Wind vector scale is 5 kt. Topography is contoured at 300 m intervals.

The differences in geopotential height are relatively minor with maximum differences reaching only 6 m. However the wind field difference is more physically significant and is characterized by a largely, ageostrophic, divergent response with a 5-kt increase in westerlies along the east slopes of the Rocky Mountains. There is some indication of adjustment in the geostrophic component as can be seen in the increased intensity of the anti-cyclonic flow around the positive height difference. The increase in anti-cyclonic flow is expected due to the action of the coriolis force on the divergent, down-gradient ageostrophic flow. The height difference and divergence axis of the difference wind field is closely correlated with the underlying topography, as was the convergent surface difference wind field. Returning to Figure 5.17, it is seen that the primary increase in mean vertical velocity occurs just above the highest terrain and that 500 mb (~5900 m) lies within the region of vertical convergence that characterizes the upper troposphere over the Continental Divide. Hence, the horizontally divergent ageostrophic difference field can most easily be explained by the increase in vertical mass transport below the 500 mb level associated with increased low-level convergence, generally toward the higher terrain. As stated earlier, deep, moist-convection is one of the contributing mechanisms to the mass transport observed in the synoptic-scale vertical motion. As such, one should therefore interpret the increased moisture content at 500 mb in Simulation B, as being associated with the increased participation of moist-convective motions in the large-scale topographic circulation.

Finally, the Simulation B, 00Z, 700 mb forecast is shown in Figure 5.20 below. Comparison with Figure 5.3, shows that upslope flow now exists along the length of the Continental Divide in the southern half of Colorado and northern New Mexico where Simulation A predicted southerly and south-southwesterly flow. In addition, the 00Z vertical velocity field has decidedly shifted east of the Continental Divide in the same regions. Located within the vertical layer of mean vertical divergence (Figure 5.17), the flow field at 700 mb (~3200 m) exhibits increased ageostrophic horizontal convergence east of the Continental Divide, especially in the southern two-thirds of Colorado.

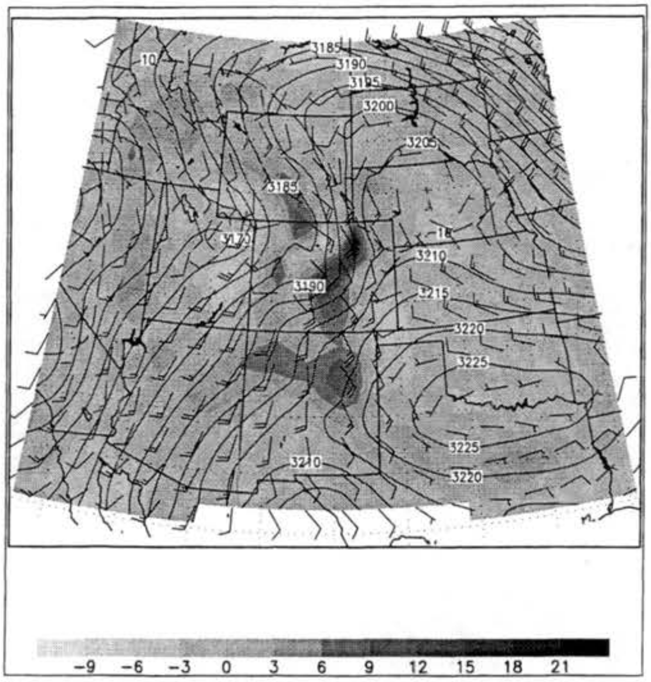


**Figure 5.20** Simulation B, 00Z, 700 mb forecast. Heights are contoured at 5-m intervals. Vertical velocity is shaded at 1-cm/sec intervals. Wind barb convention is the same as Figure 5.2

## 5.4 Summary

In this chapter, the synoptic forecasts were presented and differences between simulations and observations were noted. It was shown that Simulations A and B differ considerably in the boundary layer thermodynamic and wind predictions. Much of this appears to be due to an overestimated evaporation fraction in regions of high soil moisture content in Simulation A. Along with systematically higher surface temperatures and lower surface dewpoint temperatures in Simulation B, an increase in the upslope synoptic circulation was noted. Accompanying the increased topographic flow is an increase in synoptic-scale vertical velocity over the high terrain of Colorado and New Mexico and an eastward shift of the vertical velocity centroid at the Continental Divide. Similarly, the 12Z July 28 - 05Z July 29 large-scale precipitation maximum is also shifted eastward while retaining a comparable magnitude. Lastly, while the Grid 1 dewpoint depression forecast was generally more accurate in Simulation B, that of Simulation A was more accurate over eastern Colorado. In the next chapter, the differences in boundary layer evolution, and the influence of these variations on the behavior of simulated convective elements along the Front Range will be examined.

# 6

# Pre-storm and Convective Evolution

## 6.1 Introduction

In this chapter the preconditioning of the storm environment, and its influence on the convective evolution are investigated. The roles of storm precipitation and propagation characteristics in determining accumulated precipitation are examined and differences between simulations are noted.

## 6.2 Pre-conditioning of the storm environment

### 6.2.1 *Three-Grids (12Z-18Z)*

We begin by examining the 15Z-18Z precipitation evolution in both simulations. As noted in Section 4.2.2, precipitating microphysical species — rain, hail, graupel, snow, aggregates, and pristine ice — are activated at 15Z in this 3-grid portion of the simulation. Figure 6.1 shows the 15Z-18Z precipitation rate on Grid 3 for both simulations. During this period, two areas of precipitation form, one of which is located along the Colorado-Wyoming border and another located ~130 km to the southeast of Denver. Both areas of precipitation propagate north-northeastward at 8-10 m/s.

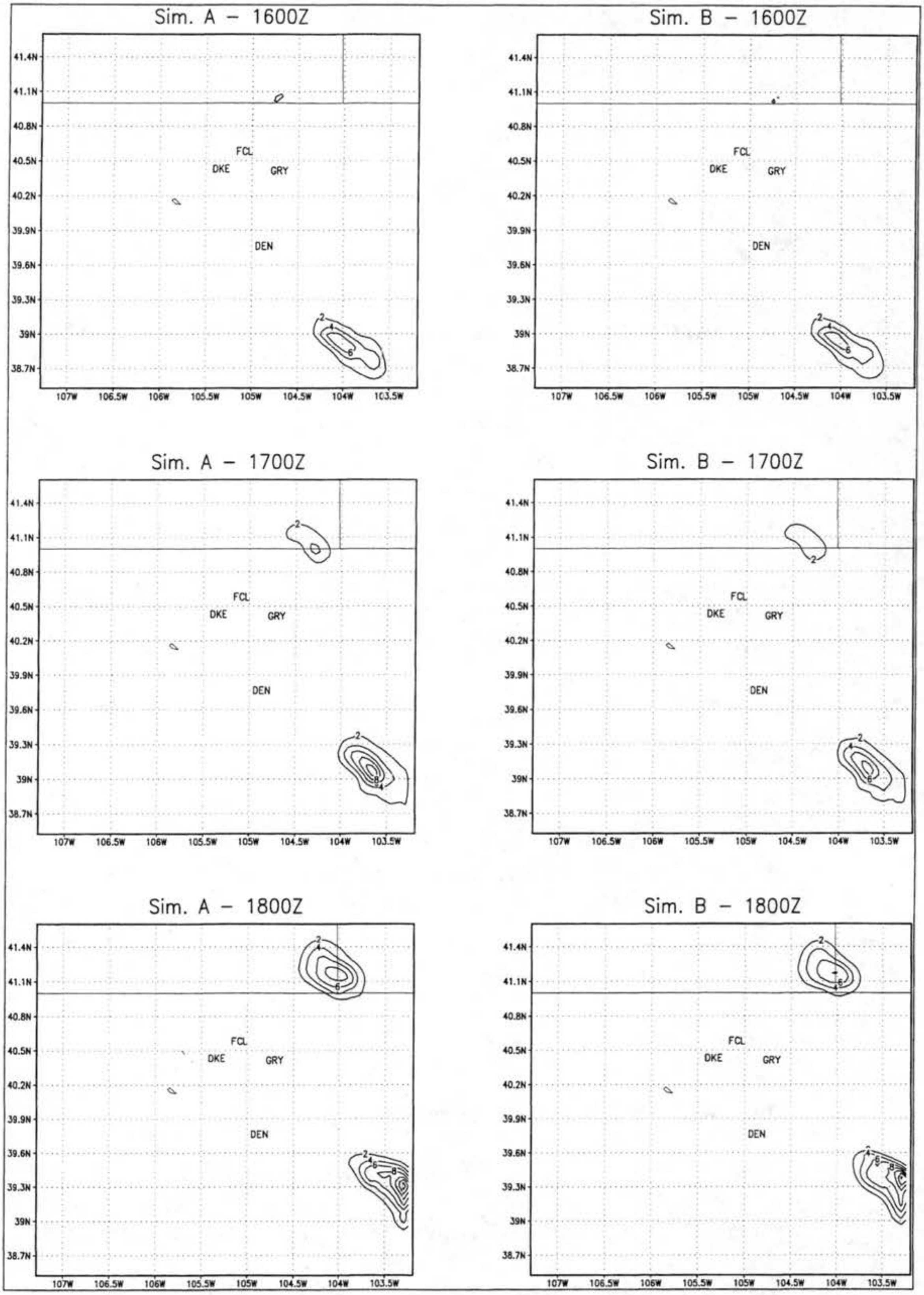


**Figure 6.1** 15Z - 18Z precipitation rate in Simulations A and B. Precipitation rate is contoured at 1 mm/hr intervals. Fort Collins, Drake, Greeley and Denver are shown for geographical reference.

The maximum precipitation rates in Simulation A during this time are 9 and 15 mm/hr for the northern and southern systems respectively. The Simulation B precipitation evolution is very similar with a precipitation intensity that is ~1mm/hr less than that of Simulation A. After 18Z, both systems dissipate. The accumulated precipitation is shown in Figure 6.2. The accumulated precipitation patterns and magnitudes (~10 mm) are similar with Simulation B exhibiting ~1mm less accumulated precipitation at the maxima than Simulation A.

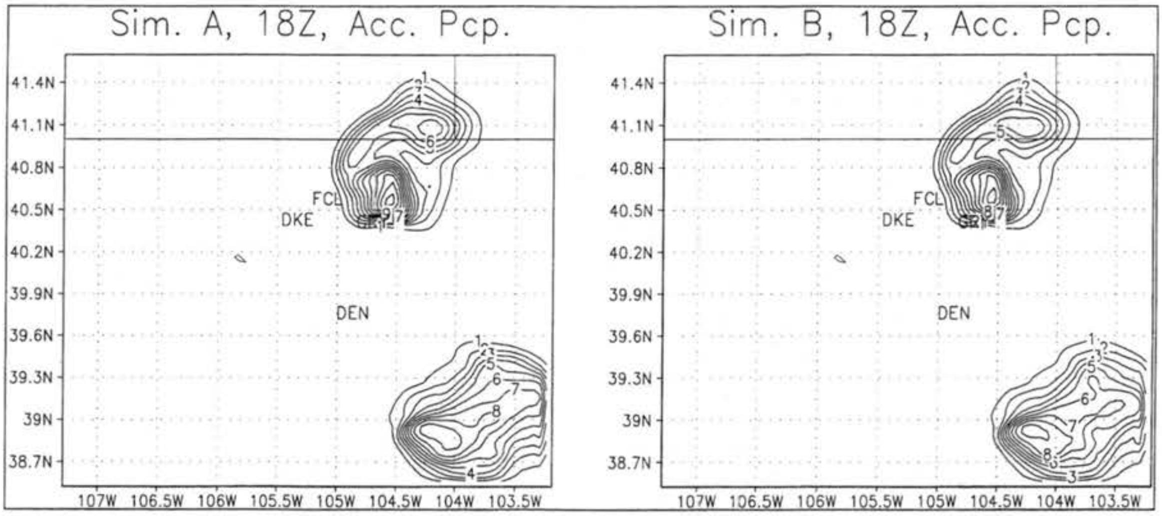


**Figure 6.2** 18Z, Grid 3, accumulated precipitation for Simulations A and B. Contour interval is 1 mm.

The resulting 18Z, top-level soil-moisture content is shown in Figure 6.3. Comparison with the initial soil moisture field (Figure 4.10 and 4.5) shows relatively minor modifications in Simulation A and more significant moistening to the north of Greeley and southeast of Denver in Simulation B, associated with the 15Z-18Z precipitation. The Grid 3 average soil-moisture decreases in Simulation A from 0.229 $m^3/m^3$ (54% saturation) at 12Z to 0.197 $m^3/m^3$ (47% sat.) at 18Z, while the variability, characterized here by the standard deviation, increases slightly from 0.038 $m^3/m^3$ to 0.045 $m^3/m^3$. Simulation B experiences a small net moistening as the average increases from 0.075 $m^3/m^3$ (18% sat.) at 12Z to 0.084 $m^3/m^3$ (20% sat.) at 18Z, with an increase in variability from 0.030 $m^3/m^3$ to 0.043 $m^3/m^3$.

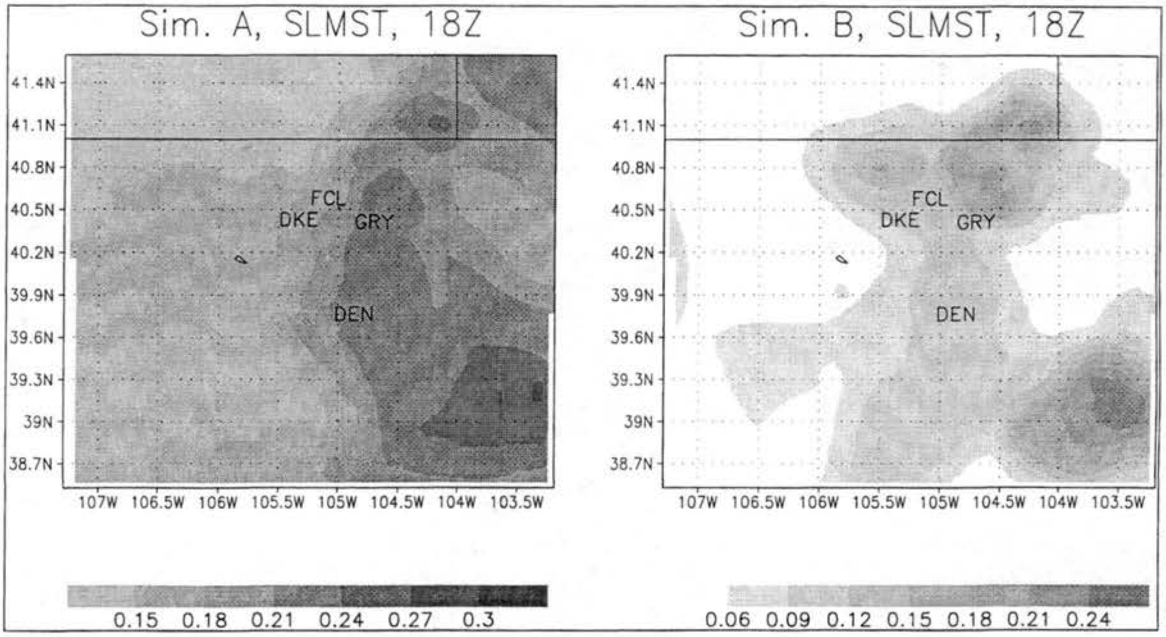


**Figure 6.3** 18Z, Grid 3, volumetric soil-moisture content for Simulations A and B. Shading interval is 0.03 $m^3/m^3$. Shading scale is identical between panels.

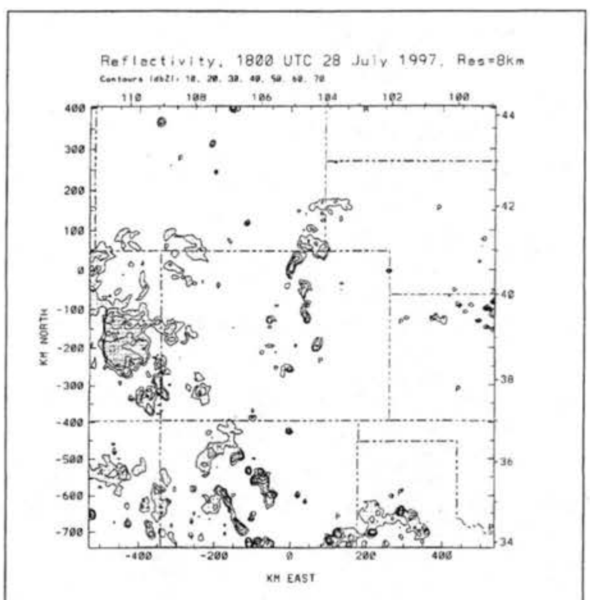


**Figure 6.4** Radar reflectivity at 1800Z, 28 July 1997. Reflectivity contoured at 10-dBZ intervals (Courtesy of Global Hydrology Resource Center and Ray McAnelly).

Clearly, the gross differences in the initial moisture fields, namely the relative average dryness of Simulation B and the moist conditions of Simulation A, have changed little relative to the initial characteristics. Comparison of the 18Z precipitation rate (Figure 6.1) and the 18Z radar mosaic (Figure 6.4 above) shows that precipitation did occur over the Colorado-Wyoming border. However the precipitation over Denver and Fort Collins is not reproduced and overall, the agreement between the simulation and the radar mosaic, in terms of location and coverage is poor.

Next, we consider the low-level wind and thermodynamic evolution. Figure 6.5 below shows the initial, 12Z, 28 July, Grid 3 winds surface temperature and dewpoint temperature.

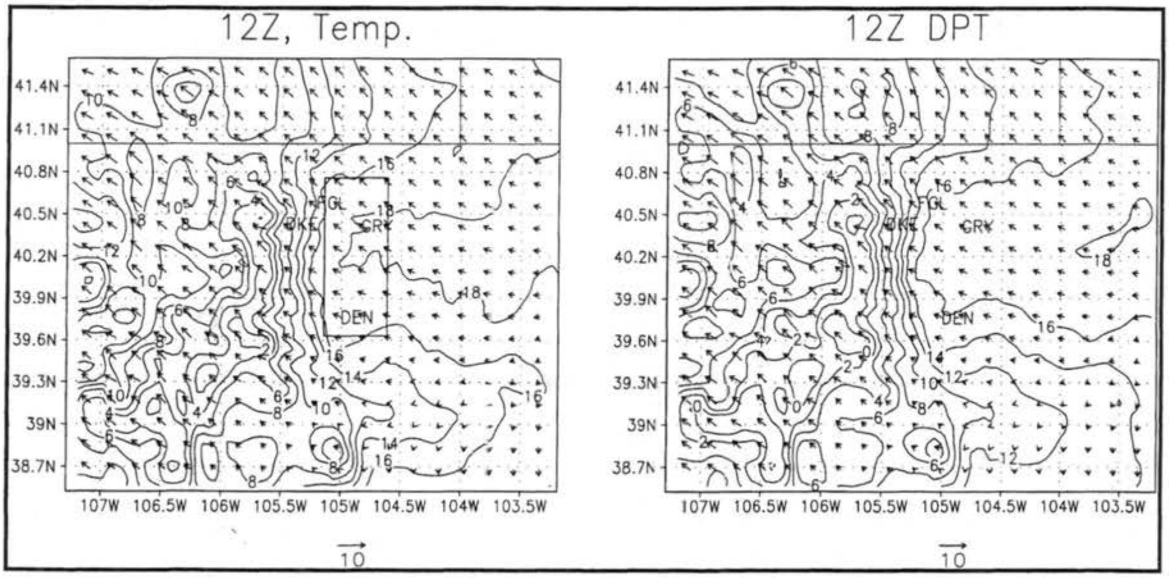


**Figure 6.5** Initial (12Z) temperature, dewpoint and winds at surface (50m-AGL). Temperature and dewpoint contoured at 2°C intervals. Wind vector scale is 10 m/s. Rectangle in left panel shows averaging area used for quantities in Table 6.1.

The reader is reminded that the initial (12Z) atmospheric fields are identical for each simulation. Winds along the Front Range are southeasterly at 3-4 m/s and the 50-m (AGL) temperature is 17°C-18°C. The dewpoint depression at the same level is less than

2°C. Figure 6.6 below shows the 18Z forecast surface temperature, dewpoint and winds for Simulations A and B. By 18Z significant differences in the low-level thermodynamic fields have developed. Simulation B is warmer over much of the domain with differences ranging from 0°C to 8°C. In addition, Simulation B is drier with dewpoint temperatures 2-4°C colder than in Simulation A.

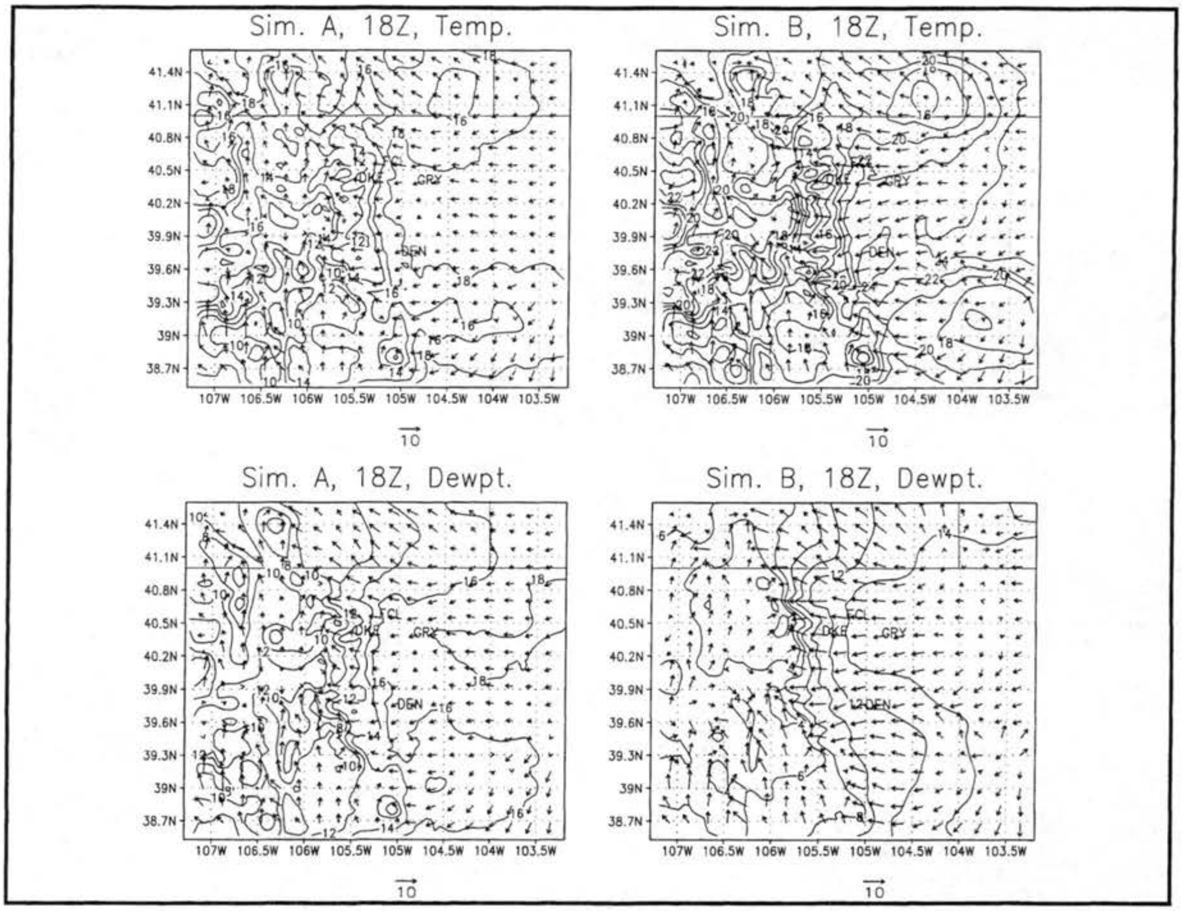


**Figure 6.6** 18Z Temperature (top), dewpoint (bottom) and winds for simulations A (left) and B (right). Temperature and dewpoint contoured at 2°C intervals. Wind vector scale is 10 m/s.

As is evident in Figure 6.6, the cold pools associated with the precipitating regions are approximately 6°C colder, relative to the environment, in Simulation B than in Simulation A. Given the nearly identical precipitation rates between simulations, it is likely that this is the result of the increased, low-level, environmental dewpoint depression, in Simulation B, which is apparent over the majority of Grid 3. Despite the increased low-level convergence on the windward peripheries of the Simulation B cold-pools, no convective storms occur within the eventual location of Grid 4 in association with these boundaries after 18Z. The effect of low-level dewpoint depression on cold-pool characteristics and storm propagation is considered in detail in Section 6.3.3.

| **Variables** | **12Z** | **18Z** | |
|---|---|---|---|
| | | **Sim. A** | **Sim. B** |
| $\overline{T}$ (°C) | 17.4 | 18.3 | 22.9 |
| $\overline{T}_d$ (°C) | 16.4 | 16.8 | 14.0 |
| $\overline{u}$ (m/s) | -2.75 | -3.11 | -5.87 |
| $\overline{v}$ (m/s) | +1.70 | -0.79 | -0.98 |
| *CAPE* (J/kg) | 184 | 214 | 294 |
| *CIN* (J/kg) | 59 | 52 | 58 |
| *LCL* (m-AGL) | 639 | 668 | 1176 |
| *LFC* (m-AGL) | 2653 | 2770 | 2733 |
| *PWAT* (cm) | 3.77 | 3.40 | 3.24 |
| $\overline{\theta}_e$ (K) | 344.0 | 346.0 | 345.1 |
| AE (W/m$^2$) | 10 | 463 | 593 |
| *EF* (Dimensionless) | 4.24 | 0.86 | 0.60 |
| $D_{BL}$ (m) | — | ~370 | ~660 |

**Table 6.1** Horizontally averaged quantities at 12Z and 18Z for simulations A and B. Quantities are described in text, units are indicated and area of averaging is shown in the left panel of Figure 6.5

In order to summarize the 18Z simulation differences, Table 6.1 is presented above. The quantities in this table represent the average of each field over the rectangular area shown in the left panel of Figure 6.5. This table shows, following the order presented in the table, 50m-temperature ($T$), dewpoint temperature ($T_d$), zonal ($u$) and meridional ($v$) wind components, convective available potential energy ($CAPE$), convective inhibition ($CIN$), the height of the lifted condensation level ($LCL$) and level of free convection (*LFC*) with respect to the average elevation, precipitable water (*PWAT*), 50m-equivalent potential temperature ($\theta_e$, or "theta-e"), evaporation fraction (*EF*), and the boundary layer depth ($D_{BL}$). Here, the top of the boundary layer is defined as the first grid point, starting from the lowest model level, at which the potential temperature lapse rate is greater than 1.0°C/km. In reality, the boundary layer top is not well defined in either simulation due to the coarse vertical and horizontal grid spacing. Therefore, $D_{BL}$ is simply an approximate quantification of the difference in boundary layer structure between simulations.

The results in this table indicate what has already been noted; namely, that Simulation B is warmer and drier at the surface than Simulation A at 18Z. The effect on the lifted condensation level is an increase from 668 m (AGL) in Simulation A to 1.18 km (AGL) in Simulation B. Both simulations exhibit a decrease in precipitable water from the initial condition which, itself, is ~0.6 cm higher than that of the 12Z Denver sounding. Examination of the low-level wind field during the adjustment phase of integration (not shown), shows that this is due to a downslope wind that develops in the first two-hours of integration, which temporarily dries the low-level air over the averaging area. The upslope surface winds recover by 1600Z in Simulation A, and by 1430Z in Simulation B. The upslope component in Simulation B is almost twice that of Simulation A at 1800Z. This earlier recovery and higher intensity of the upslope flow in Simulation B is consistent with the synoptic-scale differences shown in Chapter 5, in which higher surface temperature along sloping surfaces led to an enhanced upslope wind. The CAPE is still relatively low at 18Z in comparison to the Denver 00Z sounding

CAPE of 703 J/kg, an expected result given that only 6 hours of solar irradiation has occurred in the simulation.

It is also interesting to note that the increased low-level dewpoint in Simulation A, compensates the increased low-level temperature in Simulation B, resulting in an equivalent potential temperature difference, between simulations of only 0.9 K at 18Z. The effect of available energy partitioning on the equivalent potential temperature can be better understood by considering a simple example.

We begin with the differential, parcel definition of the equivalent potential temperature, $\theta_e$:

$$d \ln \theta_e = d \ln \theta + \frac{L}{C_p T} dq, \qquad (6.1)$$

where $\theta$ is the dry potential temperature, $L$ is the latent heat of condensation, here approximated to be independent of temperature, $C_p$ is the specific heat of air at constant pressure, $T$ the absolute temperature and $q$, the water vapor mixing ratio. Multiplying this equation by $C_pT$ we have,

$$C_p T d \ln \theta_e = C_p T d \ln \theta + L\, dq \, .$$

However, the first law of thermodynamics, is written:

$C_p T d \ln \theta = dh$, where $dh$ is the specific, differential diabatic heating. Hence,

$$C_p T d \ln \theta_e = dh + L\, dq \, .$$

If, for simplicity, we neglect boundary layer entrainment and consider $dh$ to be provided to a mixed layer parcel solely from the surface sensible heating, then the specific diabatic heating can be expressed as, $dh = \frac{SH}{\rho_0 D} dt$, where $SH$, is the surface sensible heat flux, $\rho_0$ is the characteristic mass density of the mixed layer and $D$ is the mixed layer depth. Here we have also assumed that the mixed-layer remains unsaturated. However, the argument can easily be augmented to include latent heat release for saturated conditions, as this process is, in fact, the usual motivation for the differential law expressed in Eq. 6.1. However, diabatic heating associated with cloud radiation within the mixed layer is excluded from consideration. With these simplifications, we have,

$$C_p T d \ln \theta_e = \frac{SH}{\rho_0 D} dt + L\, dq .$$

Recalling that the surface available energy flux is defined as $AE = SH + LH$, where $LH$ is the surface latent heat flux, we can write,

$$C_p d \ln \theta_e = \frac{AE}{\rho_0 D} dt - \frac{LH}{\rho_0 D} dt + L\, dq \tag{6.2}$$

The latent heat flux is simply, $LH = L \cdot F_v$, where $F_v$ is the vapor mass flux at the lower boundary. Hence,

$$\frac{LH}{\rho_0 D} dt = \frac{L \cdot F_v}{\rho_0 D} dt = L\, dq .$$

Substituting this into (6.2) gives,

$$C_p T d \ln \theta_e = \frac{AE}{\rho_0 D} dt. \tag{6.3}$$

Hence, for a non-entraining mixed layer in which the lower boundary is the only source of diabatic heating and water vapor, the change in mixed-layer equivalent potential temperature is primarily dependent on the available surface energy and the mixed layer depth. The available energy, neglecting surface radiative emission and heat storage is largely controlled by incident solar radiation during the daytime. Hence, given identical surface available energy, and identical mixed layer depth, the partitioning of solar radiation into latent and sensible heat components is, under the preceding assumptions, immaterial to the evolution of equivalent potential temperature.

This result identifies available surface energy as a direct mechanism for changing the mixed-layer equivalent potential temperature, while sensible heating has both a direct and indirect effect. The direct effect, which is not included in (6.3) is the effect of mixed-layer entrainment, which is primarily controlled by the surface sensible heat flux, while the indirect effect, which is included in (6.3), is the mixed layer depth, an integral result of the direct effect. Betts and Ball (1995), derive an expression for the local time derivative of equivalent potential temperature which includes the effects of entrainment:

$$C_p T \frac{\partial}{\partial t} \ln \theta_e \cong \frac{AE \cdot g}{P_i}\left[1 + A_r \frac{(\beta_i + 1)(\beta_s - \beta_v)}{(\beta_s + 1)(\beta_i - \beta_v)}\right]. \tag{6.4}$$

Here, $\beta_i$ and $\beta_s$ are the inversion-base and surface Bowen ratios, respectively. $A_r$ is the entrainment parameter, which relates the inversion base heat flux to the surface heat flux:

$$F_{i\theta} = -A_r F_{s\theta}, \qquad \text{and} \qquad A_r > 0.$$

$\beta_v \cong -0.07$, is the slope of a dry adiabat on a $C_pT$, $Lq$ diagram, and $P_i$ is the pressure depth of the mixed layer. Equation (6.4) will not be used quantitatively in this thesis but is presented to qualitatively illustrate the direct effect of entrainment on $\theta_e$ evolution. Given that $A_r$ is positive, the term which is generally responsible for the negative entrainment contribution to the equivalent potential temperature tendency is $(\beta_i - \beta_\upsilon)$, since $\beta_i$ is negative and generally has a magnitude which is greater than 0.07 during daylight hours when the boundary layer is growing (Betts and Ball, 1995).

Given the 28% larger available energy flux in Simulation B, one might expect a significantly higher equivalent potential temperature in that simulation. However, the evaporation fraction in Simulation B is 0.60 compared to 0.86 in Simulation A, resulting in a sensible heat flux of 237 W/m$^2$ compared to 65 W/m$^2$ in Simulation A. The influence of the sensible heat flux on boundary layer growth is evidenced by the 75% deeper, boundary layer of Simulation B. Hence, boundary layer entrainment is acting to completely offset the increase in available surface energy above that of Simulation A. We will investigate this in more detail in the next section where the 18Z-20Z, Grid 4 evolution is discussed.

The focus on the low-level $\theta_e$ evolution is necessary for two reasons. Firstly, the equivalent potential temperature determines the moist adiabat, on a skew-T diagram, that a parcel ascends after reaching the LCL. The intersection of the environmental, free-atmosphere temperature profile with this moist adiabat determines both the LFC and the equilibrium-level (EL) and hence the CAPE which determines the potential strength of storm updrafts. Secondly, the surface equivalent potential temperature is also related in a one-one fashion to the low-level wet-bulb temperature, the temperature at which a parcel will become saturated if precipitation is evaporated into a surface parcel at constant pressure. This effect can be expected to influence cold-pool thermodynamic properties, whose relationship to the environmental *dry* potential temperature, partially determines the cold-pool propagation characteristics. Hence, this parameter may potentially influence not only precipitation rate, through the updraft intensity, but also storm movement, via the cold-pool.

### 6.2.2 *18Z-20Z (Grid 4)*

In this section the precipitation evolution and low-level thermodynamic changes between 18Z and 20Z in both simulations, are summarized. Figure 6.7 below shows the 19Z-20Z precipitation rate at 30 minute intervals for both simulations. In all discussions to follow, the maximum precipitation rate associated with a storm is the maximum grid-point value. Storm motion or propagation speed is defined with respect to the location of the central maximum of the precipitation rate. The term quasi-stationary refers to storms whose motion is less than 1.0 m/s.

In Simulation A, precipitation starts at 1830Z (not shown) over the high terrain in the western portion of Grid 4. Between 1830Z and 2000Z these storms move in variable directions at speeds ranging from quasi-stationary to 1.5 m/s. By 2000Z the maximum precipitation rate is 12 cm/hr which occurs at (105.7°W, 40.1°N) and (105.4°W, 39.4°N). Simulation B shows a similar evolution with convection initiating over the highest terrain at 1830Z. These storms propagate eastward at 1-2 m/s, with the exception of the storm located at (105.4°W, 39.6°N) which propagates eastward at 4 m/s.

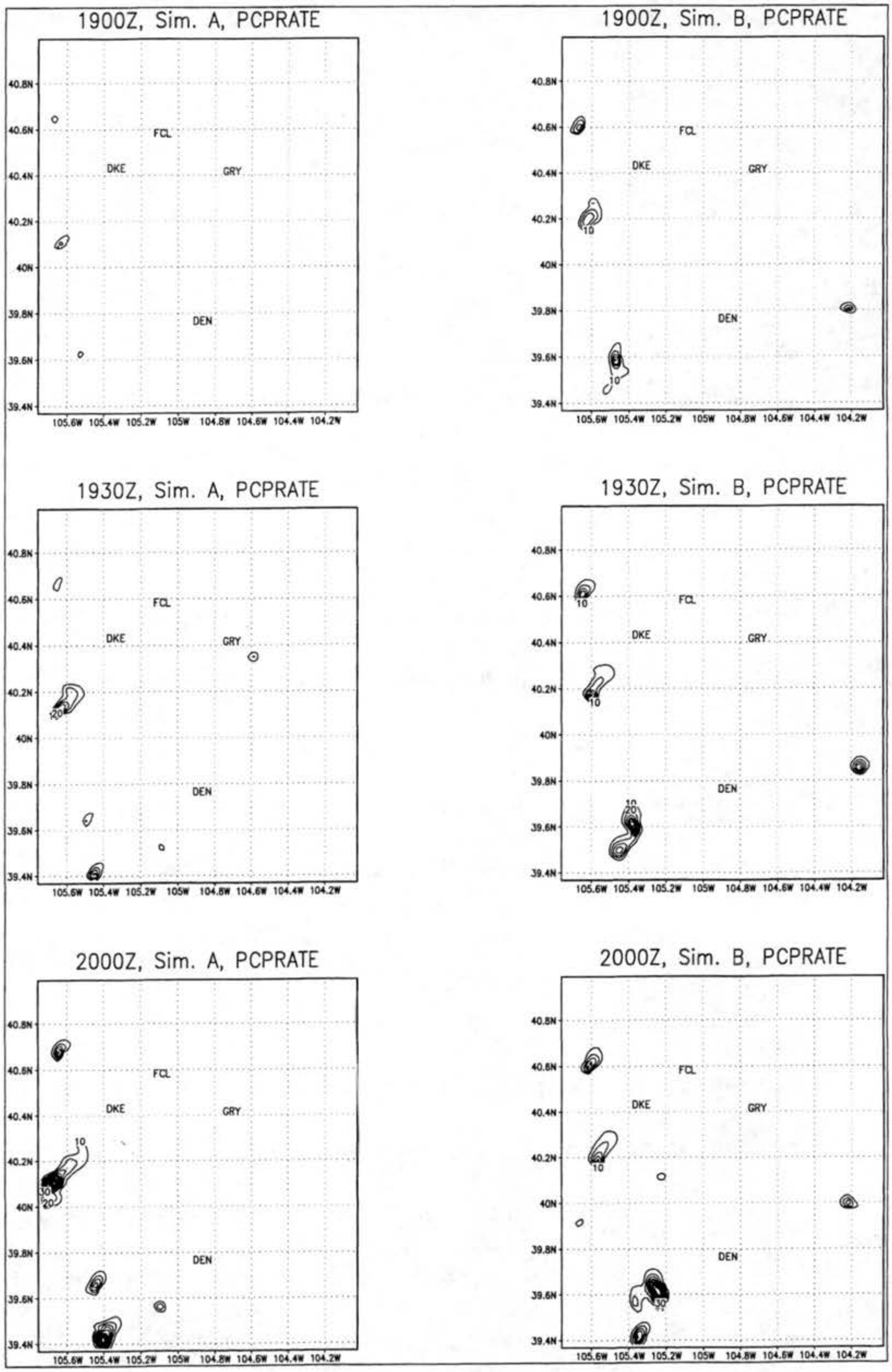


**Figure 6.7** Precipitation rate at 1900Z, 1930Z and 2000Z, for Simulations A (left) and B (right). Contour interval is 10mm/hr.

At 2000Z, the maximum precipitation rate is 11 cm/hr in this storm with other storms precipitating at 0.4-0.5 cm/hr. Simulation B exhibits slightly higher precipitation rates soon after convective initiation while Simulation A meets and exceeds these rates by 2000Z. In addition, Simulation B storms demonstrate marginally higher propagation speeds. Both simulations concentrate the majority of the 1800Z-2000Z precipitation over the higher terrain where the elevation exceeds 2400 m.

| **Variables** | **1900Z** | | **1930Z** | | **2000Z** | |
|---|---|---|---|---|---|---|
| | **Sim. A** | **Sim. B** | **Sim. A** | **Sim. B** | **Sim. A** | **Sim. B** |
| $\overline{T}$ (°C) | 18.9 | 24.7 | 19.2 | 25.4 | 19.5 | 25.9 |
| $\overline{T}_d$ (°C) | 17.6 | 14.1 | 18.0 | 13.8 | 18.3 | 13.4 |
| $\overline{u}$ (m/s) | -3.68 | -6.87 | -4.05 | -7.00 | -4.00 | -6.43 |
| $\overline{v}$ (m/s) | +0.20 | -0.26 | +0.46 | +0.49 | +0.48 | +1.01 |
| $CAPE$ (J/kg) | 594 | 632 | 839 | 700 | 1057 | 722 |
| $CIN$ (J/kg) | 9 | 24 | 2 | 16 | 2 | 10 |
| $LCL$ (m-AGL) | 615 | 1340 | 590 | 1449 | 590 | 1569 |
| $LFC$ (m-AGL) | 1657 | 2309 | 1121 | 2213 | 831 | 2012 |
| $PWAT$ (cm) | 3.51 | 3.30 | 3.58 | 3.35 | 3.68 | 3.45 |
| $\overline{\theta}_e$ (K) | 349.0 | 347.5 | 350.5 | 347.7 | 351.8 | 347.5 |
| $AE$ (W/m$^2$) | 375 | 598 | — | — | 376 | 565 |
| $EF$ (Dimensionless) | 0.90 | 0.28 | — | — | 0.93 | 0.34 |
| $D_{BL}$ (m) | ~370 | ~900 | ~370 | ~1100 | ~370 | ~1300 |

**Table 6.2** Average variables from Simulations A and B at 1900Z, 1930Z, and 2000Z. Surface energy variables (EF, AE) only available at hourly intervals. Simulation A variables are shaded for clarity.

Despite the similarity in precipitation evolution between simulations, the 18Z-20Z period is that in which these simulation become markedly different in the low-level thermodynamic characteristics, a continuation of the trend seen at 1800Z. Table 6.2 shows the same variables that were shown in Table 6.1, but for 1900Z, 1930Z, and 2000Z. The averages in this table are performed over the same area as that of Table 6.1

except that the averages are done on Grid 4, which is inserted at 1800Z. Simulation A experiences an increase in surface temperature of 0.3°C/hr while Simulation B increases by approximate 0.6°C/hr. By 2000Z, Simulation B is 6.4°C warmer than Simulation A. While Simulation A experiences a steady increase in dewpoint temperature of ~0.3°C/hr, the dewpoint in Simulation B decreases steadily at a rate of ~0.3°C/hr. Hence the dewpoint depression in Simulation A remains nearly constant while that of Simulation B increases, reaching over 12°C at 2000Z. The effect of this on the LCL can be seen as Simulation A retains a ~600-m (AGL) LCL while that of Simulation B reaches 1569 m by 2000Z.

As at 1800Z, Simulation B has a larger available energy flux than that of Simulation A between 1900Z and 2000Z. However, the equivalent potential temperature in Simulation B remains steady at ~347.6 K, while that of Simulation A increases at a mean rate of 1.2 K/hr. Here, the direct and indirect effects of sensible heating in a moist low-level environment become apparent. The Simulation B boundary layer grows from 900 m to 1300 m, over 4 times that of Simulation A, in which the boundary layer depth remains nearly constant at 350-400 m. The increased depth and entrainment leading to this increase act to offset the effect of available energy input on $\theta_e$. This is shown graphically in Figure 6.8 below, which shows the area-averaged potential temperature profile in the lowest few kilometers for both simulations at 2000Z. As noted earlier, it is difficult to precisely define the boundary layer top. However, the two profiles are clearly distinguishable, with Simulation B exhibiting a more dry-neutral/unstable profile through a greater depth. This, along with the quantitative parameter, $D_{BL}$, is justification for attributing the $\theta_e$ sink to entrainment in Simulation B.

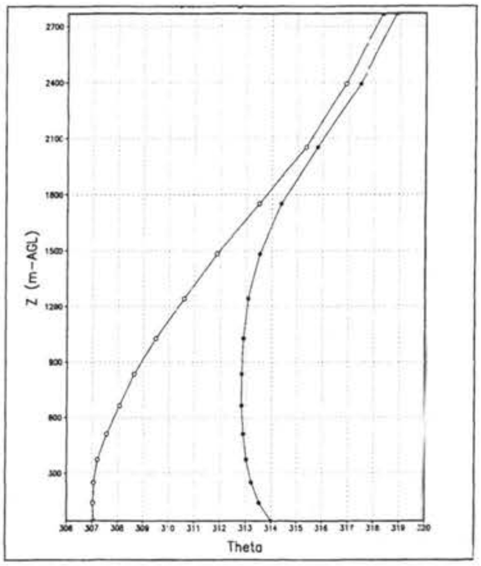


**Figure 6.8** 2000Z average potential temperature profile for Simulations A (open circles) and B (solid circles). Averaging area is shown by the rectangle in Figure 6.9.

Figure 6.9 shows the Simulation A, 1900Z surface equivalent potential temperature and equivalent potential temperature advection. The left panel shows that a southwest-northeast oriented area of enhanced $\theta_e$ exists to the north and east of Denver, which places the averaging area in a region of positive $\theta_e$ advection.

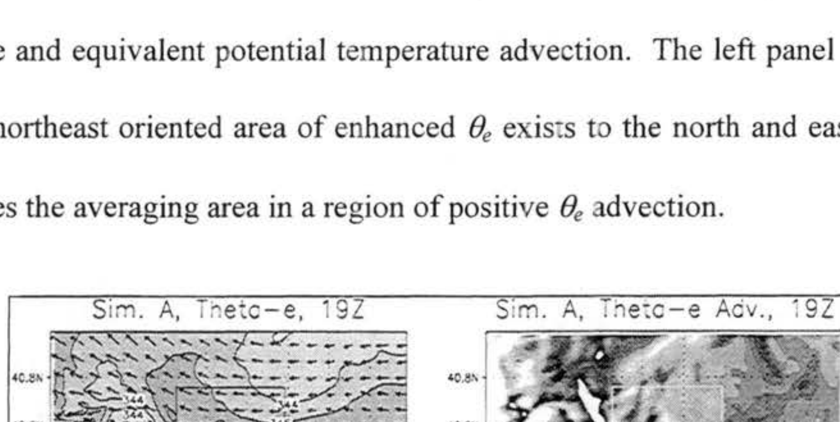


**Figure 6.9** Simulation A, 1900Z, surface equivalent potential temperature and winds (left) and equivalent potential temperature advection (right). Equivalent potential temperature shaded and contoured at 2K intervals. Wind vector scale is 10 m/s and plotted at every fifth gridpoint. Equivalent potential temperature advection contoured at 1K/hr intervals. Values with absolute value ≥ 5K/hr are not plotted. Averaging rectangle is shown.

We must remember that equations 6.2 and 6.4 are for a boundary layer parcel in which the time differential is applied following the horizontal motion. The local, or partial time derivative will consist of the available energy (source) and entrainment (sink) forcing terms in these equations along with an advective source: $-\vec{\mathbf{V}}\cdot\nabla\theta_e$, where $\vec{\mathbf{V}}$ is the horizontal velocity vector (vertical advection is neglected near the surface). The area-averaged advection, which is the advective source for the local time derivative of the area-averaged $\theta_e$ in Table 6.2, is obtained by averaging the grid-point advection shown in Figure 6.9. Averaging yields an advective source of ≅ +0.5 K/hr. Hence, approximately 40% of the $\theta_e$ change within the averaging area can be explained by the advective source. The remaining 1.0 K/hr is the minimum value associated with the area-averaged available energy source, $\left\langle \frac{\theta_e}{C_p T}\frac{AE}{\rho_0 D}\right\rangle$, since the entrainment term is a sink.

The nearly constant boundary layer depth, LCL, and dewpoint depression in Simulation A is largely a result of the high evaporation fraction (>0.9) between 1900Z and 2000Z. Again, we are confronted with a very high evaporation fraction around high noon. This issue was already considered in some detail in Chapter 5 during examination of the synoptic-scale forecasts. In this case however, the available energy is significantly lower. In fact, the available energy between 1900Z and 2000Z in Simulation A is comparable to the 1400Z available energy in Figure 5.9 for Tulsa. Recalling Figure 5.10, from Betts and Ball (1995), the average evaporation fraction for each of the three soil-moisture categories was in fact around 0.8 at 1400Z. In short, it is difficult to assess the plausibility of this evaporation fraction given the relatively low surface available energy flux east of the Front Range foothills in Simulation A.

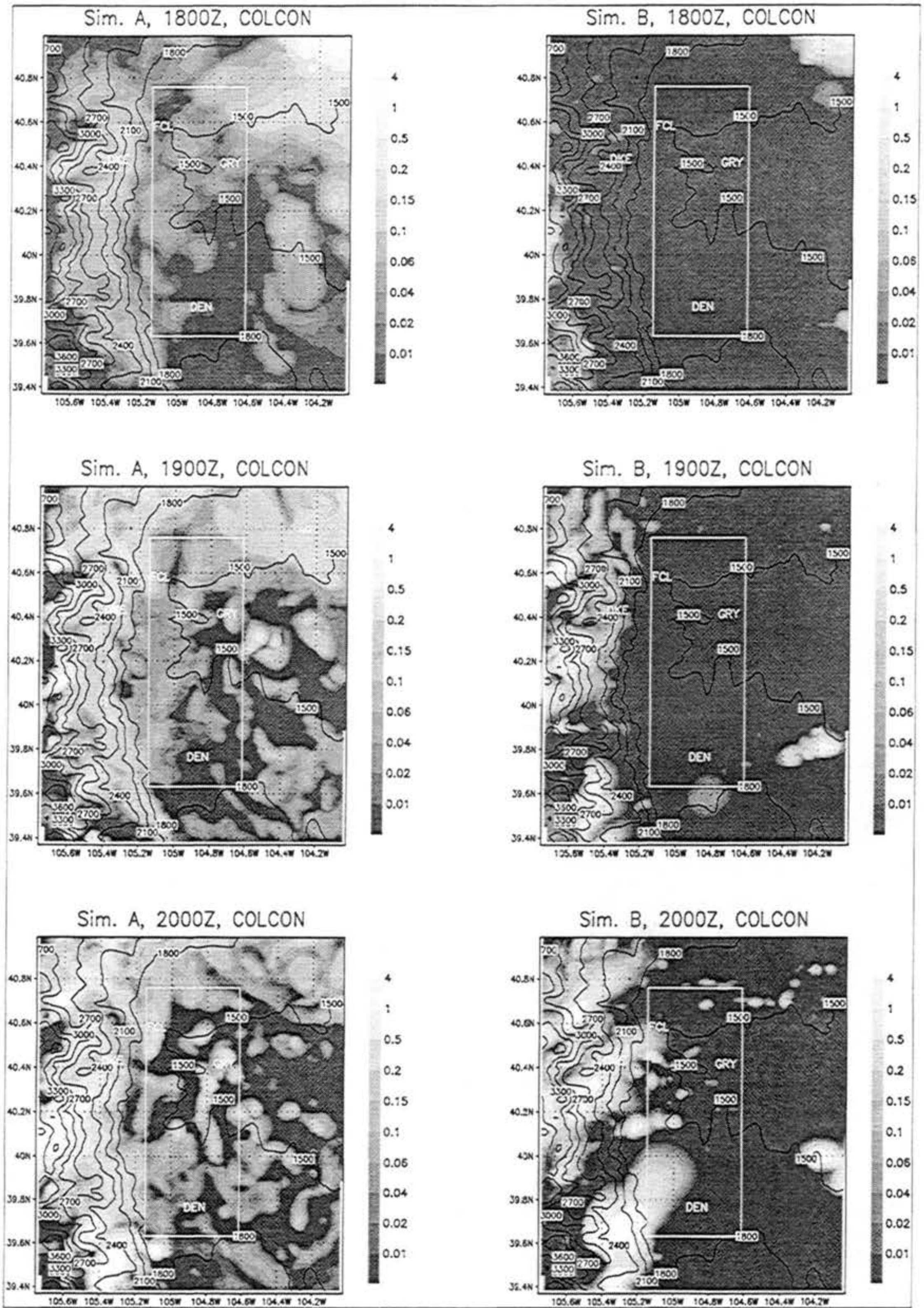


**Figure 6.10** Grid 4 column condensate (kg/m$^2$) for Simulations A and B at 1800Z, 1900Z, and 2000Z. Topography contoured at 300m intervals. Rectangle shows averaging area referenced in text.

We now turn to the issue of the disparate available energy fluxes between simulations. This is immediately explained by the 1800Z-2000Z, column condensate fields shown in Figure 6.10 above. The column condensate field is the vertically integrated condensate mass with units of kg/m$^2$. This plot shows that Simulation B has virtually no cloud cover east of the foothills at 1800Z. In that simulation, clouds are largely restricted to elevations at or above 2100 m (MSL) after 1800Z. This is consistent, qualitatively, with the higher LCL of the upstream, low-level air in Simulation B. One can infer that with reduced cloud cover, Simulation B experiences a greater incident solar radiation at the surface that, again, largely determines the available surface energy flux. This leads one to the following conclusion: In these simulations, not only does soil moisture initialization affect the partitioning of available energy at the surface, but it also influences, to a non-negligible extent, the available surface energy itself, through cloud enhancement or suppression.

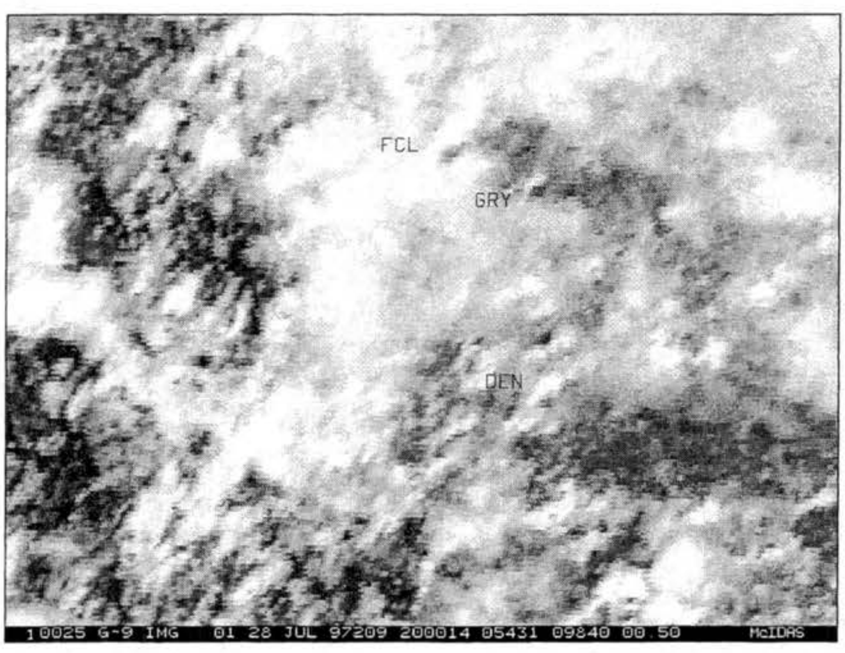


**Figure 6.11** 2000Z July 28 visible satellite image. Fort Collins (FCL), Greeley (GRY) and Denver International Airport (DEN) are also shown.

Figure 6.11 shows the 2000Z visible satellite image over the Front Range. This figure demonstrates that extensive cloud cover existed. The partial clearing to the east of Denver and Greeley is roughly consistent, qualitatively, with the clearing indicated in the column condensate of Simulation A between 1800Z and 2000Z (Figure 6.10). Additionally, the area of enhanced $\theta_e$ seen in Simulation A (Figure 6.9) is also explained by the simulated clearing, and is therefore due to the increase in simulated surface insolation.

The $\theta_e$ evolution in both simulations can thus be summarized in the following way. Theta-e increase in both simulations is driven by available energy input. However, in Simulation B, despite the higher available energy, the smaller evaporation fraction produces a larger sensible heat flux that results in boundary layer growth and entrainment which keeps $\theta_e$ relatively constant after 1800Z. In Simulation A, approximately 90% of the available energy occurs in the form of latent heat flux, resulting in little boundary layer deepening. Theta-e advection, which accounts for ~40% of the 1800Z-2000Z increase over the averaging area in Simulation A, is the result of a mean, along-wind column-condensate gradient. Simulation B lacks cloud coverage over the averaging area, which accounts for the higher available energy in this simulation at and beyond 1800Z.

The evolution of CAPE and the LFC are direct results of the low-level $\theta_e$ evolution. As noted before, the low-level $\theta_e$ uniquely determines the moist adiabat along which a surface parcel ascends after reaching the LCL. As low-level $\theta_e$ increases in Simulation A between 1900Z and 2000Z, the LFC lowers by approximately 800 meters. By 2000Z, both the LCL and the LFC lie well within the flow possessing an upslope component, which extends to approximately 700mb (~3200 m-MSL). In Simulation B, the LCL is at 1569 m-AGL, or ~3100 m-MSL, and the LFC is at ~3500 m-MSL, within the lee-side downslope airflow. The vertical proximity of the LCL to the westerly, downslope flow may be partly responsible for the lack of cloud coverage to the east of the Front Range in Simulation B. The additional positive area, in Simulation A, that results from both the increase in $\theta_e$ and the lowering of the LFC, produces a 2000Z CAPE of 1057 J/kg, significantly higher than the 00Z Denver sounding CAPE of 703 J/kg. In addition, the lowering of the LFC results in a mere 240-m separation between the LCL and the LFC producing very little CIN. For this reason, 2000Z marks the end of the so-called, "pre-storm" evolution. In the next section, the convective evolution of Simulations A and B will be described.

## 6.3 Convective Evolution

### 6.3.1 *2000Z-0000Z, Simulation A precipitation summary*

Having established some of the differences in thermodynamic evolution, we now turn to a description of the precipitation evolution in Simulation A between 2000Z and 0000Z. The precipitation rate for this period is shown in Figure 6.12. For convenience, the storms to be discussed are labeled with Roman numerals. The areas of precipitation that existed at 2000Z over the Front Range continue to exist at 2030Z. At 2030Z, Storm I exhibits a maximum precipitation rate of 10 cm/hr and moves east-northeastward at 8-9 m/s between 2000Z and 2030Z. At the same time, precipitation commences between Fort Collins and Greeley at a rate of 2 cm/hr. These cells, which include Storm II, can be seen in their formative stage in the 2000Z column condensate plot of Figure 6.10 as a

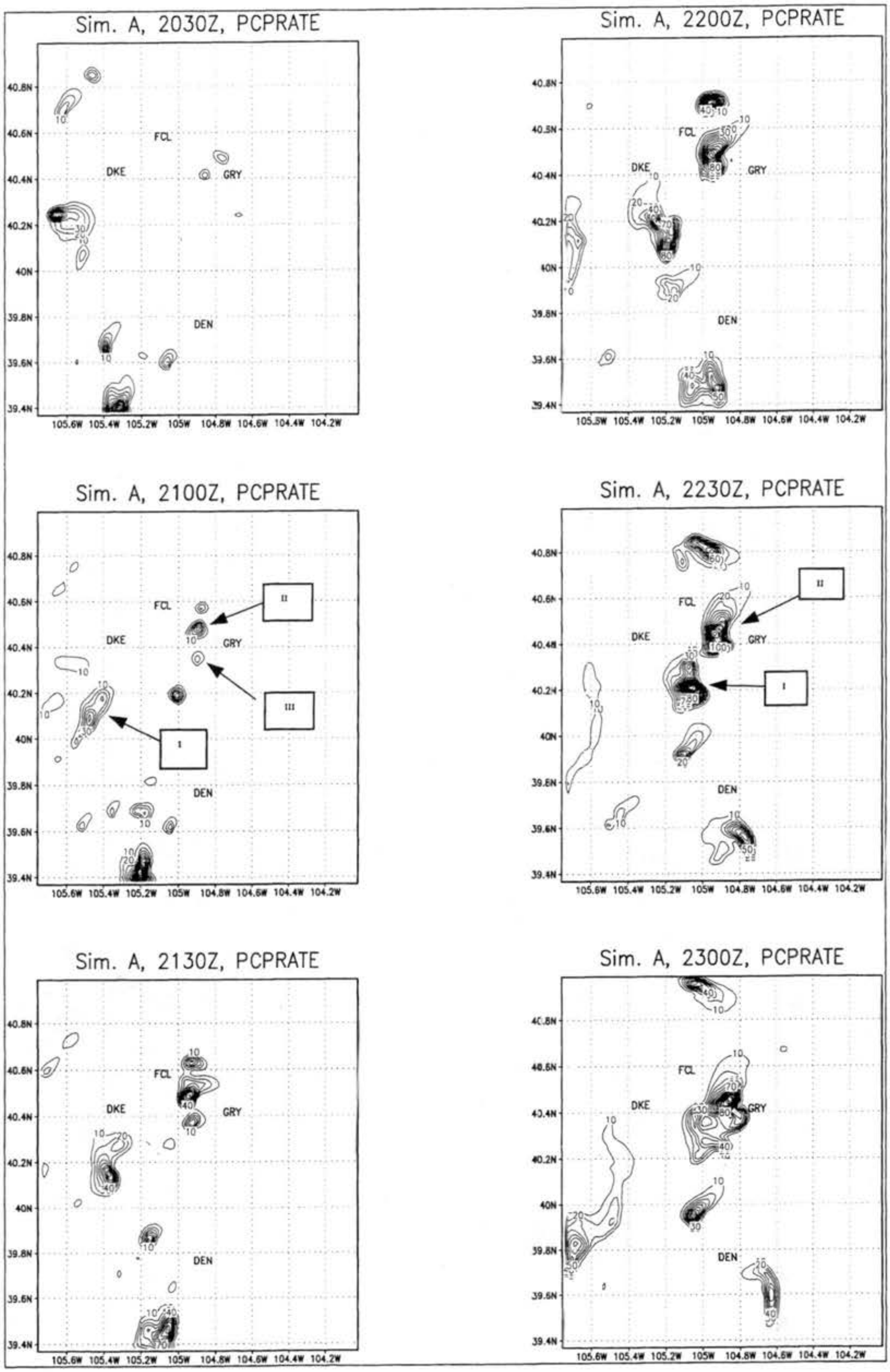


**Figure 6.12** 2000Z-2300Z precipitation rate for Simulations A at half hour intervals. Precipitation rate is contoured at 10 mm/hr intervals. Figure is continued on next page. Storm labels mentioned in text are shown.

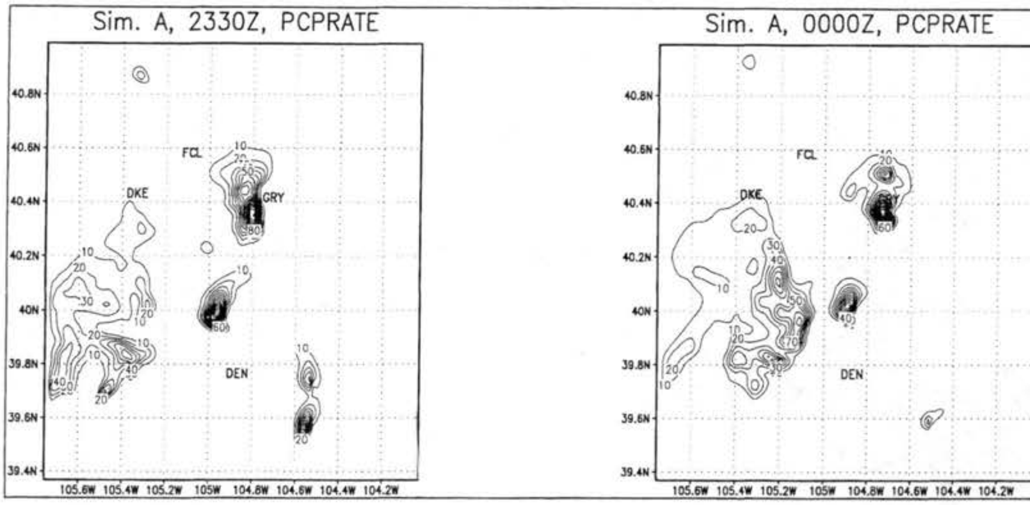


**Figure 6.12 (cont'd).** 2330Z (left) and 0000Z (right) precipitation rate for Simulation A.

south-southwest to north-northeast oriented band of cloudiness. This band forms on the western edge of the enhanced region of $\theta_e$ depicted previously in Figure 6.9, and moves northwestward at 7-8 m/s.

At 2100Z, Storm I possesses a maximum precipitation rate of 6 cm/hr and propagates northeastward at 4-5 m/s. Cells continue to initiate and develop east of the Front Range. At 2100Z, Storm II intensifies and reaches a maximum precipitation rate of 7 cm/hr while it propagates north-northwestward at 4-5 m/s. An additional cell, denoted as Storm III, forms at 2100Z within this line. This storm exhibits a 3 cm/hr maximum precipitation rate. By 2130Z this line of cells takes on a north-south orientation with Storm II achieving a maximum precipitation rate of 12 cm/hr. At this time it is located approximately 20.2 km to the southeast of Fort Collins, and moves southwestward at ~2 m/s. Storm I continues it's northeastward movement at 6-7 m/s with a maximum precipitation rate of 10 cm/hr.

Between 2130Z and 2200Z, precipitation centers II and III merge into a single entity. By 2200Z, Storm II is precipitating at a maximum rate of 14 cm/hr and is quasi-stationary 15.3 km to the southeast of Fort Collins. Storm I possesses a comparable maximum precipitation rate of 13 cm/hr but propagates east-northeastward at 9-10 m/s. At 2230Z Storm II is propagating at 2-3 m/s eastward with a maximum precipitation rate of 16 cm/hr. Hence, the time between 2130Z and 2230Z marks the period in which Storm II reverses its propagation direction. In the intervening one hour, the mean, ground-relative propagation vector is 1.7 m/s to the south. The maximum precipitation rate associated with Storm II occurs at 2245Z (using 15-minute analyses) and is 19 cm/hr. The maximum precipitation rate on Grid 4 does not occur with Storm II, but rather with Storm I, at 2230Z, which possesses a remarkable maximum precipitation rate of 21 cm/hr.

At 2300Z, Storms I and II begin to merge. At this time, Storm I is propagating northeastward at 7-8 m/s with a much-reduced maximum precipitation rate of 6 cm/hr. Storm II moves eastward at 3-4 m/s, with a maximum precipitation rate of 16 cm/hr. By 2330Z, Storm I and II have merged into a single system which then propagates eastward at 1-2 m/s until 0000Z, the final time shown in Figure 6.12. At 2330Z and 0000Z, the maximum precipitation rate of the resulting storm is 18 cm/hr and 19 cm/hr respectively.

The accumulated precipitation distribution is shown in Figure 6.13 below. At 0000Z the domain maximum is 21 cm (8.3 inches) and is located 21.4 km to the southeast of Fort Collins. The domain maximum corresponds to the approximate position of Storm II just before and after its quasi-stationary phase, when the propagation direction of the storm reverses. At the domain maximum, accumulation starts at 2045Z. The maximum precipitation rate experienced at the domain maximum is 16.6 cm/hr and occurs at

2230Z. By 0015Z, the precipitation rate at the domain maximum drops below 1 cm/hr. In the next section, a summary of the Simulation B precipitation evolution is presented.

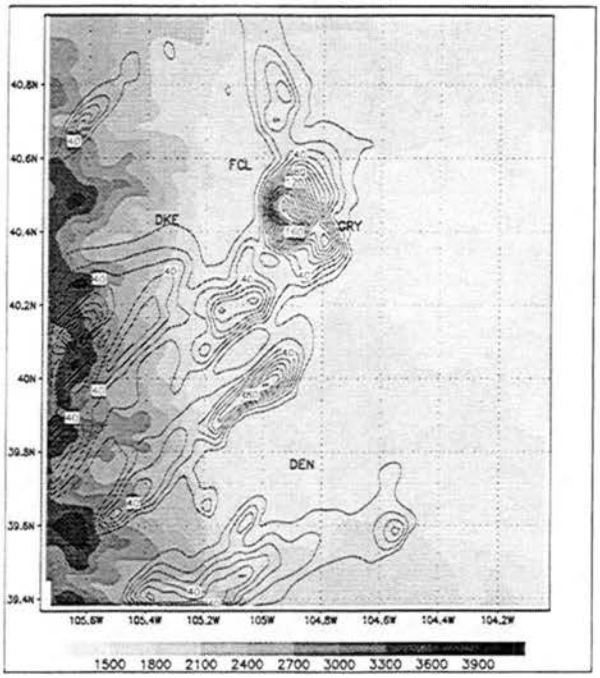


**Figure 6.13** Simulation A, 0000Z July 29, accumulated precipitation. Accumulated precipitation contoured at 10-mm intervals. Topography shaded at 300-m intervals.

### 6.3.2 *2000Z-0000Z, Simulation B precipitation summary*

Figure 6.14 shows the 2000Z-0000Z precipitation rate for Simulation B. Prior to 2030Z, the precipitation evolution was similar between simulations. However, by 2100Z significant differences exist. Unlike Simulation A, no precipitating convection develops between Fort Collins and Greeley until 2200Z. Convection that does develop in that area, after 2200Z, occurs in association with a northeastward-propagating system that initiates over the higher terrain between 1830Z and 1900Z. Secondly, the entire 2000Z-0000Z precipitation evolution is characterized by cell movement to the north and northeast while in Simulation A, propagation-direction reversal and quasi-stationary movement occur.

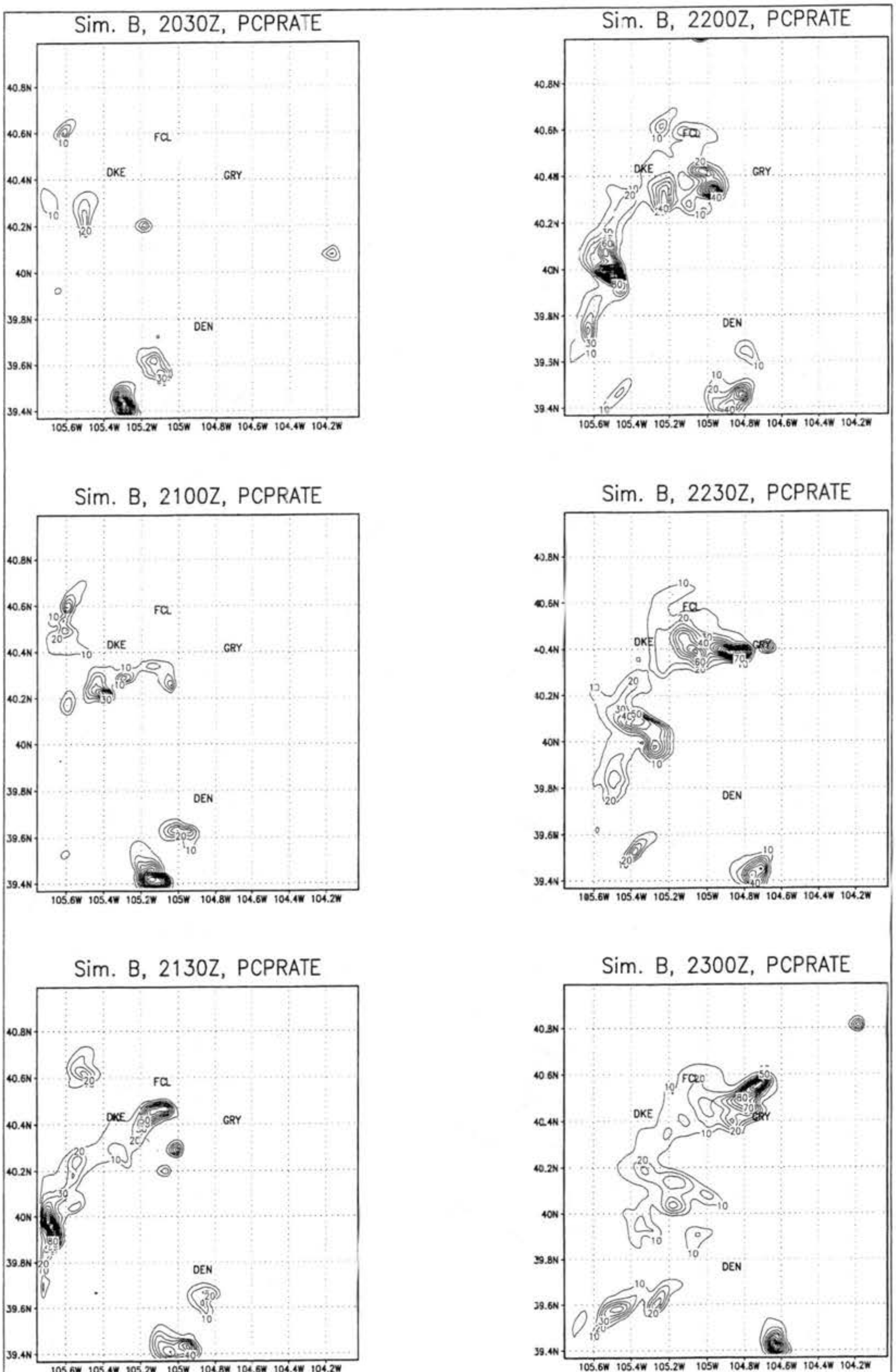


**Figure 6.14** 2000Z-2300Z precipitation rate for Simulation B at half hour intervals. Precipitation rate is contoured at 10 mm/hr intervals. Figure is continued on next page.

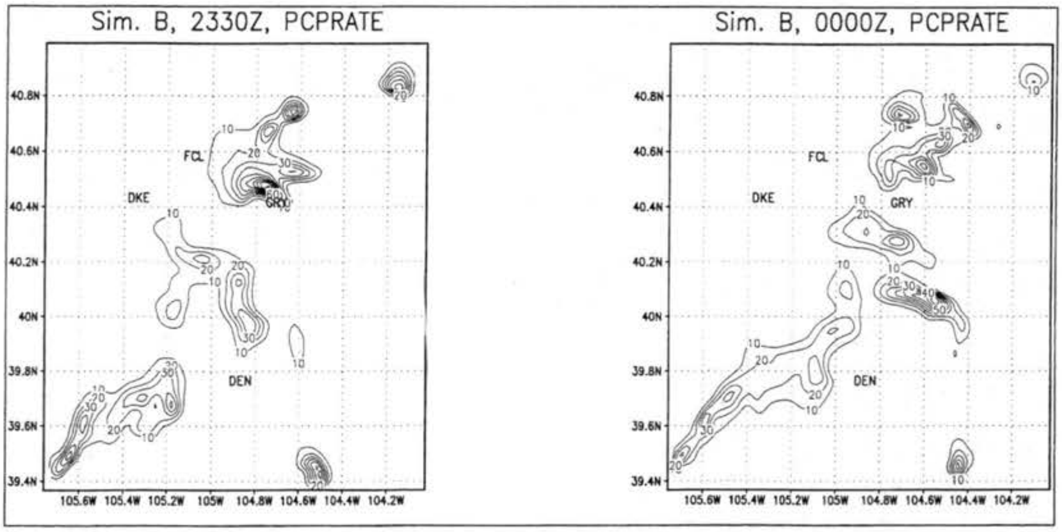


**Figure 6.14 (cont'd)** 2330Z (left) and 0000Z (right) precipitation rate for Simulation B.

Figure 6.15 shows the 0000Z accumulated precipitation for Simulation B. Comparison with that of Simulation A (Figure 6.13) shows that Simulation B produces a more diffuse accumulated precipitation field.

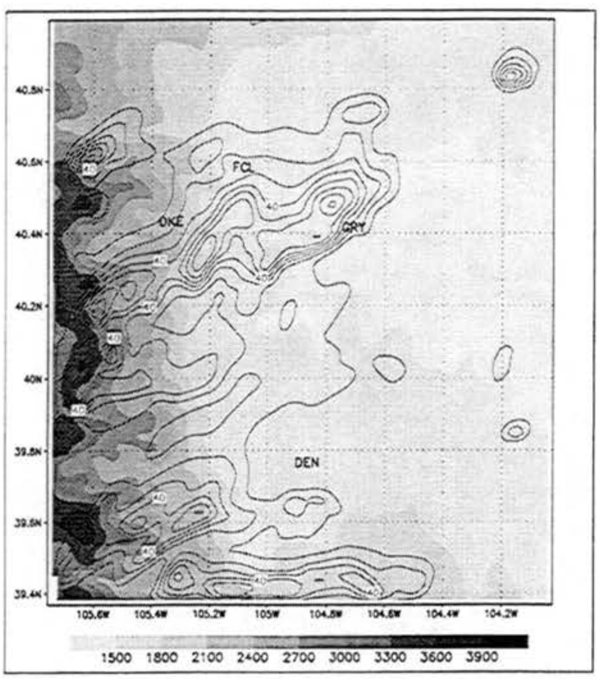


**Figure 6.15** Simulation B, 0000Z July 29 accumulated precipitation for Simulation B. Accumulated precipitation contoured at 10-mm intervals. Topography shaded at 300-m intervals.

Three maxima of 8 cm occur 33 km to the east-southeast of Fort Collins, 28.8 km to the south-southwest of Fort Collins and 59.3 km to the southwest of Fort Collins. These maxima occur in association with the northeastward propagating convective cells depicted in the 2200Z precipitation rate panel at ~(40.4°N, 105°W). Precipitation rates within this system vary between 10 and 14 cm/hr between 2230Z and 0000Z. These rates are comparable to that of Storm II in Simulation A, which ranged from 6 to 19 cm/hr. The more diffuse nature of the accumulated precipitation in Simulation B is largely due to the steady northeastward propagation of the simulated systems.

While the precipitation maximum in Simulation A is produced by continuously propagating storms, those in Simulation B are produced by a system exhibiting multi-cellular characteristics. This is illustrated in Figure 6.16 below, which shows the initiation locations and mean trajectories of the distinct precipitating cells. Here a "cell" is defined in terms of the precipitation rate, as a region of closed 10-mm/hr interval contours that persists for 15 minutes or longer. This definition restricts consideration to those cells exhibiting a significant (≥10mm/hr) precipitation rate. In Figure 6.16, the numerals denote an initiation point, where a closed 10-mm/hr or greater contour first appears. Storms that propagate onto Grid 4 through the western and southern boundary are excluded in the sense that their appearance on the boundary does not constitute an initiation point. The numerals denote the time of initiation with '1' representing the 1800Z-1945Z period, '2' representing the 2000Z-2145Z period, '3' denoting the 2200Z-2345Z period and '4' representing 0000Z. The decay of a cell is defined here as the point at which the definition for cell existence (see above) is no longer met. Given these definitions, the mean propagation path is then defined as the line joining the initiation point and the decay point and these are also shown in Figure 6.16.

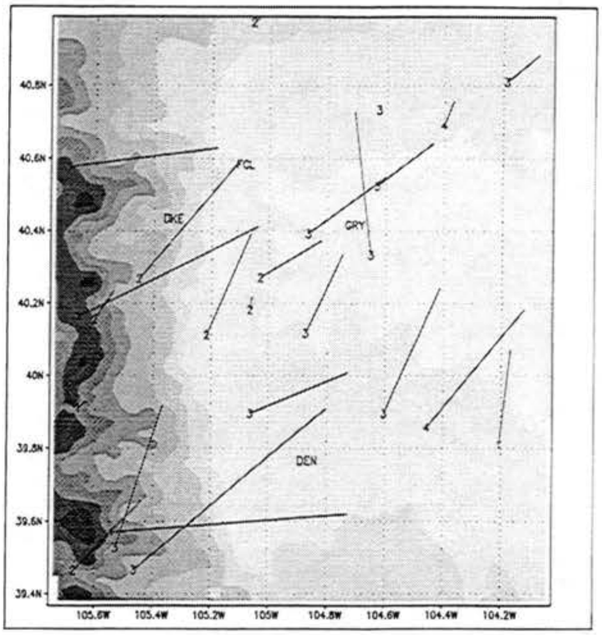


**Figure 6.16** Cell initiation and mean propagation path. '1' indicates initiation between 1800Z and 1945Z, '2' between 2000Z and 2145Z, '3' between 2200Z and 2345Z, and '4' 0000Z. Solid lines indicate mean propagation path. Topography shading is identical to Figure 6.15.

The average lifetime of the 24 tabulated individual cells is 1.55 hours, with a comparable standard deviation of 1.53 hours. Figure 6.16 illustrates that the earliest cells initiate over the higher terrain to the west of Fort Collins and Denver, followed by north-eastward propagation and new cell generation, primarily on the eastern side of the existing cells. When viewed on the time-scale 1900Z-0000Z, an approximate, mean, meso-$\beta$-scale, ground relative system propagation vector can be identified in terms of the time sequence of initiation points in the northern two-thirds of Grid 4 in Figure 6.16. This vector is described by a 106 km displacement, as determined from the high terrain initiation points and the 0000Z initiation points (denoted by the number 4) over a 5 hour period, yielding a 5-6 m/s eastward meso-β-scale propagation vector. Individual cells, however, travel in directions that are primarily north to northeastward at approximately 6-10 m/s. The differing direction and speed of the individual cells relative to the meso-β-scale system propagation vector suggests that some, as of yet unidentified mechanism is acting to control the longer time-scale evolution of the precipitation centers. The next section will consider this issue in greater depth.

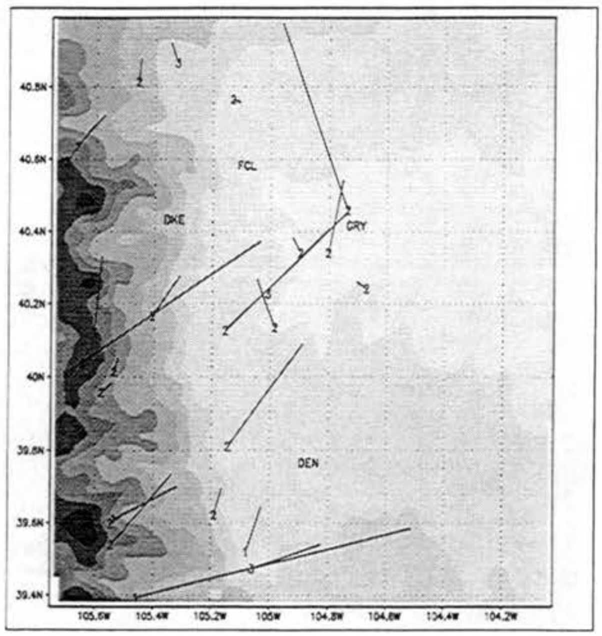


**Figure 6.17** Same as Figure 6.16 except for Simulation A.

A similar analysis, shown in Figure 6.17, was performed for Simulation A. This figure shows that a greater proportion of the cells initiate during period-'2', that is between 2000Z and 2145Z than in Simulation B. Simulation B produces only one cell with a mean propagation path having a westward component. In contrast, Simulation A produces five such cells out of a total of 25 identified cells in that simulation. The increased percentage of westward propagating cells may be related to the previously discussed point that both the 2000Z LCL and LFC lie well within the easterly low-level airflow just east of the Front Range foothills, while in Simulation B, the LCL lies just below the westerly airflow and the LFC lies within the westerly-component flow. The average lifetime of individual cells in Simulation A is 1.57 hours, which is comparable to those in Simulation B. However, while both simulations place a majority of the period-'1' initiation sites over the higher terrain, only Simulation B demonstrates a clear trend for subsequent cells to systematically develop eastward in time.

In summary, the primary differences in precipitation evolution between simulations, includes the following. Firstly, the domain maximum in Simulation A is produced by a system that is largely characterized by continuous propagation, the exception being the merging of Storms I and II at 2315Z. Simulation B exhibits discrete propagation with individual cells travelling north-northeastward at 6-10 m/s and a meso-$\beta$ spatial scale, 5-hour time-scale, system propagation vector of 5-6 m/s eastward. The larger domain maximum in Simulation A and the more diffuse pattern in Simulation B are largely the result of fundamentally different propagation characteristics. Simulation A produces a reversal in propagation direction in Storm II along with a nearly quasi-stationary property between 2130Z and 2230Z, while Simulation B storms exhibit neither direction-reversal, nor quasi-stationary propagation. Simulation A produces 21-cm of precipitation by 0000Z, roughly 5-cm less than the Fort Collins storm total. However, as will be seen shortly, another 5-cm falls over the domain maximum between 0000Z and 0230Z. Simulation B produces domain maxima between Fort Collins and Greeley that are approximately 18-cm lower than the extreme amount observed in Fort Collins. In the next section, we will examine a likely physical mechanism for the differing propagation characteristics.

### 6.3.3 *Cold-pool characteristics*

Figure 6.18 is presented to motivate the analysis in this section.

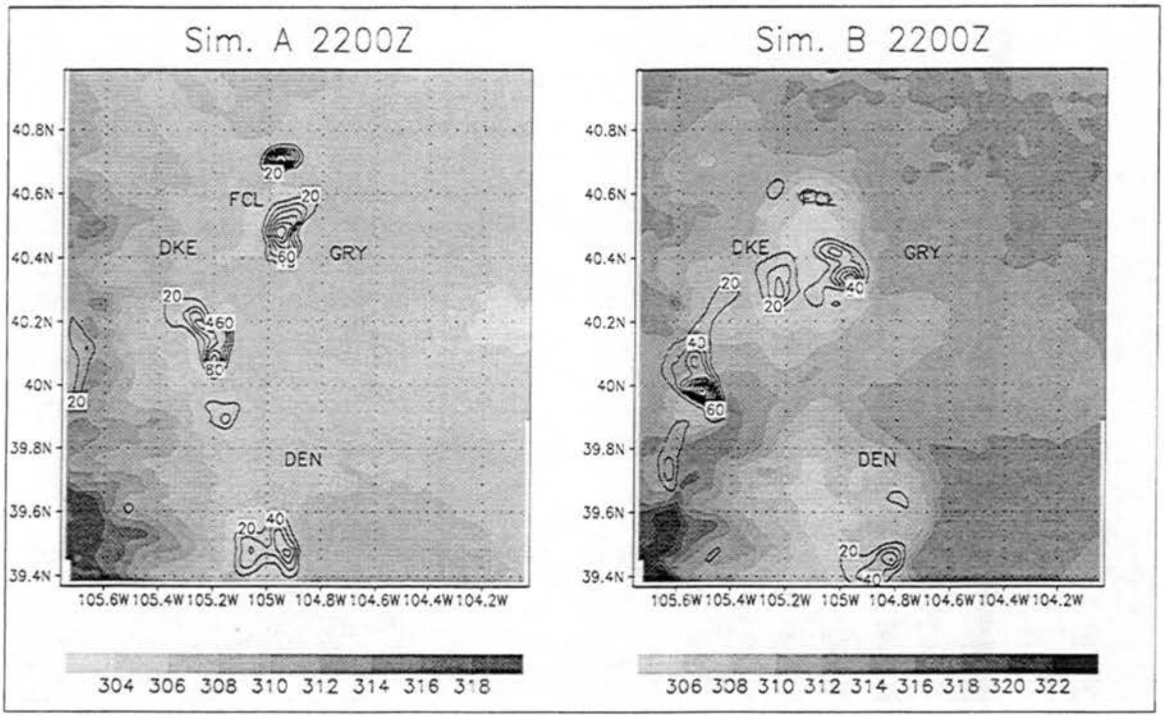


**Figure 6.18** Surface potential temperature (shaded) and precipitation rate (contoured) at 2200Z for Simulations A (left) and B (right). Potential temperature shaded at 2K intervals, with identical shading scale between panels. Precipitation rate contoured at 20-mm/hr intervals.

This figure shows the surface potential temperature and precipitation rate for Simulations A and B at 2200Z. In Simulation A, Storm II is located between Fort Collins and Greeley and is quasi-stationary. In association with Storm II is a cold-pool which has spread approximately 10-km to the north and west of the storm center and which is approximately 4K colder than the surrounding environment. Simulation B also produces cold-pools associated with the areas of precipitation in that simulation. However, in Simulation B, the cold-pools extend over a significantly larger area and exhibit typical potential temperature deficits of approximately 10K. The goal in this section is to provide a quantitative measure of the cold-pool properties and to relate these properties to the cold-pool movement.

The reason for this undertaking is the previously noted eastward movement of the cell initiation points in Simulation B. As Figure 6.18 illustrates, at least for 2200Z, there is a tendency for cells to exist along the eastern or windward edge of the cold-pool boundaries, presumably due to increased low-level convergence along these boundaries. This begs the issue of whether or not the cold-pool propagation in Simulations A and B plays a role in determining storm motion and the evolution of cell initiation points in time. More specifically, are the cold-pool properties in Simulation B conducive to an increased system propagation speed, relative to Simulation A, thereby partially explaining the more diffuse precipitation pattern in Simulation B?

Firstly, it must be understood that the choice of quantitative parameter used to characterize the cold-pool "strength" must ultimately relate to the ground-relative propagation speed of the cold-pool. A reasonable choice for this parameter is the classical propagation speed for a two-dimensional density current in a shearless basic-state flow:

$$c^2 \equiv -2g \cdot \int_0^H \frac{\theta'}{\theta_0(z)} dz \, . \tag{6.5}$$

Here, $c$ is the propagation speed relative to the undisturbed environmental airflow, $g$ is the gravitational acceleration, $\theta_0(z)$ is the environmental potential temperature profile, and $\theta'$ is the perturbation potential temperature within the cold pool. The integration is performed vertically from the surface to the top of the cold-pool, $H$, above which $\theta'$ is assumed to be negligible. (Rotunno et. al., 1988, hereafter referred to as RKW.)

RKW developed a more comprehensive expression for the ground-relative propagation speed in a sheared environment with a rigid-lid upper-boundary condition, but which contained an undetermined parameter, $\beta$, which related the inflow and outflow wind velocities at the rigid-lid upper boundary. Barriers to applying this expanded theory to the present situation arise from the arbitrariness in selecting the level for the rigid-lid upper boundary — a complication which stems from the existence of a convective plume in the area of interest in these simulations. Secondly, the choice of this level, in a sheared environment can significantly alter the *shear* modification to the solution. Because of the arbitrariness in selecting this level in the present situation, there seems little point in including the shear effect. In addition, the effects of latent heating above and near the cold pool, due to active convection is also not considered in Equation 6.5. Given this, $c^2$, as determined in the analysis to follow, will not be used as and should not be interpreted as a test or validation of the classical formula for steady-state, two-dimensional density current propagation, since very few of the assumptions in that theory can be said to be satisfied exactly by the system being simulated. Rather, it is simply a convenient parameter choice, which we anticipate may be related to the simulated cold-pool motion in these simulations.

The method used to compute $c$ is as follows. Firstly, the cold-pool is identified by examination of the surface potential temperature field. An example is shown in Figure 6.19 below. The horizontal position corresponding to the minimum surface potential temperature is identified and denoted as the central minimum. The central minima for each simulation at 2230Z are marked with crosshairs in Figure 6.19. The potential temperature profile at the central minimum is used to compute the potential temperature perturbation, $\theta'$.

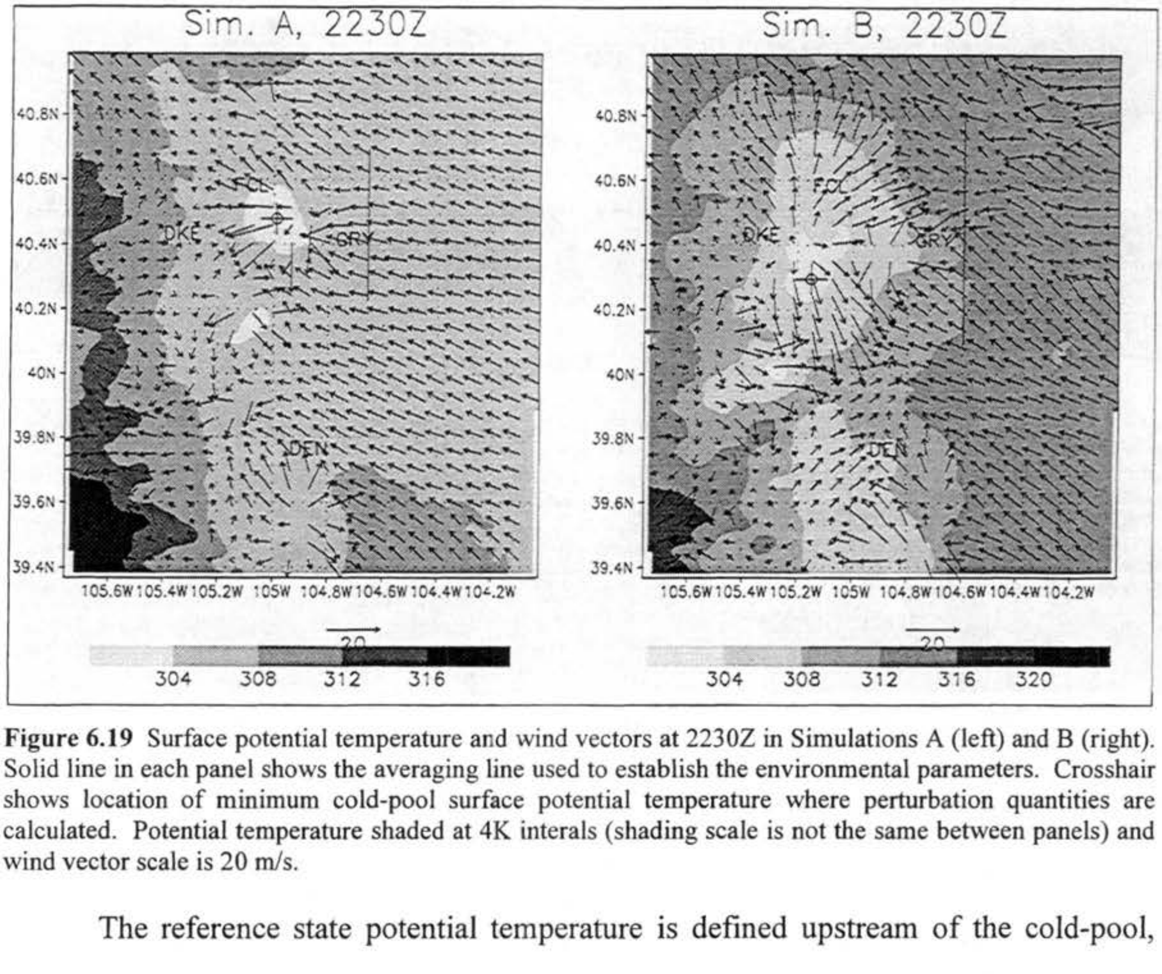


**Figure 6.19** Surface potential temperature and wind vectors at 2230Z in Simulations A (left) and B (right). Solid line in each panel shows the averaging line used to establish the environmental parameters. Crosshair shows location of minimum cold-pool surface potential temperature where perturbation quantities are calculated. Potential temperature shaded at 4K interals (shading scale is not the same between panels) and wind vector scale is 20 m/s.

The reference state potential temperature is defined upstream of the cold-pool, with sufficient distance from the cold-pool to be representative of the impinging air properties. The environmental quantities are defined using the line-average along the north-south oriented lines shown in Figure 6.19. Using the perturbation potential temperature and the reference-state potential temperature thus defined, the quantity $-\dfrac{\theta'}{\theta_0}$ is computed at each grid-point in the vertical. The surface value of this quantity is obtained by extrapolation since the vertical Cartesian levels do not always correspond with the underlying topography. The cold-pool top, where $\frac{\theta'}{\theta_0} = 0$, is obtained by linear interpolation. This fractional perturbation is then averaged to the center of each vertical interval. Finally, the quantity $c^2$ is obtained by a Riemann sum approximation to the integral in Equation 6.5.

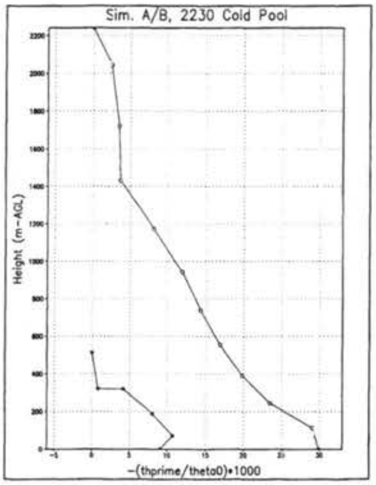


**Figure 6.20** Plot of $\left( -\frac{\theta'}{\theta_0} \cdot 10^3 \right)$ vs. height (m-AGL) at 2230Z for Simulations A (solid circles) and B (open circles).

Profiles of $-\frac{\theta'}{\theta_0}$, corresponding to the time depicted in Figure 6.19 (2230Z), are shown in Figure 6.20. This figure illustrates two major differences in the cold-pool properties, between simulations. Firstly, the cold-pool in Simulation B exhibits greater negative buoyancy at every level by a factor of three to five. Secondly, the cold-pool depths are significantly different with Simulation A exhibiting a depth of ~520-m compared to ~2240-m in Simulation B. The cold-pool depth in Simulation A is approximately that of the 2000Z LCL (590-m) in Table 6.2, suggesting that evaporative cooling, due to precipitation falling below cloud-base, could be a major contributor to the cold-pool negative temperature perturbation. In Simulation B, the cold-pool depth of 2240-m is ~670-m higher than the 2000Z LCL in Table 6.2. This may be due to moist-adiabatic descent of low $\theta_e$ air from prior or proximate downdrafts, or may be due to evaporative cooling of precipitation falling from elevated cloud-masses surrounding the precipitation cores. At any rate, the deeper cold-pool in Simulation B is consistent with the higher LCL in Simulation B which allows for a greater depth of the sub-cloud air to be cooled by the evaporation of falling precipitation. An alternative explanation for the increased depth relates not to the sub-cloud temperature profile, but to that of the environment. Even if the sub-cloud and in-cloud temperature profiles were identical between simulations, we know that the environmental temperature profiles are not. Simulation B possesses a warmer and deeper boundary layer than does Simulation A. This alone would produce a deeper cold pool since, here, by definition the cold pool extends up to the point where $\theta' = 0$. For example, it is true that at 2230Z, the computed cold-pool minima potential temperature profiles in each simulation are within ~1K of each other at each level. However, the environmental potential temperature profiles differ by as much as 7K, with Simulation B being warmer until, at approximately 2.2-2.4 km (AGL), the profiles return to within 1K of each other.

The average cold-pool depth, time-averaged from 15-minute analyses between 2100Z and 2300Z, is 646-m in Simulation A, and 2388-m in Simulation B. The maximum near-surface cold-pool potential temperature deficit during this period is ~4K in Simulation A and ~9.5K in Simulation B. Referring back to Equation 6.2, we see that the steady state propagation speed, $c$, will be larger in Simulation B due to both the larger-negative buoyancy values and the greater cold-pool depth attained in that simulation. Figure 6.21 shows the computed $c$ values as a function of time for both simulations.

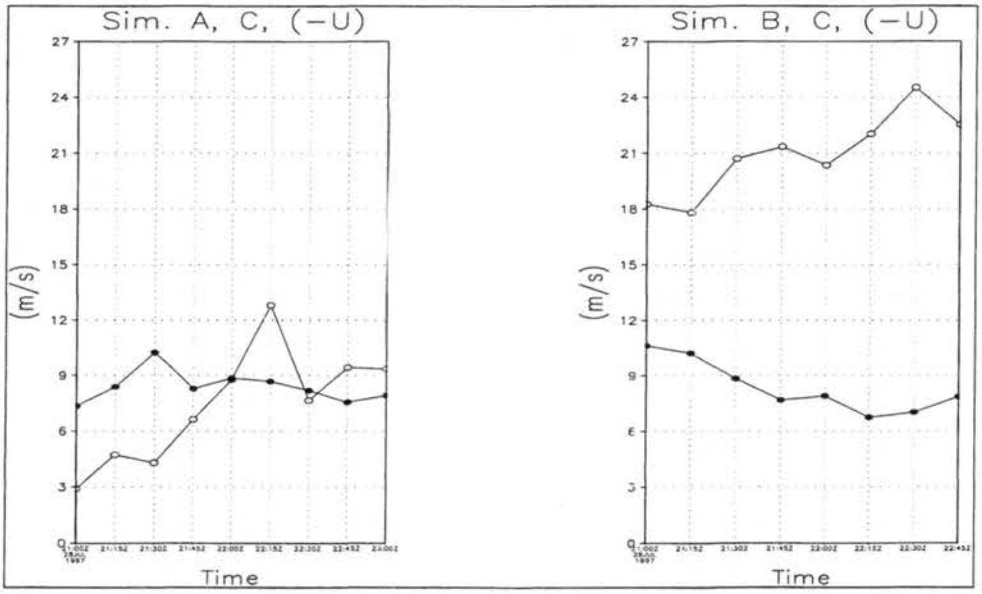


**Figure 6.21** Propagation speed (c) (open circles) relative to the ambient, 200-m average zonal wind-speed (-U) (solid circles), as a function of time in Simulations A and B.

In this plot, $c$ is compared to the low-level, environmental zonal wind magnitude. The low-level environmental zonal wind is simply the vertical average over the lowest 200-m, of the line-averaged environmental profile. Both simulations, as expected, show $c$ increasing with time as the respective cold-pools strengthen. In Simulation A, $c$ ranges from 3 m/s at 2100Z to 13 m/s at 2215Z. In Simulation B, $c$ ranges from 17 m/s to 24.5 m/s. Comparison to the environmental upstream zonal velocity magnitude shows that Simulation B always produces a $c$ that is greater than the impinging wind. Likewise, the cold-pool in Simulation B is always found to always propagate eastward. The same comparison in Simulation A shows that during the period 2100Z-2200Z, $c$ is less than the zonal wind magnitude and it is during this time that Storm II, propagates westward. After 2200Z, $c$ is larger than the zonal wind magnitude and after 2200Z, Storm II propagates eastward, against the impinging easterly flow. This would suggest that the reversal of propagation direction in Storm II is due to the increasing cold-pool strength, and that the difference in propagation characteristics between Simulations A and B may be largely due to the differing cold-pool properties. It should be noted however, that the ground relative propagation speed predicted by the difference between the environmental low-level wind and the steady state propagation speed, *c*, is significantly over-predicted in Simulation B. The mean ground-relative propagation speed actually simulated is ~5-6 m/s, while Figure 6.21 predicts 8-17 m/s. Hence, it is clear that the simple steady-state two-dimensional theory is an over-simplification for the current simulations. This is not surprising as these simulations are not characterized by steady state solutions, the flow is three-dimensional, the environment is sheared, and heat sources and sinks are abundant near the cold pool. However, the difference in storm propagation characteristics between simulations, does agree qualitatively, with the cold-pool propagation difference between simulations. Other factors, such as the vertical extent of the convective plume within the sheared flow and the distribution of latent heating within the updraft are likely to have an impact on storm movement (Moncrieff and Green, 1972) as well. The effects of shear, environmental hydrostatic stability and latent heating on storm steering level and cold-pool propagation were examined by Liu and Moncrieff (1996) for two-dimensional flow, but this was not pursued in this thesis.

### 6.3.4 *Cold-pool source and storm structure*

As was apparent in the previous section, the storms in Simulations A and B produce cold-pools, which, by definition, are negative perturbations in the *dry* potential temperature. A possible explanation was proposed in which the negative potential temperature perturbation was partially due to evaporative cooling below cloud-base and this was partly justified by the coarse correspondence between the cold-pool depth and the LCL. Now we investigate the cold-pool source in Simulation A in more detail, but to do so, we must examine the storm structure. Figure 6.22 shows the vertical velocity on the z=2311 m (MSL) ≅ 800 m (AGL), Cartesian surface at 2200Z.

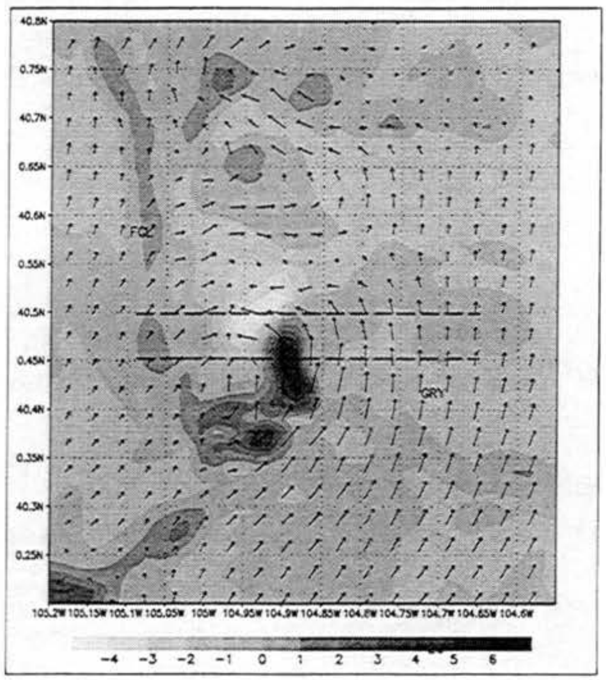


**Figure 6.22** Vertical velocity (shaded) at z=2311m (MSL) and horizontal velocity vectors at z=3981m (MSL) at 2200Z. Vertical velocity shaded at 1-m/s intervals. Horizontal velocity scale is 20-m/s. Dashed lines show transects used in Figure 6.23.

The vertical velocity field shows the updraft and downdraft associated with Storm II in Simulation A. As a reminder, this time corresponds to the stage when Storm II is quasi-stationary 15.3-km to the southeast of Fort Collins. The maximum precipitation rate at this time, which occurs in the downdraft region (light shading), is 14 cm/hr. The cold-pool potential temperature perturbation at the surface is between -2.5 and -3.5 K. The horizontal velocity vectors in this figure are *not* defined on the same surface but are those on the z=3981m (MSL) ≅ 2400m (AGL) surface. These will be discussed shortly. The vertical velocity field shows that the main updraft exists on the eastern side of the system with the downdraft located 5-6 km to the northwest.

The dashed lines in this figure show the transect locations, along which storm cross-sections were taken. The cross-sections taken along the northern and southern transects will hereafter be referred to as the "downdraft-" and "updraft-" cross-sections respectively. Before proceeding to the cross-sections it is important to note that this storm is not completely sampled in either transect due to the storm tilt. Examination of the vertical extent of the vertical velocity field (not shown) shows that the updraft ceases to exist between model-levels 30 and 31 which corresponds to 14.7-15.5 km (MSL). Secondly, the latitude and longitude of the vertical velocity maximum at model-level 30 occurs at (40.5174°N, 104.863°W), while the precipitation rate maximum occurs at (40.4785°N, 104.953°W). This corresponds to a displacement of 8.75 km to the northeast, of the storm top relative to the precipitation core. One will recall, from Section 3.2.3, that the Cheyenne NEXRAD radar detected the storm-top, to be located vertically between 13.5-15.5 km (MSL), and 8-10 km horizontally to the northeast of the precipitation core. Hence, the simulated storm tilt and height is consistent with observations of the Fort Collins storm itself.

Figure 6.23 below shows the updraft- and downdraft cross-sections with streamlines and shaded vertical velocity. The updraft cross-section only samples the portion of the updraft below approximately 7-km (MSL) as the updraft tilts north of the updraft transect above this altitude.

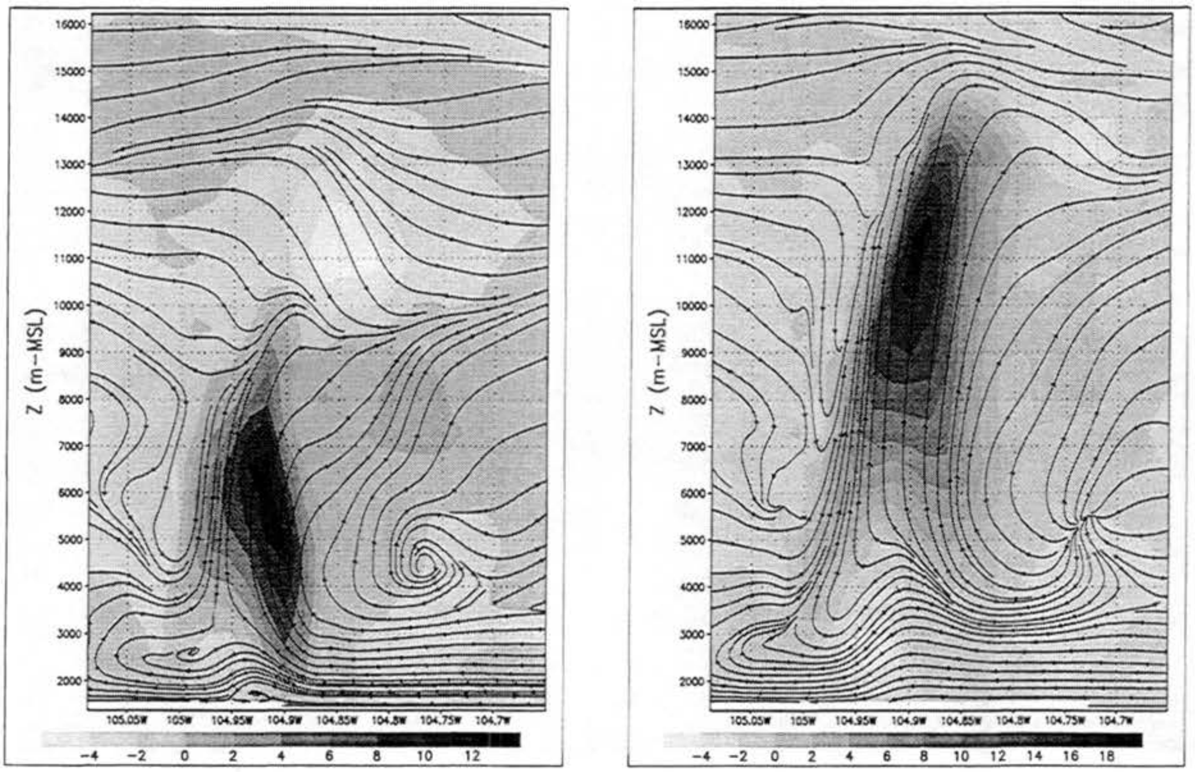


**Figure 6.23** Storm I updraft (left) and downdraft (right) cross-sections at 2200Z. Streamlines are solid lines with arrows and vertical velocity field is shaded at 2-m/s intervals.

The left panel shows an updraft with maximum vertical velocity between 12 and 14 m/s (27-31 mph). The base of the updraft is located at ~2300 m (MSL) ≅ 800 m (AGL) and at 104.88°W. This horizontal position corresponds to the eastern edge of the cold pool shown earlier in Figure 6.18. Inflow air at 2000 m (MSL) flows up and over the southeastern edge of the cold-pool and then enters the incompletely sampled downdraft at 104.97°W. An overturning circulation can be seen to the east of the main-updraft at ~4200m. The right-panel of Figure 6.23 shows the downdraft cross-section. This figure samples the main downdraft and the upper-portion of the storm updraft, which tilts into the downdraft transect from the south around 7-km (MSL) altitude. The maximum vertical velocity is ~19 m/s (43mph) at z=11 km (MSL). The downdraft, being more completely sampled in this transect reaches a maximum descent rate of ~-4 to -6 m/s (9-13 mph) at approximately 2800-m (MSL) ≅ 1300-m (AGL). Two updraft branches are evident on the eastern and western sided of the storm system with the downdraft splitting these branches below 4.2-km (MSL). Again, an overturning circulation is evident to the east of the system but is located at 5.5 km (MSL) in this cross-section. Storm II, at 2200Z, is therefore characterized by an updraft which tilts to the northwest below 5.5 km (MSL) and to the northeast above 5.5 km (MSL) with the primary downdraft located to the northwest of the primary updraft. The updraft cross-section samples the low-level updraft and the southern portion of the cold-pool, while the downdraft cross-section samples the upper-level updraft and the primary downdraft.

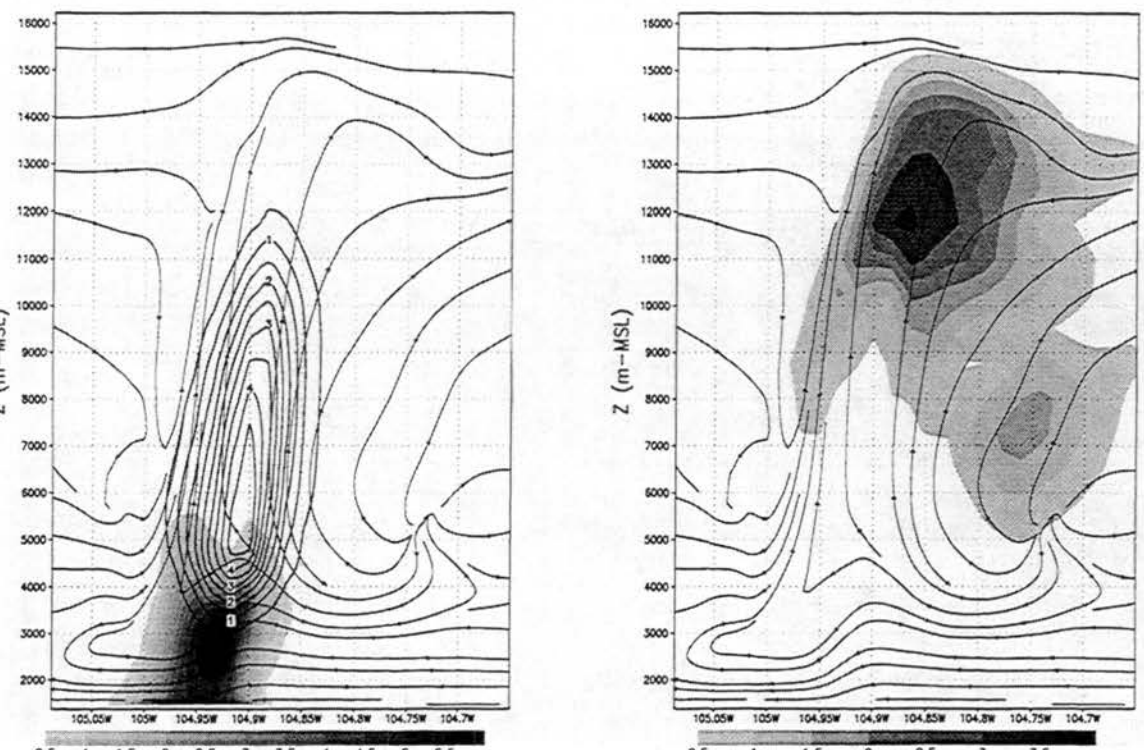


**Figure 6.24** Downdraft cross-sections showing rain and hail mixing ratios (left), shaded and contoured respectively at 0.5 g/kg intervals. Right panel shows the sum of graupel, snow, aggregates and pristine ice mixing ratios, shaded at 0.5 g/kg intervals.

Figure 6.24 shows the microphysical variables for the downdraft cross-section. This figure shows that the rain mixing ratio maximum exceeds 5.5 g/kg between 2200-m and 3400-m (MSL). This rain shaft lies directly beneath a northeastward tilting hailshaft that extends to approximately 12-km (MSL) and which exhibits a comparable mixing ratio maximum, exceeding 5 g/kg. The in-cloud freezing level lies between 4900-m and 5100-m (MSL). As one would expect, the hail and rain-mixing ratio gradients overlap below the freezing level. The similarity in the maximum hail and rain mixing ratios indicates that much of the rainfall is supplied from hail falling and melting below the freezing level.

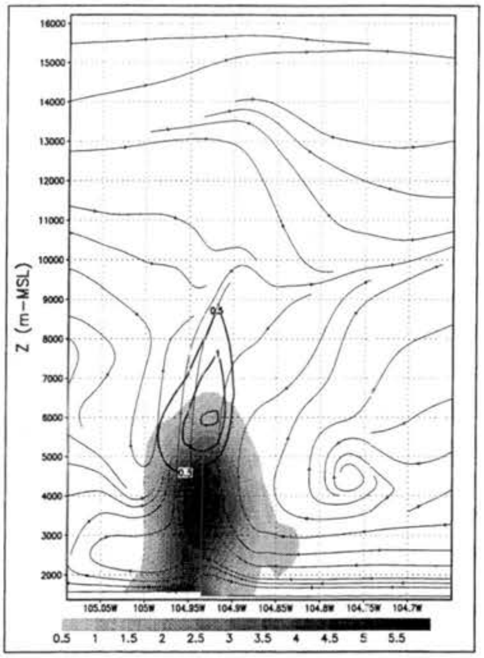


**Figure 6.25** Updraft cross-section at 2200Z in Simulation A. Rain mixing ratio shaded at 0.5 g/kg-intervals; hail mixing ratio contoured at 0.5-g/kg intervals.

Figure 6.25 shows the rain and hail mixing ratios in the updraft cross-section. The primary differences between the updraft microphysical configuration and that of the downdraft cross-section are the following. Firstly, the maximum rain-mixing ratio is centered at 4 km in the updraft cross-section, as opposed to 2.5 km in the down-draft cross-section. Secondly, rain-mixing ratios greater than 0.5 extend all the way up to 6.6

km, approximately 1.2 km above the in-cloud freezing level which is at ~5.4 km within the updraft cross-section. This would suggest that in the updraft cross-section, the rain species is being launched above the freezing level leading to supercooled raindrops followed by a transition to the hail category through freezing (See Walko et. al., 1995 for an explanation of the category transitions). In the downdraft cross-section, the rain mixing ratio barely extends above the 5 km freezing level, and does so only within the two ascending branches that surround the downdraft. In that same cross-section the hail shaft extends down to 3-km, well below the freezing level. Hence a possible scenario which would explain the differences in microphysical species concentrations between the two cross-sections is one in which raindrops are carried above the freezing level within the low/mid-level updraft followed by freezing to form hail, with a subsequent descent within the downdraft and complete melting constituting the majority of the rain shaft. This is also consistent with the scenario proposed by (Petersen et. al., 1999) (Section 7c) in which raindrops were lofted above the freezing level, underwent freezing and accretional growth followed by descent in the downdraft to the northwest of the updraft. Secondly, it should be noted that there is no accumulated hail precipitation at the surface from this simulated storm. This is also consistent with observations as no hail was observed in association with the Fort Collins storm (Petersen et. al., 1999) (Section 8). The right-panel in Figure 6.24 (downdraft) shows the summed mixing ratios of the intermediate and low-density species: graupel, snow, aggregates, and pristine ice. Being lower density frozen particles with typically smaller terminal velocities, these species are found almost exclusively above the freezing level in the upper portion of the primary updraft and on the ascending, western edge of the overturning circulation to the east of the primary updraft.

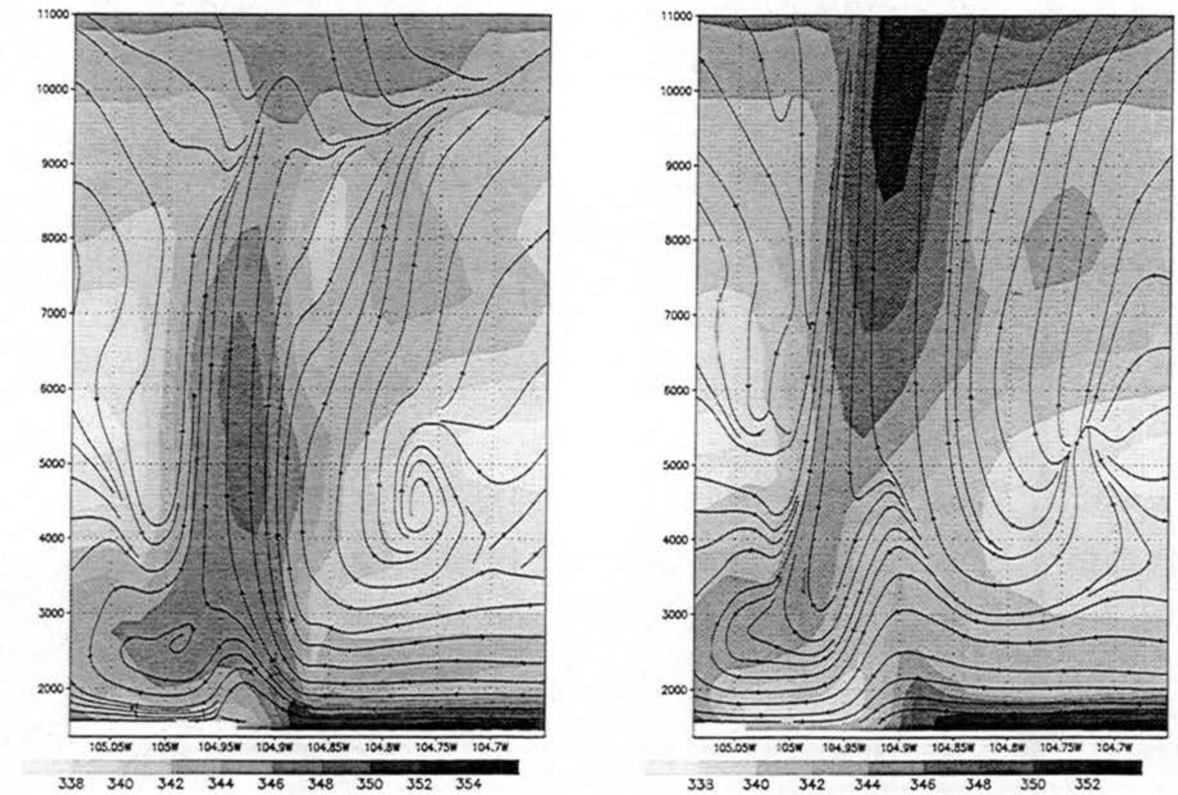


**Figure 6.26** Updraft and downdraft cross-sections for Storm II at 2230Z, with streamlines (solid). $\theta_e$ shaded at 2K intervals. Vertical axis is height (m-MSL).

Now that the storm structure has been clarified, we turn to the issue of the cold-pool source air. Figure 6.26 shows the familiar streamline pattern for the updraft and downdraft cross-sections with a shaded $\theta_e$ field superimposed. Recall that $\theta_e$ is conserved following a parcel if evaporation and condensation from vapor to liquid is the only source of diabatic heating. Mixing processes and melting/freezing of condensate act to change $\theta_e$. The vertical scale in this plot is not identical to previous plots and only extends to 11-km (MSL). The left panel (updraft cross-section) clearly shows the updraft, the low-level inflow and the head of the cold-pool, which is located at 104.92°W. The updraft is flanked on both sides by regions of minimum $\theta_e$. This $\theta_e$ minimum, in the pre-storm environment was located at approximately 5-km (MSL). Some of this lower $\theta_e$ air mixes with the updraft between 2000-m and 3500-m, thereby reducing the updraft $\theta_e$. The maximum $\theta_e$ within the updraft between 4 and 7 km is likely due to the latent heat of freezing. The surface cold-pool in the updraft cross-section is partly due to southward advection from that in the downdraft cross-section. The downdraft cross-section shows a different $\theta_e$ configuration. As noted earlier, this cross-section only intersects the primary updraft above approximately 7-km. Again, the cold-pool is evident with its eastern boundary at 104.92°W. The fact that the cold-pool can be identified in this plot as a low-$\theta_e$ region suggests that either the cold-pool source air is not entirely of surface origin, or that the melting of frozen precipitation within the downdraft significantly lowers the cold-pool $\theta_e$. In fact, the relative continuity of the 340-342K $\theta_e$ region within the cold-pool and extending to the $\theta_e$ minimum at 4-5 km (MSL) to the east of the storm indicates that the cold-pool source air originates above the boundary layer to the east of the storm system. Figure 6.22, which was used to show the transect geometry, also shows the horizontal wind at 3981-m (MSL) superimposed on the 2311-m vertical velocity. This figure shows that in fact, at ~4 km (MSL) predominantly easterly winds penetrate the downdraft region. Hence the storm structure, in addition to that already noted, consists also of an easterly stream of air which undercuts the northwest/east tilting updraft between 3 and 4-km (MSL) on its northern side, intercepts the hail and rain shafts and descends at near saturation within the downdraft, to form the cold-pool. This cold-pool then spreads southward toward the low-level updraft where it can be seen lifting the high-$\theta_e$ easterly inflow in the left panel of Figure 6.26. It is also likely that the melting of hail at the top of the downdraft and mixing processes near the cold-pool boundary and updraft play a role in modulating $\theta_e$ as well.

The same analysis was attempted for the storms between Fort Collins and Greeley in Simulation B between 2200 and 2300Z. However, due to the transient nature of the cells, their rapid movement, the limitations of cross-section views, etc., it was nearly impossible to conclusively identify the cold-pool source air. It was noted that areas of cool $\theta_e$ tended to form within the downdrafts where there was also a strong hail mixing ratio gradient, suggesting that the melting of hail may have played a significant role in changing $\theta_e$ (Knupp, 1987). Additionally the environmental $\theta_e$ minimum would often flow rearward over an advancing cold pool followed by cell initiation in such a way that a pocket of low-$\theta_e$ air would be trapped to the west of the developing updraft and be absorbed into the developing downdraft. As in Simulation A, comparable hail and rain mixing ratios (5.0-7.5 g/kg) often lied directly above and below each other and yet no precipitation at the ground occured in the form of hail east of the Front Range foothills.

Referring back to Figure 6.19, it can be seen that the surface potential temperature at the cold-pool minima are nearly identical between simulations. The primary difference, in terms of thermodynamic properties, between the cold-pools is not the cold-pool potential temperature, but rather the environmental potential temperature. There exist several hypotheses for explaining the similar cold-pool temperatures between simulations. The first would involve the assumption that the cold-pool is produced solely because of evaporative cooling by precipitation falling into the boundary layer. It was already noted earlier that the differences in pre-storm surface temperature, and hence, potential temperature, between simulations was significantly greater than the difference in surface equivalent potential temperature due to the compensating effects of vapor vs. sensible surface heat flux. Under the preceding assumption concerning evaporative cooling, and assuming that the cold-pool is saturated, the cold-pool would reach the wet-bulb temperature. The wet-bulb temperature at a given pressure is only a function of equivalent potential temperature. Hence, the environmental temperature difference between simulations would overwhelm the cold-pool potential temperature difference between simulations in determining the theoretical density-current propagation speed. A second theory would involve the assumption that in both simulations, the cold-pool forms primarily from downdraft air that originates above the boundary layer. Air above the boundary layer is affected minimally by the soil-moisture initialization difference, and assuming nearly moist-adiabatic descent within the downdraft, the resulting cold-pool temperatures would be nearly identical between simulations. Both hypotheses rely on the cold-pool being nearly saturated and in fact the cold-pools examined in both simulations are characterized by surface relative humidity of greater than 90%. We know from the Storm II, Simulation A analysis presented above, that in fact, much of the downdraft air does originate above the boundary layer between 3 and 4-km (MSL) and that the cold-pool equivalent potential temperature is some 12K colder than the environmental boundary layer value. Therefore, the cold-pool for that storm is not produced only by evaporative cooling of boundary layer air. However, without understanding the exact source(s) of the cold-pool air in Simulation B, it is impossible to verify or reject the second hypothesis. Given the variety of mechanisms (melting precipitation, mixing from aloft, etc.) by which the surface $\theta_e$ can change, we are simply left to accept the fact that the cold-pool potential temperatures are nearly identical between simulations, and that in Simulation A, much of the cold-pool air originates above the boundary layer. At the same time, the difference in environmental low-level potential temperature, between simulations is clearly understood. It results from a greater partitioning of solar energy into sensible heat flux vs. vapor flux. We can therefore conclude that in these simulations, the increased theoretical propagation speed of the cold-pool in Simulation B is a result not due to differences in the cold-pool thermodynamic properties, but rather due to the environmental thermodynamic properties — a direct result of the soil-moisture initialization. However, the greater propagation speed and hence cold-pool spreading rate also leads to a significantly larger cold-pool in Simulation B. As indicated in a previous discussion (Section 6.3.2), the more expansive cold-pool leads to a greater frequency of cell initiation over a more expansive area.

## 6.4 0000Z-0500Z Evolution

By 0000Z the intense, flood-producing precipitation over the domain accumulated precipitation maximum, in Simulation A, is largely completed. No major changes in the behavior of Simulation B occur as the storms depicted in Figure 6.14 continue moving eastward or dissipate. The final, 0500Z accumulated precipitation distribution for both simulations is shown in Figure 6.27 below. Simulation B exhibits 8-9 cm (3.1-3.5 in) maxima along a southwest to northeast oriented band that passes between Fort Collins and Greeley. The domain maximum in Simulation B occurs along the southern boundary, approximately 43-km to the southwest of Denver and is 11-cm (4.3 in).

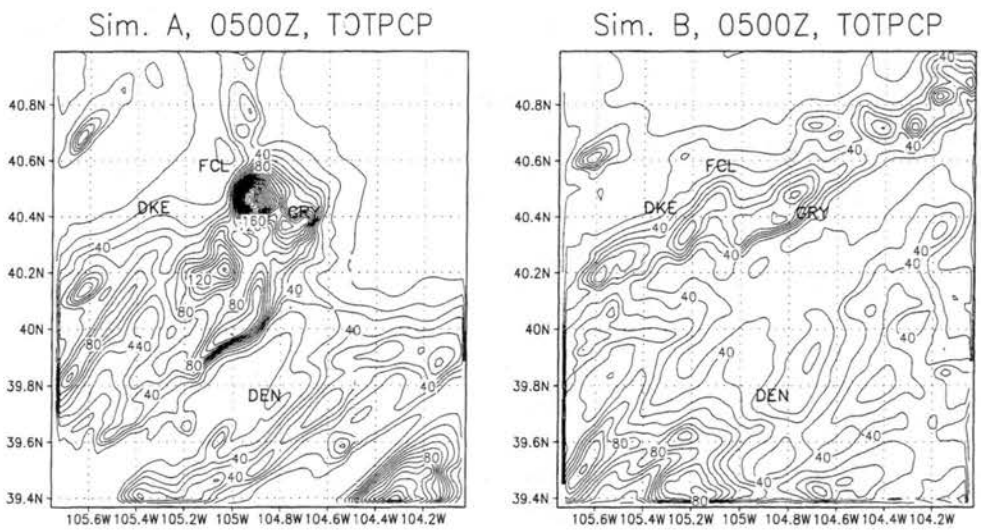


**Figure 6.27** Total accumulated precipitation for Simulations A and B at 0500Z. Accumulated precipitation contoured at 10-mm intervals. Denver, Drake, Fort Collins, and Greeley are shown for reference.

Simulation A generates a 26-cm (10.24 in.) maximum approximately 23-km to the southeast of Fort Collins. This represents a 5-cm (2.0 in.) increase above the 0000Z domain maximum value. Secondary maxima of 14 cm (5.5 in.) and 9 cm (3.5 in.) occur 42.3 km to the south-southeast of Fort Collins and 64 km to the southwest of Fort Collins, respectively. The 9-cm maximum occurs over the higher terrain where the elevation exceeds 3300-m (MSL). Recall that in the analysis of Storm II in Simulation A, that hail mixing ratios of greater than 0.5 g/kg extended down to approximately 3000-m (MSL). While hail never reached the surface in that storm, which occurred over a ~1500-m (MSL) ground surface, approximately 1.0-1.8 cm of hail does reach the ground at, and surrounding, the 9-cm maximum located over the higher terrain.

The means by which an additional 5-cm of precipitation falls over the domain maximum in Simulation A is of interest. Figure 6.28 below, shows the Grid 4 precipitation rate at 30-minute intervals for Simulation A. This figure is a time-continuation of Figure 6.12.

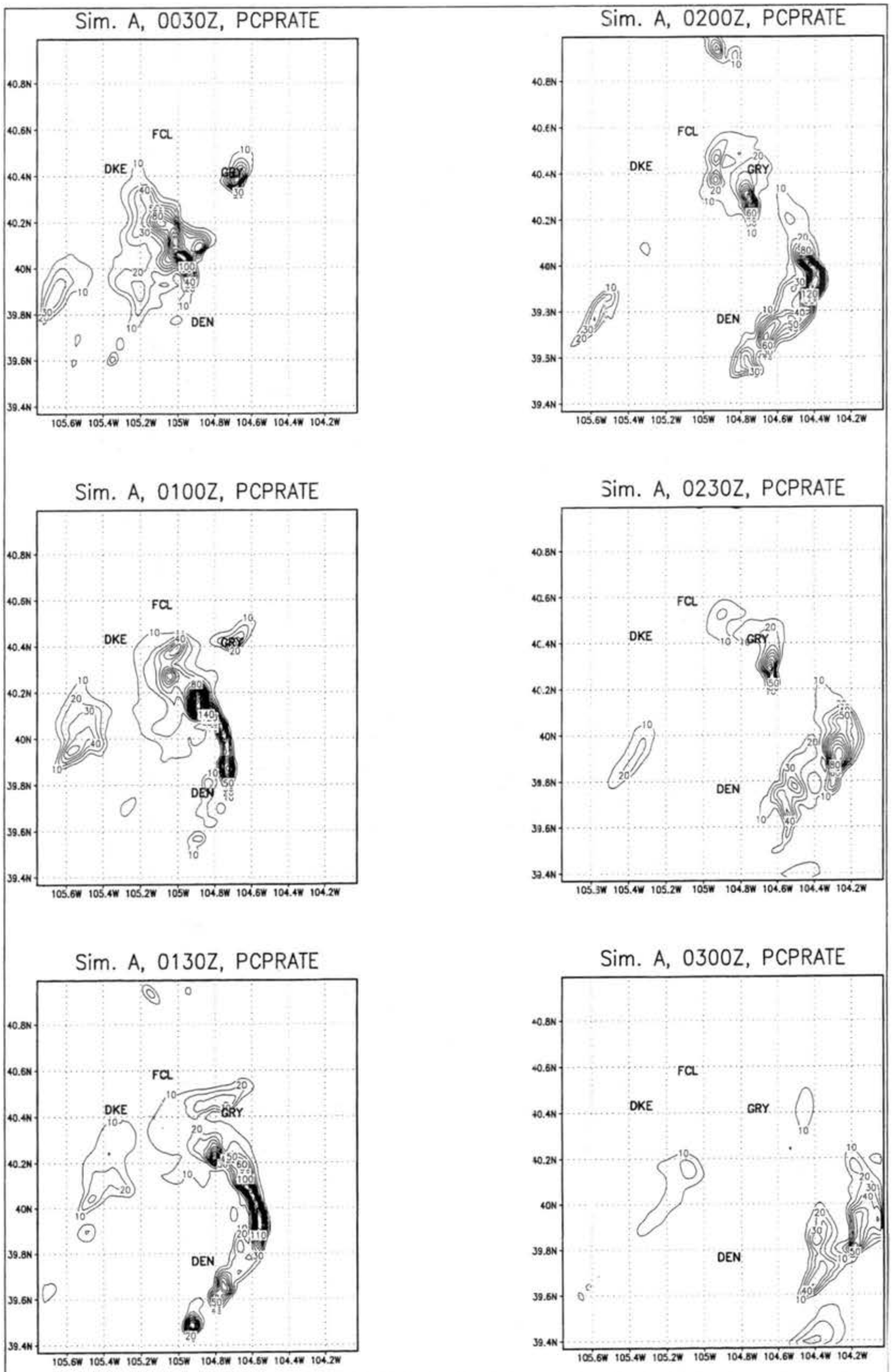


**Figure 6.28** Precipitation rate for Simulation A between 0030Z and 0500Z. Precipitation rate contoured at 10-mm/hr intervals.

The 2300Z panel in Figure 6.12 shows convection was entering the western boundary of Grid 4. This convection amplifies and organizes along the high terrain west of Denver and begins propagating eastward, off the terrain as an organized system at 0000Z. At 0100Z, this system begins to take on a distinct bow-shape as the northern tip approaches the remnants of Storm II. The eastward movement of Storm II halts and begins to propagate westward, yet again, and merges with the northern component of the system at 0200Z. It is during the 0100Z to 0230Z period that the additional 5-cm of precipitation falls over the domain maximum. The 0130Z simulated bow echo compares reasonably well with the 0200Z meso-analysis of Petersen et. al. (1999), shown in Figure 6.29.

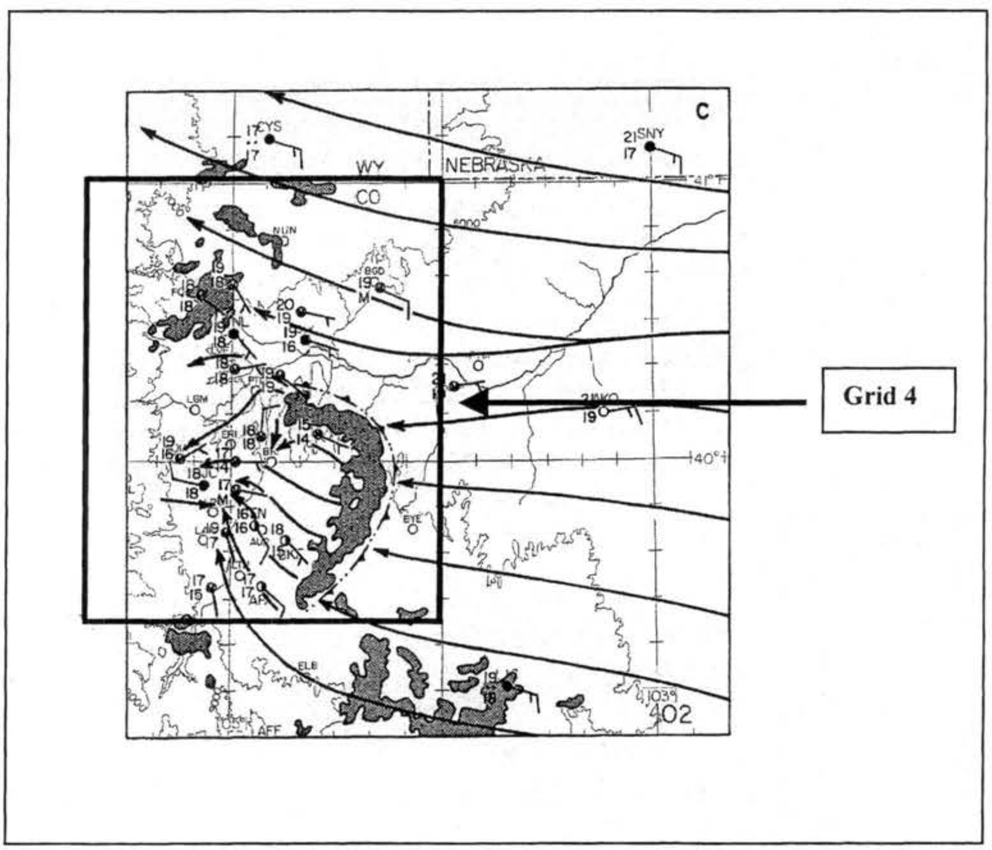


**Figure 6.29** Mesoscale analysis from Petersen et. al. (1999) at 0200Z with outline of Grid 4 superimposed. Shaded areas indicate radar reflectivity ≥ 35 dBZ. Surface streamlines shown by solid arrows. Full wind barb indicates wind-speed of ~5m/s, half barb indicates ~2.5 m/s. Outflow boundary shown by broken line.

The primary difference between the simulation and the analysis is that no convection exists over Fort Collins during the passage of the bow-echo, but is instead located between Fort Collins and Greeley. Secondly, the vast majority of flood-producing precipitation at the domain maximum has already fallen by this point in the simulation. The maximum precipitation rate within the bow echo is 21 cm/hr at 0100Z, and varies between 15 and 18 cm/hr between 0100Z and 0200Z. By 0300Z, the maximum precipitation rate in the decaying system is only 7 cm/hr. Between 0100Z and 0200Z, the bow-echo system propagates eastward at 7-8 m/s, in good agreement with the propagation speed of 8 m/s cited by Petersen et. al. (1999). Figure 6.30 shows the 0200Z 2516-m (MSL) rain-mixing ratio and wind vectors.

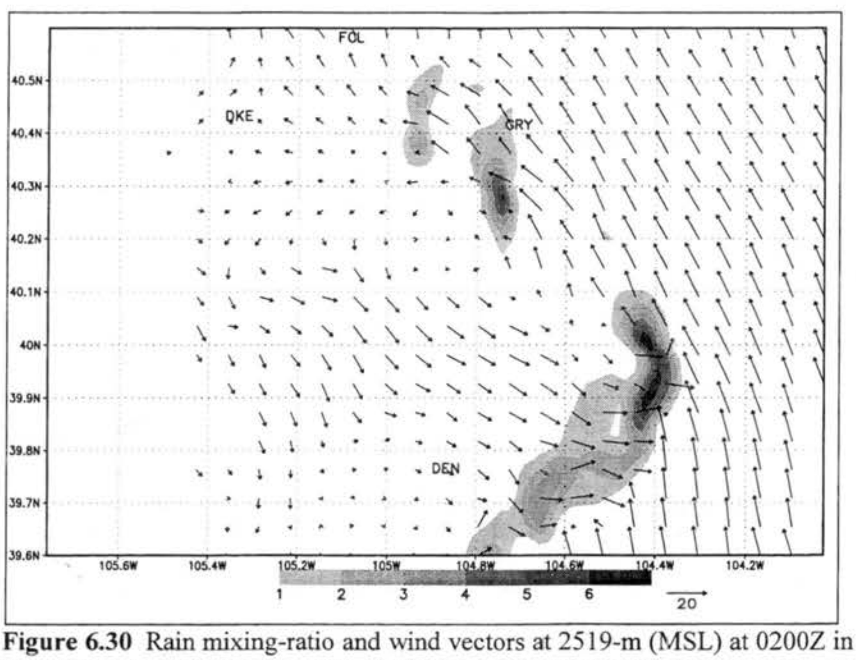


**Figure 6.30** Rain mixing-ratio and wind vectors at 2519-m (MSL) at 0200Z in Simulation A. Rain mixing ratio shaded at 1-g/kg intervals. Wind vector scale is 20 m/s.

This corresponds to approximately 1-km AGL. This figure most closely resembles the situation depicted earlier in Figure 3.7 from Petersen et. al. (1999). Both show convection situated downstream from the bow-echo to the northwest. However, in the simulation the bow-echo is only 48-km from the convection to its northwest while in Figure 3.7, the distance is ~85-km. Additionally, there is no evidence of an accelerated easterly jet as was documented in Petersen et. al. (1999). There is a modification to the environmental flow as can be seen in the westerly, or rear-inflow jet to the west of the simulated bow-echo system. Some evidence of a rear-inflow jet can also be seen in Figure 3.7 and its presence was confirmed in Petersen et. al. (1999). In short, the bow-echo in these simulations seems to play a minor role in enhancing the precipitation over the domain maximum. However, while the timing of the bow-echo seems to be in reasonable agreement with observations, the flood-producing convection occurs approximately 3-4 hours earlier than observed. Therefore it is clearly impossible to relate the bow-echo in this simulation with that which occurred in reality in terms of its effect on either the true Fort Collins storm or that in the simulation. Simulation B has not been discussed in this context because it does not produce a bow-echo.

## 6.5 Summary

In this section, we examined the pre-storm and convective evolution of both simulations. It was found that by 18Z significant differences in the low-level thermodynamic and wind fields had already developed and were consistent with those already noted on the synoptic scale in Chapter 5. The $\theta_e$ evolution difference in these simulations results in a higher surface $\theta_e$ immediately east of the Front Range foothills in Simulation A than in Simulation B after 1800Z. Higher sensible heat fluxes in Simulation B create a deeper, warmer, and dryer boundary layer than in Simulation A. A noticeable effect on the cloud-coverage was discovered with Simulation B possessing less cloud-coverage than

Simulation A. Despite the resulting higher available energy, Simulation B experiences a less-rapid $\theta_e$ increase due to boundary layer entrainment of low-$\theta_e$ air. However, the low-level dry potential temperature, and hence absolute temperature difference was significantly larger than that of the equivalent potential temperature difference between simulations.

The convective evolution of Simulation A and Simulation B were remarkably different. Simulation A exhibited explosive convective development between 2000Z and 2200Z over both the higher and lower elevations producing a quasi-stationary system at ~2200Z that released 21 cm of precipitation over approximately 2.5-3.0 hours. Simulation B, however, developed convection initially only over the higher terrain, possibly a result of the reduced CAPE and the proximity of the LCL to the downslope westerly airflow east of the mountains. The resultant outflow propagated eastward with time, initiating new cells on the windward edge of the cold-pool. No quasi-stationary systems developed in Simulation B. Precipitation rates were similar between simulations, while propagation characteristics were very different with Simulation B producing eastward and northward propagating cells on the periphery of an eastward propagating and continuously developing cold-pool.

Given the very different propagation characteristics, as well as the disparate cold-pool signatures at the surface, the cold-pool properties were examined quantitatively using a simple 2-dimensional, steady state, no-shear analytical equation for density current propagation. This revealed that Simulation B possessed a deeper cold-pool and a greater negative temperature perturbation relative to the environment at each level. However, it was found that the dominant effect on the difference in cold-pool strength (defined by the vertically integrated buoyancy) was not due to the cold-pool itself, but rather the environmental potential temperature. The pre-conditioning of the environment was well understood and followed from the partitioning of solar energy into sensible heat and vapor flux. However, the reasons for the similarity in cold-pool thermodynamic properties were not precisely identified.

Simulation A more accurately reproduces reality with more concentrated accumulated precipitation maxima, comparable to those observed, while Simulation B produces a more diffuse pattern — a result of the increased propagation speeds of the simulated storms in the latter simulation. Simulation A produces 26 cm (10.2 in.) approximately 22-km to the southeast of Fort Collins by 0500Z, which is within one inch of the observed Fort Collins storm total. Simulation A also reproduces, in reasonable accordance with observations, a bow-echo that was observed to form around 0000Z and propagated onto the plains between 0000Z and 0300Z. However, the timing of the primary, flood-producing storm is roughly 4 hours early. The reason for this timing discrepancy is not understood but is likely related to the rapid growth of CAPE and vanishing CIN east of the foothills around 2000Z with a relatively high soil-moisture condition. This may, in fact, be a result of initializing these simulations without cloud-cover, cloud-cover which *was* present, as confirmed by satellite imagery and common knowledge, during the early- and late-morning hours of July 28.

# 7

# Summary and Conclusions

## 7.1 Summary of Experiment

In this thesis, two simulations were performed with RAMS 3b corresponding to the period of the July 28, 1997 Fort Collins flash flood. The two simulations performed differed only in initial soil moisture content. Simulation A utilized the 12Z July 28 soil moisture analysis from the operational ETA model while Simulation B used the API method for estimating antecedent soil moisture. The motive for performing these simulations was to assess to what extent the model evolution differed between simulations, especially with regard to the magnitude, location, timing, and even existence of extreme precipitation accumulation. Such sensitivity, if identified, provides useful information not only for model development and initialization evaluation, but also for future and current studies whose aim is to provide extreme precipitation estimates using a numerical model.

## 7.2 Conclusions

Examination of the model evolution showed that Simulations A and B differed significantly in their evolution. The differences between simulations were found to be significant not only on the convective scale, but on the synoptic scale as well. The simulated 1800Z-0500Z synoptic-scale, accumulated precipitation maximum in Simulation B was located east of the Continental Divide, while in Simulation A, the large-scale accumulated precipitation maximum was produced west of the Continental Divide. This resulted from an enhanced upslope flow in Simulation B, especially east of the Continental Divide, which, in turn, was due to a higher low-level temperature field in that simulation.

Simulation B produced Grid 4 precipitation maxima that were less than half of the maximum in Simulation A. One of the most significant results in these simulations is that the primary factor governing the accumulated precipitation difference is storm movement as opposed to storm intensity. The lack of quasi-stationary storms in Simulation B was attributed to the more vigorous cold-pools in that simulation.

The relationship between cold-pool strength and soil moisture initialization was partially identified. The primary influence on the differing cold-pool strength was found to be due to the environmental potential temperature difference between simulations, rather than the cold-pool potential temperature difference between simulations. The increased cold-pool depth and perturbation temperature in Simulation B was primarily due to the increased temperature and depth of the environmental boundary layer in Simulation B. The environmental boundary layer evolution was examined in both simulations and the differences were directly associated with the differential partitioning of available energy into sensible and latent heat fluxes due to the soil moisture initialization. Hence, the soil-moisture initialization affects the simulated cold-pool propagation speed, not by directly altering the cold-pool itself, but rather by modifying the environment into which it propagates. However, it was also noted that the location of the LCL and LFC near and within, respectively, the westerly mid-level flow may have also contributed to the increased tendency for westward propagation in Simulation B.

The existence of extreme precipitation accumulation in Simulation A, which is within an inch of the observed accumulated precipitation for the 1200Z-0500Z period, makes Simulation A more plausible on the basis of precipitation alone. Secondly, the extreme precipitation event simulated occurs within 23 km spatially, 4-5 hours temporally, and within 1 inch of the precipitation total observed. Thirdly, the production of a quasi-stationary storm system in Simulation A, a characteristic of the Fort Collins storm during its most intense phase, gives more credence to the results of Simulation A. Additionally, the relationship identified in this thesis, between the low-level thermodynamic environment, cold-pool motion, and simulated storm motion, logically connects the errors in low-level thermodynamic prediction and accumulated precipitation in Simulation B. Finally, the remarkable correspondence between the bow-echo in Simulation A and that observed and noted in Petersen et. al. (1999), and the lack of said feature in Simulation B also establishes Simulation A as the more realistic simulation of the two.

## 7.3 Suggestions for Future Research

A reading of this thesis shows quite clearly that there remains a considerable amount of uncertainty in the numerical modeling and forecasting of localized convective storms. Hence, many of the suggestions for future research are based on some of the fundamental problems encountered with these simulations. As noted in Chapter 5, serious errors in the low-level thermodynamic fields occur over rather large areas in Simulation A due to an excessive evaporation fraction. For an operational version of this model, the forecast error would essentially necessitate the avoidance of initializing the model with soil moisture content greater than ~50% saturation, despite the fact that such values and larger are observed. In this situation, it is clear that the desired forecast is determining the initial soil moisture content more so than the other way around, which severely limits the potential utility of the soil model. Secondly, it has been well established in this thesis as well as in cited research, that the primary effect of soil moisture and its spatial variability on the overlying atmosphere occurs through the control on the partitioning of available energy into latent and sensible heat flux at the lower boundary. It seems quite futile to investigate this in detail without also examining the controls on available energy itself, such as cloud cover. As noted previously, these simulations, like most performed with this model, are initialized without condensate. Even with a perfect or true soil moisture field and a perfect soil and vegetation model, the error resulting from erroneous available energy fluxes makes the partitioning of such, moot. Hence, it would seem that research with the goal of improving the behavior and accuracy of simulated surface energy fluxes, needs to consider cloud and soil moisture initialization as a single problem, and/or surface parameterizations need to be tested offline with imposed observational data.

A second problem encountered with the simulations in this thesis concerns the timing of precipitation. The timing of the flood producing precipitation in Simulation A is 3-4 hours earlier than observed. This is significant because in addition to the Fort Collins flood, two other major Type I flood events have occurred east of the Continental Divide: The Big Thompson flood of 1976 and the Rapid City flood of 1972. Both of these floods occurred at or after nightfall. While no reason for this pattern has been identified in the literature, its existence may signify an, as of yet, unidentified influence on extreme precipitation near complex terrain, such as the timing and spatial-scales of thermally induced slope-flows. Secondly, radar imagery from the Fort Collins event such as that shown in Figure 7.1 shows a clear indication of orographic anchoring of storms along the Front Range between 2100Z and 0200Z.

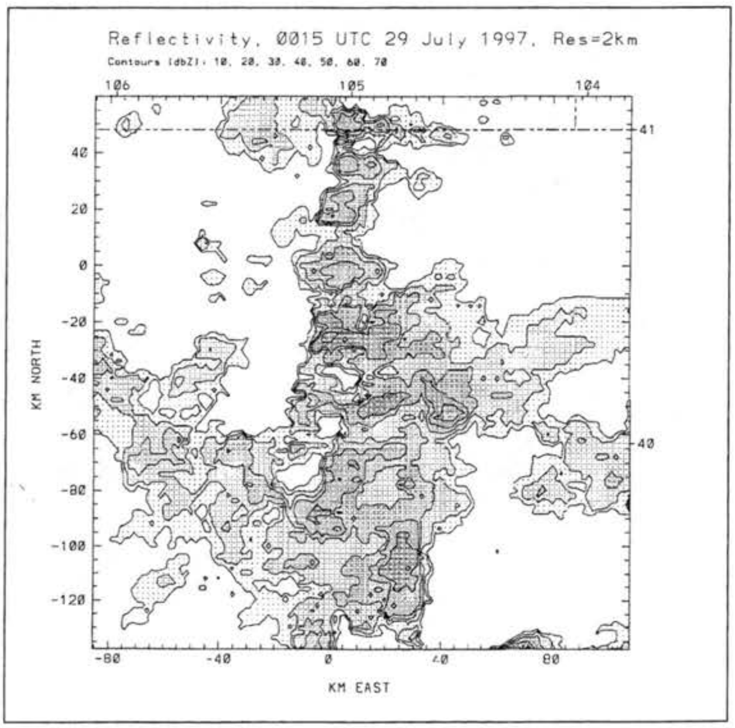


**Figure 7.1** Radar reflectivity at 0015Z showing orographic anchoring of storms along Front Range foothills. Axis values denote distance north and south of CSU campus observation station.

No pattern suggestive of orographic anchoring can be identified in the precipitation rate plots of Chapter 6. This is, again, troubling since both the Rapid City and Big Thompson events, which were meteorologically similar to the Fort Collins event, also demonstrated storm fixation by topography. Without proper timing or orographic anchoring, it is nearly impossible to use these simulations to determine the role topography plays in reality. The question of what would be required to obtain orographically anchored storms under meteorologically similar conditions, as has been consistently observed, has not been answered by this thesis. Research of this question would likely need to start as an idealized experiment with two components — initiation and maintenance. One of the problems with the simulations in this thesis is that there is no storm initiation at the base of the foothills. Hence, the problem in these simulations may be an initiation problem as opposed to maintenance. This would certainly be an excellent topic to pursue, as an understanding of this problem would have a wide range of applicability to operational forecasting and research investigating the dependence of extreme precipitation on elevation.

It was shown that the cold-pool propagation speeds in the performed simulations were linked to both the storm motion and the environmental thermodynamic conditions. For a thunderstorm whose downdraft air originates below the middle-troposphere and above the boundary layer, as in Simulation A, the combination of a nearly moist-adiabatic lapse rate with nearly saturated conditions up to at least the mid-troposphere would be optimal. This is because air parcels entering the downdraft will descend the moist adiabat that closely matches the environmental profile, thereby bounding the temperature perturbation of the cold-pool and weakening the tendency of the storm to propagate away from the topography. This is much like the claim made by Maddox et. al. (1977) in which high moisture content throughout the depth of the troposphere aids in minimizing cold-pool strength. However, the current claim being made here is that, in addition to saturation, a nearly moist-adiabatic temperature lapse rate is also helpful to reduce the temperature perturbation of the cold-pool. At the same time, we also know that a perfectly moist adiabatic lapse rate throughout the troposphere produces little or no CAPE. Since precipitation accumulation depends on both precipitation intensity and storm movement, a particular balance between CAPE and the environmental temperature profile may be necessary to obtain both intense precipitation and nearly stationary movement. For a given shear profile, 3-dimensional, horizontally homogenous simulations without topography, along with a series of differing thermodynamic profiles, would serve as an excellent starting-point to investigate this question. The role of topography wouldn't be well understood without first investigating this question anyhow. This would also be a good set of experiments to augment with sensitivity simulations in which microphysical parameters, such as hydrometeor size or concentration, are varied.

In conclusion, it is apparent that, as a scientific community, we have a considerable amount of progress to make before we can reliably use numerical models to forecast local convective events without requiring constant attention and ad-hoc modifications to the initialization procedure. For this reason, much of the attention in future work must focus on exactly this — the initialization procedure. Soil moisture continues to be an especially problematic field due to the lack of observations, and the wide range of surface parameterization behavior across models. Given the wide range of behaviors among surface models, it seems that the primary benefit to obtaining soil-moisture measurements would need to be realized in the improvement of surface modeling. In the mean time, much progress can be made by considering equally complex problems such as orographic anchoring and storm movement vs. precipitation intensity as a function of microphysical specifications and temperature and moisture profiles. These problems, though complex in nature, will only be understood through intelligent and simple experiment design. The resulting experiments should provide a framework for interpreting more complex experiments, such as those performed in this thesis. With a disciplined approach, we should have both the computational and intellectual tools necessary to provide useful results for both operational and research applications in the field of extreme precipitation.

# References


Abbs D. J., and B. F. Ryan, 1997: Numerical modelling of extreme precipitation events., UWRAA Res. Rep. No. 131, 76 pp.

Avissar, R., and Y. Mahrer, 1988: Mapping frost-sensitive areas with a three-dimensional local-scale numerical model. Part I: Physical and numerical aspects., *J. Appl. Meteor.*, **27**, 400-413.

Barnes, S. L., 1973: Mesoscale objective map analysis using weighted time series observations. NOAA Tech. Memo. ERL NSSL-62, 60 pp. [NTIS COM-73-10781].

Bernardet, L. R., L. D. Grasso, J. E. Nachamkin, C. A. Finley, and W. R. Cotton, 2000: Simulating convective events using a high-resolution mesoscale model., *J. Geophys. Res.*, **105**(D11), 14963-14982.

Betts, A. K., and J. H. Ball, 1995: The FIFE diurnal cycle climate., *J. Geophys. Res.*, **100**(D12), 25679-25693.

Betts, A. K., J. H. Ball, A. C. M. Beljaars, M. J. Miller, and P. Viterbo, 1996: The land surface-atmosphere interaction: A review based on observational and global modeling perspectives., *J. Geophys. Res.*, **101**, 7209-7225.

Betts, A. K., Fei Chen, Kenneth E. Mitchell, and Zavisa J. Janjic, 1997: Assessment of the land surface and boundary layer models in two operational versions of the NCEP ETA model using FIFE data., *Mon. Wea. Rev.*, **125**, 2896-2916.

Black, Thomas, and Coauthors, 1997: Changes to the ETA forecast systems. Tech. Proc. Bull. No. 441, National Weather Service, Office of Meteorology, Science Division, Silver Spring, Maryland, 20910.

Bosilovich, Michael G., and Wen-Yih Sun, 1999: Numerical simulation of the 1993 Midwestern flood: Land-atmosphere interactions., *J. Climate*, **12**, 1490-1505.

Brown, Michael E., and David L. Arnold, 1998: Land-surface-atmosphere interactions associated with deep convection in Illinois., *Int. J. Climatol.*, **18**, 1637-1653.

Caracena, Fernando, R. A. Maddox, L. R. Hoxit, and C. F. Chappell, 1979: Mesoanalysis of the Big Thompson storm., *Mon. Wea. Rev.*, **107**(1), 1-17.

Chang, C. B., and D. J. Perkey, 1995: Numerical simulations of mesoscale flood environment., *Meteorol. Atmos. Phys.*, **55**, 17-32.

Chang, Jy-Tai, and Peter J. Wetzel, 1991: Effects of spatial variations of soil moisture and vegetation on the evolution of a prestorm environment: A numerical case study., *Mon. Wea. Rev.*, **119**, 1368-1390.

Chen, C., and W. R. Cotton, 1983: A one-dimensional simulation of the stratocumulus-capped mixed layer., *Bound.-Layer Meteor.*, **25**, 289-321.

Chen, F., K. Mitchell,, J. Schaake, Y. Xue, H.-L Pan, V. Koren, Q. Duan, and A. Betts, 1996: Modeling of land-surface evaporation by four schemes and comparison with FIFE observations., *J. Geophys. Res.*, **101**, 7251-7268.

Choudhury, B. J., and Bruce J. Blanchard, 1983: Simulating soil water recession coefficients for agricultural watersheds., *Water Resources Bull.*, **19**(2), 241-247.

Clark, Craig A., and Raymond W. Arritt, 1995: Numerical simulations of the effect of soil moisture and vegetation cover on the development of deep convection., *J. Appl. Meteor.*, **34**, 2029-2045.

Clark, T. L., and R. D. Farley, 1984: Sever downslope windstorm calculations in two and three spatial dimensions using anelastic interactive grid nesting: A possible mechanism for gustiness., *J. Atmos. Sci.*, **41**, 329-350.

Clark, T. L., and W. D. Hall, 1991: Multi-domain simulations of the time dependent Navier-Stokes equations: Benchmark error analysis of some nesting procedures., *J. Comput. Phys.*, **92**, 456-481.

Cotton, W. R., R. L. McAnelly, and C. T. Ashby, 2001: Estimating extreme precipitation at high elevations in Colorado through mesoscale ensemble modeling., *Preprints Proc. 15th Conf. on Precipitation Extremes: Predictions, Impacts, and Responses*, 14-18 Jan. 2001, Albuquerque, New Mexico, AMS, pp. 248-251.

Davies, H. C., 1983: Limitations of some common lateral boundary schemes used in regional NWP models., *Mon. Wea. Rev.*, **111**, 1002-1012.

Dennis, A. S., R. A. Schleusener, J. H. Hirsch, and A. Koscielski, 1973: Meteorology of the Black Hills flood of 1972., Rep. 73-4, Institute of Atmospheric Sciences, South Dakota School of Mines and Technology, Rapid City, South Dakota, 57701.

Dickinson, R. E., A. Henderson-Sellers, P. J. Kennedy, and M. F. Wilson, 1986: *Biosphere-Atmosphere Transfer Scheme (BATS) for the NCAR Community Climate Model*, National Center for Atmospheric Research, Boulder, Colorado, Tech. Note TN-275+STR.

Doesken, N. J., and T. B. McKee, 1998: An analysis of rainfall for the July 28, 1997 flood in FCL, Colorado. Climatology Rep. 98-1, Department of Atmospheric Science, Colorado State University, 55 pp.

Douglas, Michael W., R. A. Maddox, Kenneth Howard, and Sergio Reyes, 1993: The Mexican Monsoon., *J. Climate*, **6**(8), 1665-1677.

Gal-Chen, T., and R. C. J. Somerville, 1975: On the use of a coordinate transformation for the solution of the Navier-Stokes equations., *J. Comput. Phys.*, **17**, 209-228.

Gallus, William A. Jr., and Moti Segal, 2000: Sensitivity of forecast rainfall in a Texas convective system to soil moisture and convective parameterization., *Wea. Forecasting.*, **15**, 509-525.

Grasso, Lewis D., and W. R. Cotton, 1995: Numerical simulation of a tornado vortex., *J. Atmos. Sci.*, **52**(8), 1192-1203.

Grossi, P., G. Graziani, and C. Cerutti, 1998: Mesoscale flow and pollutants transport modelling in north-east Sicily., *Air Pollution Modelling and its Applications XII*, Plenum Press, p. 43-51.

Grossman, Robert L., and Dale R. Durran, 1984: Interaction of low-level flow with the western Ghat Mountains and offshore convection in the summer monsoon., *Mon. Wea. Rev.*, **112**, 652-672.

Hill, G. E., 1974: Factors controlling the size and spacing of cumulus clouds as revealed by numerical experiments., *J. Atmos. Sci.*, **31**, 646-673.

Hong, Song-You, and Hua-Lu Pan, 1996: Non-local boundary layer vertical diffusion in a medium-range forecast model., *Mon. Wea. Rev.*, **124**(10), 2322-2339.

Janjic, Z. I., 1996: The surface layer parameterization in the NCEP ETA model. Research Activities in Atmospheric and Oceanic Modeling, WMO, Genve, CAS/JSC WGNE, 4.16-4.17. [Available from World Meteorological Organization, Case Postale 2300, CH-1211 Geneva, Switzerland.]

Kanamitsu, Masao, 1989: Description of the NMC global data assimilation and forecast system., *Wea. Forecast.*, **4**, 335-342.

Klemp, J. B., and R. B. Wilhelmson, 1978: The simulation of three-dimensional convective storm dynamics., *J. Atmos. Sci.*, **35**, 1070-1096.

Kopp, Fred J., and Harold D. Orville, 1973: Numerical simulation of the June 9, 1972 storm in the Black Hills. *Preprints, 8th Conf. on Severe Local Storms,* Denver, Colorado, Oct. 15-17, 1973, 287-292.

Knupp, Kevin R., 1987: Downdrafts within High Plains cumulonimbi. Part I: General kinematic structure., *J. Atmos. Sci.*, **44**, 987-1008.

Kuo, H. L, 1974: Further studies of the parameterization of the influence of cumulus convection on large-scale flow., *J. Atmos. Sci.*, **31**(5), 1232-1240.

Lilly, D. K., 1962: On the numerical simulation of buoyant convection., *Tellus, XIV*, **2**, 148-172.

Liu, Changhai, and Mitchell W. Moncrieff, 1996: An analytical study of density currents in sheared, stratified fluids including the effects of latent heating., *J. Atmos. Sci.*, **53**(22), 3303-3312.

Louis, J. F., 1979: Parametric model of vertical eddy fluxes in the atmosphere., *Boundary-Layer Meteor.*, **17**, 187-202

Maddox, R.A., Fernando Caracena, Lee R. Hoxit, and Charles F. Chappell, 1977: Meteorological aspects of the Big Thompson flash flood of 31 July 1976., NOAA Tech. Rep. ERL 388-APCL 41, 84 pp.

Maddox, R.A., Lee R. Hoxit, Charles F. Chappell, and Fernando Caracena, 1978: Comparison of meteorological aspects of the Big Thompson and Rapid City flash floods., *Mon. Wea. Rev.*, **106**, 375-389.

Maddox, R. A., C. F. Chappell, and L. R. Hoxit, 1979: Synoptic and meso-$\alpha$ scale aspects of flash flood events., *Bull. Amer. Meteor. Soc.*, **60**(2), 115-123.

Maddox, R.A., Lee R. Hoxit, and Faye Canova, 1980: Meteorological characteristics of heavy precipitation and flash flood events over the western United States., NOAA Tech. Memo. ERL APCL-23, 87 pp.

Mahrer, Ytzhaq, and Roger A. Pielke, 1977: A numerical study of the airflow over irregular terrain., *Beitrage zur Physik der Atmosphäre*, **50**, 98-113.

Maidment, David R. (ed.), 1993: Handbook of hydrology., McGraw-Hill., (various pagings).

Marwitz, John D., 1972: Precipitation efficiency of thunderstorms on the high plains., *J. de Rech. Atmos.*, **6**, 367-370.

McAnelly, Ray L., Jason E. Nachamkin, William R. Cotton, and Melville E. Nicholls, 1997: Upscale evolution of MCS's: Doppler radar analysis and analytical investigation., *Mon. Wea. Rev.*, **125**(6), 1083-1110.

McCumber, Michael C., and Roger A. Pielke, 1981: Simulation of the effects of surface fluxes of heat moisture in a mesoscale numerical model. 1. Soil layer., *J. Geophys. Res.*, **86**, 9929-9938.

McKee, T. B., and N. J. Doesken, 1997: Final report: Colorado extreme precipitation data study. Climatology Rep. 97-1, Department of Atmospheric Science, Colorado State University, 107 pp.

Mesinger, F., and A. Arakawa, 1976: Numerical methods used in atmospheric models. GARP Publication Series, No. 14, WMO/ICSU Joint Organizing Committee, 64 pp.

Miller, M. J., 1978: The Hampstead storm: A numerical simulation of a quasi-stationary cumulonimbus system., *Quart. J. R. Met. Soc.*, **104**, 413-427.

Moncrieff, M. W., and J. S. A. Green, 1972: The propagation and transfer properties of steady convective overturning in shear., *Quart. J. R. Met. Soc.*, **98**, 336-352.

Nair, U.S., Mark R. Hjelmfelt, and Roger A. Pielke Sr., 1997: Numerical simulation of the 9-10 June 1972 Black Hills storm using CSU-RAMS., *Mon. Wea. Rev.*, **125**, 1753-1766.

National Research Council, 1994: *Estimating bounds on extreme precipitation events: A brief assessment.*, National Academy Press, 29 pp.

Ogura, Yoshi, and Masanori Yoshizaki, 1988: Numerical study of orographic-convective precipitation over the Eastern Arabian Sea and the Ghat Mountains during the summer monsoon., *J. Atmos. Sci.*, **45**(15), 2097-2181.

Ookuchi, Y., M. Segal, R. C. Kessler, and R.A. Pielke, 1984: Evaluation of soil moisture effects on the generation and modification of mesoscale circulations., *Mon. Wea. Rev.*, **112**, 2281-2292.

Pan, H. L., and L. Mahrt, 1987: Interaction between soil hydrology and boundary-layer development., *Bound.-Layer Meteor.*, **38**, 185-202.

Petersen, Walter A., and Coauthors, 1999: Mesoscale and radar observations of the Fort Collins flash flood of 28 July 1997., *Bull. Amer. Meteor. Soc.*, **80**(2), 191-216.

Pielke R.A., and Coauthors, 1992: A comprehensive meteorological modeling system — RAMS., *Meteorol. Atmos. Phys.*, **49**, 69-91.

Rogash, Joseph A., 1988: The synoptic and meso-α scale meteorology of Wyoming flash floods., NOAA Tech. Memo. NWS CR-93., 22 pp.

Rogers, Eric, Thomas L. Black, Dennis G. Deaven, and Geoffrey J. DiMeggo, 1996: Changes to the operational "Early" ETA analysis/forecast system at the National Centers for Environmental Prediction., *Wea. Forecast.*, **11**, 391-413.

Rotunno, Richard, Joseph B. Klemp, and Morris L. Weisman, 1988: A theory for strong, long-lived squall lines., *J. Atmos. Sci.*, **45**(3), 463-485.

Saxton, Keith E., and Arno T. Lenz, 1967: Antecedent retention indexes predict soil moisture., *J. Hydraulics Div. Proc. Am. Soc. Civ. Eng.*, **HY4**, 223-241.

Segal, M., and R. W. Arritt, 1992: Nonclassical mesoscale circulations caused by surface sensible heat-flux gradients., *Bull. Amer. Meteor. Soc.*, **73**(10), 1593-1604.

Smagorinsky, J., 1963: General circulation experiments with the primitive equations. Part I: The basic experiment., *Mon. Wea. Rev.*, **91**, 99-164.

Smith, R. B., 1985: Comment on "Interaction of low-level flow with the Western Ghat Mountains and offshore convection in the summer monsoon"., *Mon. Wea. Rev.*, **113**, 2176-2177.

Snook, John S., Jennifer M. Cram, and Jermome M. Schmidt, 1995: LAPS/RAMS: A nonhydrostatic mesoscale numerical modeling system configured for operational use., *Tellus Ser. A*, **47A**(5), 864-875.

St. Amand, Pierre, R. J. Davis, and R. D. Elliott, 1972: Report on Rapid City flood of 9 June 1972. to South Dakota Weather Control Commission, South Dakota Weather Control Commission, Pierre, South Dakota, 37 pp.

State of Colorado and Federal Emergency Management Agency (FEMA), 1997: Flood of 97: Hazard mitigation team report in response to DR-1186-CO flood disaster in Colorado declared August 1, 1997., 48 pp.

Stull, Roland B., 1988: An introduction to boundary layer meteorology., Kluwer Academic Publishers, 670 pp.

Tremback, C. J., and R. Kessler, 1985: A surface temperature and moisture parameterization for use in mesoscale numerical models., *Preprints, 7th AMS Conference on Numerical Weather Prediction,* Montreal, Quebec, Canada, Amer. Meteor. Soc., Boston, 355-358.

Tremback, C. J., 1990: Numerical simulation of a mesoscale convective complex: model development and numerical results. Ph.D. dissertation, Atmos. Sci. Paper No. 465., Colorado State University, Dept. of Atmospheric Science, Fort Collins, Colorado, 80523.

Tripoli, G., and W. R. Cotton, 1982: The Colorado State University three-dimensional cloud/mesoscale model — 1982. Part I: General theoretical framework and sensitivity experiments., *J. de Rech. Atmos.*, **16**, 185-220.

Tripoli, G. and W. R. Cotton, 1989: A numerical study of an observed orogenic mesoscale convective system. Part 1. Simulated genesis and comparison with observations., *Mon. Wea. Rev.*, **117**, 273-304.

United States Department of Agriculture (USDA), 1951: Soil survey manual., *U.S. Dep. of Agric. Handbook*, No. 18, 1-503.

United States Naval Observatory (USNO): Table of sunrise/set, moonrise/set, and twilight times., http://aa.usno.navy.mil/AA/.

Vidale, Piere Luigi, Roger A. Pielke Sr., Louis T. Stayaert, and Alan Barr, 1997: Case study modeling of turbulent and mesoscale fluxes over the BOREAS region., *J. Geophys. Res.*, **102**(D4), 29167-29188.

Walko, R. L., W. R. Cotton, M. P. Meyers, and J. Y. Harrington, 1995: New RAMS cloud microphysics parameterization. Part I: the single-moment scheme., *Atmos. Res.*, **38**, 29-62.

Weisman, M. L., and J. B. Klemp, 1982: The dependence of numerically simulated convective storms on vertical wind shear and buoyancy., *Mon. Wea. Rev.*, **110**, 504-520.

Wood, Richard A. (ed.), 1999: *The Weather Almanac: A Reference Guide to Weather, Climate and Related Issues in the United States and its Key Cities*. 9th edition. Gale Group. 738 pp.

Yan, Hong, and Richard A. Anthes, 1988: Effects of variations in surface moisture on mesoscale circulation., *Mon. Wea. Rev.*, **116**(1), 192-208.

Yoshizaki, Masanori, and Yoshi Ogura, 1988: Two- and three-dimensional modeling studies of the Big Thompson storm., *J. Atmos. Sci.*, **45**(23), 3700-3722.